PET BLOCK DETECTOR DESIGN FOR SIMULTANEOUS PET/MR IMAGING

NOVEL PET BLOCK DETECTOR DESIGN FOR SIMULTANEOUS PET/MR IMAGING

By

EVAN DOWNIE, B. Eng.

A Thesis Submitted to the School of Graduate Studies in Partial Fulfillment of the Requirements for the Degree Master of Applied Science

MASTER OF APPLIED SCIENCE (2013) McMaster University
(School of Biomedical Engineering) Hamilton, Ontario

TITLE:	Novel PET Block Detector Design for Simultaneous PET/MR Imaging
AUTHOR:	Evan Downie
SUPERVISOR:	Professor Hao Peng
NUMBER OF PAGES:	x, 123

Abstract

We investigated the use of multiplexing and an electro-optical coupling system in the design of magnetic resonance compatible positron emission tomography (PET) detectors. Reducing the number of output channels is an effective way to minimize cost and complexity and complements the substitution of coaxial cables for fiber optics. In this work, we first compared the system performance of two multiplexing schemes using both simulation and experimental studies. Simulations were performed using the LTSPICE environment to investigate differences in resulting flood histograms and rising edge slopes. Experiments were performed using Lutetium-Yttrium Oxyorthosilicate (LYSO) crystals of coupled to a SensL ArraySL-4 silicon photomultiplier (SiPM) connected to interchangeable circuit boards containing the two multiplexing schemes of interest. Three crystal configurations were tested: single crystal element (3x3x20 mm^3), 2x2 array (crystal pitch: 3x3x20 mm^3) and 6x6 array (crystal pitch: 2.1x2.1x20 mm^3). Good agreement was found between the simulations and experiment results. The capacitive multiplexer is able to achieve improved time resolution of good uniformity (average of 1.11±0.01ns and 1.90±0.03ns for the arrays, respectively) and crystal separation, compared to the resistive multiplexing (average of 1.95±0.03ns and 3.33±0.10ns). The resistive multiplexing demonstrates slightly improved energy resolution (11±0.1% and 22±0.6%, compared to 12±0.1% and 24±0.4% for the capacitive array). The relevancy of this work to the PET block detector design using SiPM arrays is also discussed, including light sharing, edge compression and gain variation among SiPM pixels. This work also examines the effect of the electro-optical coupling system by comparing the system performance between cases with and without it. The coupling system is found to adversely affect performance, increasing global energy resolution by ~6%, average timing resolution by ~120% and distorting the flood histogram. Reasons for the discrepancy and potential solutions are provided.

Acknowledgements

First and foremost I would like to thank my supervisor, Dr. Hao Peng, for granting me this opportunity and providing his support, being patient through my development as a graduate student and researcher, and being a great friend and mentor. I'd also like to thank Dr. Mike Noseworthy, for without his recommendations I may not have received the opportunities and support that were given to me. He was the one to first spark my interest in the field of medical imaging, and in combination with Dr. Brash of the School of Biomedical Engineering, my interest in graduate studies. Without the help of Dr. Troy Farncombe for his assistance in (and sharing of) the lab, Dr. Xun Li for his help in the design of the laser packaging, and Dr. Jamal Deen for offering his dark room for experiments and being part of my defense committee, this would have been a much more difficult journey, and I thank them for that.

The support staff at McMaster University have been a great source of help and support through these years as well. I must thank Kenrick Chin for his wisdom in printed circuit board design, Tyler Ackland for his help and for providing the odd potentiometer or capacitor, Clealand Berwick and the engineering machine shop for their help with designing our own light tight box, and Natalie Illingworth for taking time from her busy schedule of organising Mike to answer the plethora of questions I had.

I'd like to acknowledge CXFiber and the staff that were patient and understanding during our design process and for their great work on the finished product.

I'm grateful to have worked with everyone from our lab, Alireza, Xin, Yicheng, Ruibin, Fumin, Jenna, David, Dost, Ashley Mohammed and Nasit; thanks for your friendship, support, distractions and all of the fun we had, I wish you all the best and to see you again soon. Thanks to Darek Palubiak for helping with the laser, Tim Munsie for cutting crystals and glass for our lab, and to everyone from Mike's lab for contributing to the great environment at McMaster. Special thanks to Basilique for providing me with food to keep me sated.

Finally, thanks to my parents, Tim and Michele, brothers, Brian and Shane, and my girlfriend, Dana, for your unwavering love and support over these exciting, exhausting, and sometimes excruciating years of post secondary education. Without it, I would surely have been lost.

Table of Contents

List of Abbreviations

ADC	Analog-to-Digital Converter
APD	Avalanche Photodiode
CFD	Constant Fraction Discriminator
cps	Counts per second
CT	Computed Tomography (X-Ray)
DOI	Depth of Interaction
EC	Electron Capture
ESR	Enhanced Specular Reflector
FDG	Fluorodeoxyglucose
FPGA	Field Programmable Gate Array
FOV	Field of View
FWHM	Full Width at Half Maximum
LOR	Line of Response
LSO	Lutetium Orthosilicate
LYSO	Lutetium-Yttrium Orthosilicate
NECR	Noise Equivalent Count Rate
NIM	Nuclear Instrumentation Module
MC	Monte Carlo
MMF	Multi-Mode Fiber
MRI	Magnetic Resonance Imaging
MR-AC	Magnetic Resonance Attenuation Correction
PDE	Photon Detection Efficiency
PET	Positron Emission Tomography
PMT	Photomultiplier Tube
PSF	Point Spread Function
RF	Radiofrequency
rms	Root-mean-square
SiPM	Silicon Photomultiplier
SNR	Signal-to-Noise Ratio
SSPM	Solid State Photomultiplier
SPECT	Single Photon Emission Computed Tomography
TOF	Time of Flight
VCSEL	Vertical-Cavity Surface-Emitting Laser

List of Figures

List of Tables

Chapter 1

Introduction

1.1 Positron Emission Tomography

Positron emission tomography (PET) is one of the two main imaging modalities in nuclear medicine. PET and single-photon emission computed tomography (SPECT) are non-invasive techniques which utilize radioactive tracers to generate images representing the bodies' physiology. These techniques are categorized as functional imaging and differentiate from methods that principally generate images of anatomical structures, such as x-ray computed tomography (CT), by detecting gamma-ray emission from radiopharmaceuticals within the patient to acquire physiological information which is represented in volumetric images (Wernick & Aarsvold, 2004).

PET and SPECT differ mostly by the types of radioactive particles included in the radiopharmaceutical. As the names suggest, SPECT detects single-photon emissions from particles such as technetium-99m (^{99m}Tc), iodine-123 (^{123}I), and indium-111 (^{111}In) (Wernick & Aarsvold, 2004), while PET detects photon pairs resulting from the annihilation of positrons produced in the β^+ decay of particles such as fluorine-18 (^{18}F), oxygen-15 (^{15}O), nitrogen-13 (^{13}N) and carbon-11 (^{11}C) (Saha 2005). Though simple, this distinction is important since the choice of particle restricts how it may be used in tracers for nuclear medical imaging studies. The radiopharmaceuticals are formed by incorporating the radiotracer into a pharmaceutically active molecule which is then injected, inhaled or otherwise introduced to the patient and subsequently detected within the body at sites based on the physiological effect of that molecule. The tracers used in PET are of particular interest since they can be used to form analogs of common biological molecules. For instance, ^{18}F is used to produce ^{18}F-fluorodeoxyglucose (FDG) which is analogous to glucose and can be used to indicate levels cellular metabolism, and ^{11}C is used in ^{11}C-L-methionine, analogous to the amino acid, which indicates cancer malignancy based on amino acid utilization (Saha, 2005). Conveniently, these particles also feature short half lives (^{18}F 110 minutes, ^{15}O 2 minutes, ^{13}N 10 minutes, and ^{11}C 20.4 minutes) relative to SPECT isotopes (^{99m}Tc 6 hours, and ^{123}I 13.22 hours) which results in lower cumulated doses and reduced periods of radioactivity for patients (Wernick & Aarsvold, 2004), though it is prudent to mention that half lives of many durations have applications within nuclear imaging.

The result of the versatility of PET radiotracers is that PET has a wide range of imaging applications. PET is currently being used various fields, including: oncology for cancer diagnosis, staging, and therapy (Rohren et al., 2004); cardiology in myocardial perfusion and viability studies, and coronary artery disease (Keng, 2004); and neurology in the study of epilepsy, movement disorders, and Alzheimer's disease (Valk et al., 2005; Kadir et al., 2012). While radiopharmaceutical research will provide new applications for PET, improving the electronic system's capabilities can provide new imaging techniques to increase the effectiveness of PET in current applications and open the door to new ways to apply PET in healthcare.

In order to better understand how to improve PET system capabilities, it is useful to understand the physics and electronics that are integral to such a device. Looking at recent developments in relevant technology reveals potential avenues to explore or overlooked research opportunities. The following sections hope to provide a more in-depth look at PET systems.

1.1.1 PET Physics

As mentioned, PET systems make use of positron emitting isotopes. This form of radioactive decay is also known as β^+ (beta-plus) decay and occurs primarily in low Z nuclei that are proton-rich according to the following equation (using sodium-22, ^{22}Na, as an example):

$$^{22}Na \rightarrow {}^{22}Ne + e^{+} + v \tag{1.1}$$

where e^+ represents the positron (sometimes denoted β^+), v represents the neutrino which is also emitted but not detected in PET systems (Allen et al., 1955; Cherry et al., 2003). The energy of the positron is relative to the resulting daughter nucleus and neutrino as the transition energy is shared between them. The positron can be emitted with a variety of energies determined by the atomic mass difference of parent and daughter nuclei and any γ-rays that are also emitted due to excited states resulting from the transition to the daughter nucleus, in the case of ^{22}Na this γ-ray has a value of 1.27MeV (Allen et al., 1955) . Positron decay is in competition with another form of radioactive decay that has the same effect on the parent nucleus called electron capture (EC). Equation 1.2 illustrates EC using ^{22}Na:

$$^{22}Na + e^- \rightarrow {}^{22}Ne + v \qquad (1.2)$$

where *e*- indicates the inner shell electron that is captured in the event. In EC, additional emissions may be found in the form of x-rays or Auger electrons when the electron vacancy is filled, and γ-rays via the same mechanism as in β^+ decay (Cherry et al., 2003, Cherry et al., 2006). In EC there is no positron emission and thus PET does not focus on detection of EC events, though they will be present in some relevant radioisotopes. The relative proportions of these decay methods can be found in reference tables or by examining the decay schemes for that radioisotope as shown in figure 1.1. Because of their low atomic numbers, out of the four most common PET radionuclides (^{18}F, ^{15}O, ^{13}N and ^{11}C) only ^{18}F will experience EC (Cherry et al., 2006).

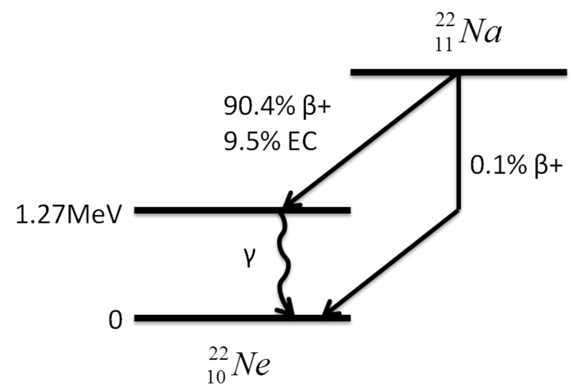

Figure 1.1 Decay scheme for ^{22}Na showing relative proportions of β^+ and EC decay methods. Note that the daughter nucleus, Ne, is initially in an excited state until it emits a γ–ray with energy equal to 1.27MeV (Lima, 2011).

After the positron is emitted it will travel through surrounding matter losing energy as it interacts and subsequently scatters (Bailey et al., 2005). The distance the positron travels is relative to the energy of the particle. The positron emitted by ^{18}F for instance, travels a maximum distance of 2.4mm in water (Bailey et al., 2005). As the positron approaches rest it will combine with an electron from surrounding atoms and, occasionally after a brief existence forming a particle known as positronium, the mass of the two particles is converted to electromagnetic energy in an annihilation event (Knoll, 2000). Assuming the two particles were initially at rest, using Einstein's mass-energy equivalence we can find the total energy that is produced:

$$E = mc^2 = m_p c^2 + m_e c^2 \qquad (1.3)$$

where m_p and m_e represent the mass of the positron and electron, respectively (both $9.1\text{x}10^{-31}$ kg) and c is the speed of light in a vacuum ($3\text{x}10^8$ m/s) (Cherry et al., 2006). The resulting energy is 1.022MeV and is emitted from the site of annihilation in the form of annihilation photons. Since the particles were assumed to be at rest and both momentum and energy must be conserved the resulting annihilation photons must be emitted in directions that satisfy this conservation. In approximately 99.97% of annihilation events, two photons are emitted in opposite directions (180^{o} to one another) with energy of 511keV (Cherry et al., 2006). These photons are the focus of PET imaging, which uses their anti-parallel momentum and specific energy to determine the position of the initial positron emitter.

To detect these annihilation photons PET systems make use of scintillation crystals and photo-detectors which will be discussed in section 1.1.2. These detectors are usually placed in a ring formation around the patient, although, partial ring or parallel plate geometries are also used, particularly for anatomy specific systems such as Spanoudaki, Lau, Vanderbroucke, and Levin's (2010) breast dedicated system. Figure 1.2 shows the detection scheme for a PET imaging system using a detector ring. The line of response (LOR) is formed by interpolating a line between the two detectors that were hit by a photon and is used to estimate the position of the positron emitters and reconstruct the image representing those locations. In order to determine which two detectors should be used to form a line of response coincidence gating (or time gating) is used. Assuming these photons are moving close to the speed of light, *c*, and the diameter of the ring is *x* cm, we know that any annihilation photons emitted inside the diameter of the ring will reach the detector in at most:

$$\frac{x}{c} = \frac{x\ (cm)}{3x10^{8}(m/s^{2})} = \frac{x}{30} ns \qquad (1.4)$$

Any incident annihilation photon pairs detected more than this time interval apart could not have come from the same annihilation event and thus the typical timing window used to determine coincidence is around this value, though not exactly, as will be discussed in section 1.1.2.

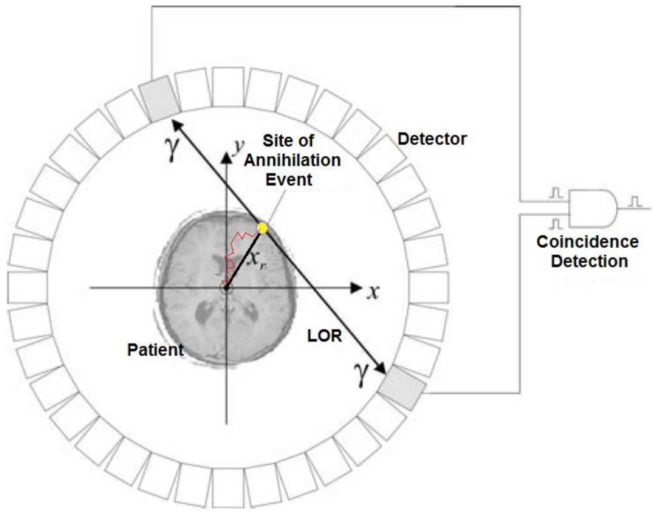

Figure 1.2 Detection scheme for a PET imaging system. The positron emitter situated at the origin of the axes emits the particle that follows the path marked in red (distance exaggerated for illustration purposes) until it annihilates with an electron at the indicated site. Annihilation photons, indicated by γ are emitted in opposite directions and are detected by the shaded detectors. The arrival times of these photons are compared in a coincidence detection stage that aids in ensuring the photons came from the same annihilation event. x_r indicates the positron range from the site of decay. LOR indicates the line of response determined by the detectors. Adapted from Wernick & Aarsvold (2004).

Assigning this LOR makes another assumption: that the photons travelled in straight lines exactly opposite one another. As noted in the case of the positron, particles travelling through matter will interact and lose energy in a process called attenuation. This attenuation can be described by the linear attenuation coefficient, μ_l, which represents the sum of the probabilities of a γ-ray interacting with matter via either the photoelectric effect, Compton scattering, or pair production, per unit area (Knoll, 2000). Though this is a stochastic process, equation 1.5 gives the expected attenuation of a narrow γ-ray beam passing through a material:

$$\frac{I}{I_o} = e^{\mu_l x} \tag{1.5}$$

where I is the attenuated beam, I_o is incident beam, x is the distance travelled in the medium, and μ_l is the linear attenuation coefficient which generally decreases with the energy of the radiation and increases with the atomic number and density of the medium (Knoll, 2000; Saha, 2005). The energy dependence of μ_l is convenient since PET depends on high energy photons which are less likely to interact with tissue than those of low energy such as in CT. Nonetheless, 511keV photons will still interact with tissues via the photoelectric effect and Compton scattering in proportions favoring the latter, as the probability of photoelectric effect is higher in low energy or high Z materials, and pair production requires incident energies larger than 1.022MeV (Knoll, 2000).

The photoelectric effect involves the absorption of the incident photon and ejection of a photoelectron whose energy is equal to that of the incident photon minus the binding energy of the electron. The probability of this process occurring is roughly proportional to Z^5/E^3 and competes with Compton scatter, both illustrated in figure 1.3 (Saha, 2005). After the ejection of the photoelectron, the vacancy is filled by an outer shell electron or the emission of an Auger electron. In the former case, characteristic x-rays are emitted that are determined by the energy difference of those shells. In Compton scatter, instead of the incident photon being absorbed it is deflected at an angle θ relative to its original direction after colliding with an outer-shell electron (assumed to be at rest) and transfers to it a portion of its own energy. The energy transferred depends on θ and is given in equation 1.6:

$$E_{sc} = \frac{E_o}{1 + \frac{E_o}{m_e c^2}(1 - \cos\theta)} \tag{1.6}$$

where E_{sc} is the energy of the scattered photon, E_o is the energy of the incident photon, θ is the scatter angle relative to the initial direction, and $m_e c^2$ is the rest-mass energy of the electron (511keV) (Knoll, 2000). Setting E_o equal to 511keV, we see that the minimum energy of a scattered photon resulting from a deflection of 180^o is $E_o/3$, or ~170keV; conversely, the maximum energy deposited by a 511keV incident photon will be

~341keV resulting from Compton scatter. The angular distribution of scattered photons is given by the Klein-Nishina formula, and indicates a tendency for forward scattering in energies relevant to PET (Knoll, 2000).

As a result of Compton scatter, it is possible that two photons that are detected within the appropriate time window produce a LOR that does not accurately represent the location of the initial positron emitter. Figure 1.4 shows the sources of noise when attempting image

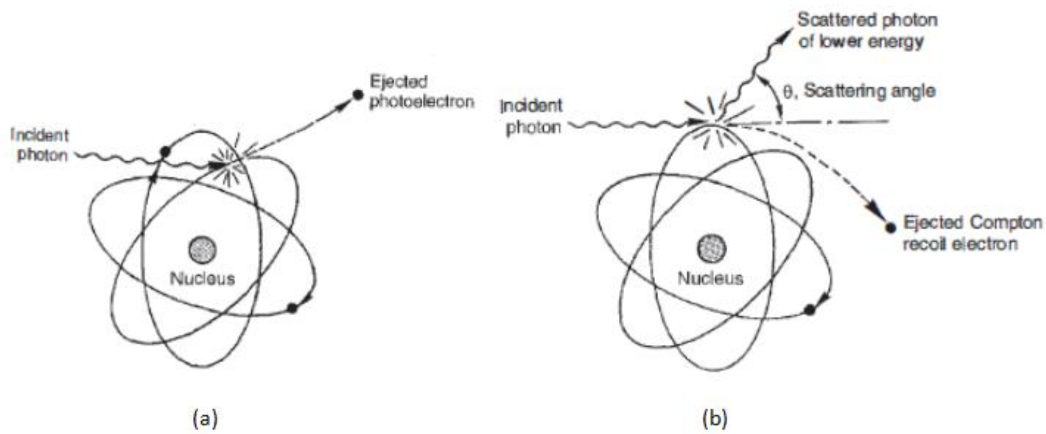

Figure 1.3 (a) Illustration of the photoelectric effect. The incident photon ejects a photoelectron and is absorbed. (b) Illustration of Compton scatter. The incident photon ejects a recoil electron but is deflected, not absorbed. The energy of the recoil electron is relative to the scattering angle, θ, and the energy of the incident photon. This figure is reproduced from (Cherry et al., 2003).

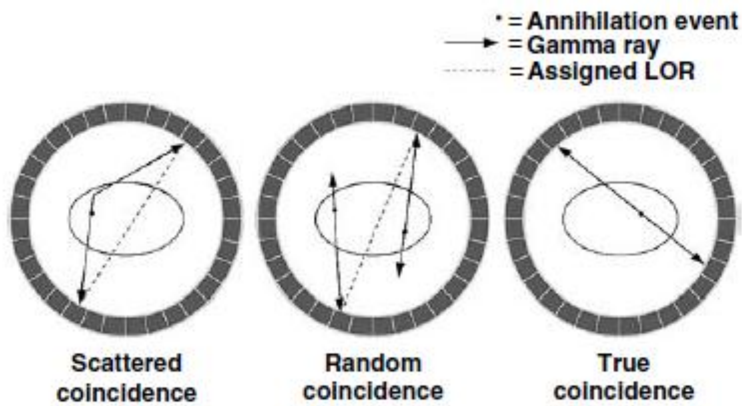

Figure 1.4 Coincidence detection events within a PET system. These three modes may all appear as a coincidence event to a detection system, but only the true coincidence should be considered when assigning the LOR. PET systems use time and energy gating to reduce occurrences of scattered and random coincidence being counted. This figure is reproduced from (Wernick & Aarsvold, 2004).

reconstruction using the LORs, scatter coincidence and random coincidence. Scatter coincidence occurs as a result of Compton scatter and adds a background noise signal to image reconstruction. Since the energy of the scattered photon must be less than 511keV due to equation 1.6, scatter coincidence can be rejected by using an energy window. One property of the detectors in PET systems is the ability to determine the energy of incident photons and by rejecting photons whose energy is determined to be outside of some window centered at 511keV, scatter coincidence can be reduced. Random coincidence occurs when many true events or scatter events coincide and strike two or more detectors within the time window. Unlike scatter coincidence, the photons in these events have not necessarily lost energy. In the case of more than two detectors being involved, true coincidence can be determined if only one candidate would exist inside the FOV of the detector, otherwise all are discarded (Cherry et al., 2006). To effectively reduce occurrences of random coincidence PET systems use a small time window, though because of the physical limitations of system timing performance random coincidence cannot be entirely eliminated in this way.

1.1.2 PET Detectors and System Properties

This section will describe the PET system in more depth with a focus on the detectors themselves and the parameters used to describe the system performance and the factors that affect them. The general form of a PET detector includes a scintillation material, to convert the annihilation photon into visible light, and a photo-detector that is sensitive to the emissions of that scintillator to convert it into an electric signal, as shown in figure 1.5.

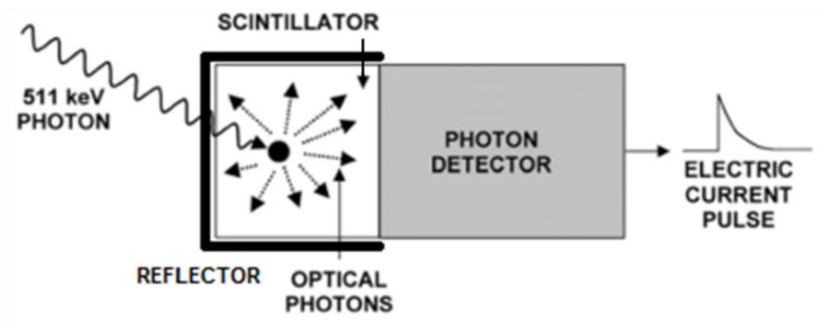

Figure 1.5 General design of a PET detector. The resulting electric current pulse is processed by the front-end electronics of the system which may include a pre-amplifier and noise filter. This figure is adapted from (Cherry et al., 2006).

A scintillator crystal converts the energy deposited by incident γ-rays during attenuation into visible light photons in a process called luminescence. In this process, electrons from the valence band in the scintillator (those bound to the crystal lattice) are excited into the conduction band (mobile electrons) and leave a vacancy, or 'hole,' in the valence band. When another electron from the conduction bad drops into this hole, its excess energy is emitted as light photons with energy slightly less than the gap between these bands (Wernick & Aarsvold, 2004). The number of electron-hole pairs produced relative to the deposited energy is known as the conversion efficiency. This light is emitted isotropically within the scintillator and thus the material is usually wrapped in a reflector to guide the photons towards one open face where the detector is located. The experiments conducted in this thesis use a fast scintillator, lutetium orthosilicate (LSO) that is common in PET applications.

The photo-detector most commonly used in PET systems is the photomultiplier tube (PMT). PMTs are common in scintillation detectors due to their large area, fast time response, high sensitivity, high gain and low noise (Ahmed, 2007). A PMT is composed of a photocathode, an electron multiplication scheme, and an electrode. The photocathode converts the scintillation light into photoelectrons through the photoelectric effect which are transmitted to the electron multiplication stage. Common photocathode materials are bialkali and multialkali variants, mostly composed of alkali metals, and are sensitive in the 200-850nm spectrum which is ideal for many common scintillators (Wernick & Aarsvold, 2004). This spectral response of the photocathode is also known by the common detector property, quantum efficiency, which is a measure of the number of charge carriers produced relative to the number of incident photons.

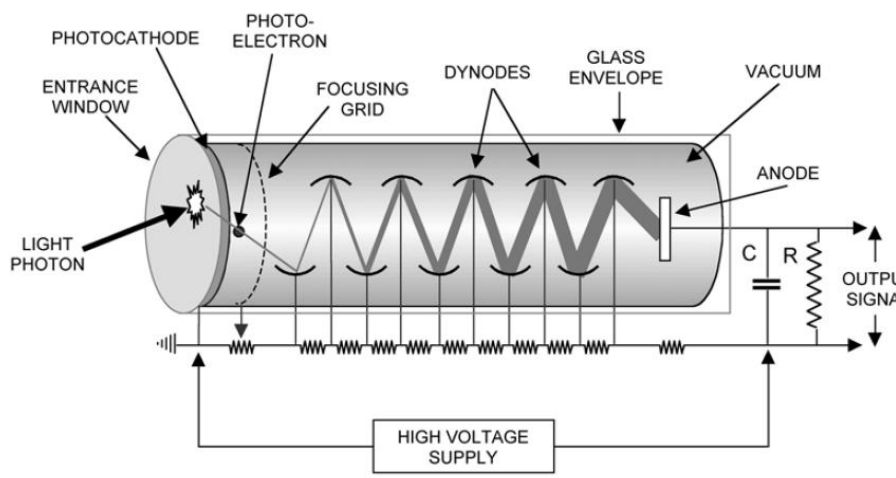

Figure 1.6 Schematic of a typical PMT. The light photon is emitted from the scintillator (not shown). The dynodes are held at increasing voltage increments and form the electron multiplication stage of the detector. This figure is reproduced from (Cherry et al., 2006).

The operation of the PMT is illustrated in figure 1.6 which reveals the electron multiplication stage, the dynodes. Each dynode is held at a higher voltage potential than the previous one in the stage. This potential difference causes emitted photoelectrons to accelerate towards the dynode. When the electron strikes the dynode at high velocity, the plate emits secondary electrons which accelerate towards the next plate (Ahmed, 2007).

These plates are specifically shaped and arranged to maximize the collection of secondary (or initial) electron emissions. The number of secondary electrons depends on the voltage differential between dynodes, but a good estimate is 6 for the first stage and 4 for subsequent stages, resulting in gains >10^6 in PMTs with 10 or more dynodes. Recent work has investigated the use of solid state detectors to fill the role of the PMT, and will be discussed further in section 1.3.

There are many parameters used to characterize the effectiveness of a PET system and perhaps the most visible is the spatial resolution. Spatial resolution is related to the sharpness of an image produced by a system, and can be described as the minimum required size of a feature to be distinguishable or detected in the image. This parameter is defined by the point spread function (PSF) of the system, which is the resulting signal distribution when the input is a single point. The PSF can vary with direction, and is often represented as a 2-dimensional Gaussian function. If this Gaussian function has a standard deviation, σ, then the distance of resolution is 2.35σ, a value known as the full-width at half-maximum (FWHM) of the function (Lima, 2011). There are many factors that affect the spatial resolution of the system. Equation 1.7 attempts to describe the contribution of these factors and was derived empirically by Derenzo et al. in 1993 for systems using block detectors.

$$\Gamma = 1.25\sqrt{\left(\frac{d}{2}\right)^2 + \left(0.0022D\right)^2 + r^2 + b^2} \qquad (1.7)$$

In this equation, d represents the width of a single crystal detector, D represents the diameter of the system, r represents the effective size of the source (including positron range), b represents an empirically derived factor describing the uncertainty in the position of the photon detection within the detector, the factor 1.25 is to account for distortion during image reconstruction, and Γ is the spatial resolution. The two most limiting factors are expected to be D and r due to the difficulty in alleviating their effects. As discussed, the positron has a range associated with its emission that will introduce uncertainty as to the location of its emitter, imposing a fundamental limitation on PET spatial resolution. Though Hammer et al. (1994) showed that the presence of a strong magnetic field can reduce the positron range effect this generally requires field strengths greater than 5T which are usually reserved for animal studies. The inclusion of the system diameter arises from the assumption that positron annihilation occurs with particles at rest. In reality, due to residual momentum at the moment of annihilation the colinearity of the photon pair can vary by up to 0.25^{o} from 180^{o} (distribution of ~0.5^{o} FWHM) which will affect the spatial resolution in a way that is directly proportional to the diameter of the ring (Derenzo et al., 1993; Lima, 2011). This is another fundamental limitation on PET spatial resolution and can only be alleviated by using smaller rings; for instance, a standard 80cm bore will have a minimum spatial resolution of 1.76mm from this non-collinearity effect alone. The other factors, *d* and *b*, can be improved by reducing the size of detector scintillator pixels and increasing the SNR of the detector, respectively.

Due to an effect known as parallax error this spatial resolution varies with axial position and degrades towards the periphery of the FOV. This effect arises due to the way the LOR is calculated in simple detector designs. In the case of an annihilation event occurring near the edge of the FOV, the photons may enter detector scintillators at oblique angles often after passing through neighboring detectors without interaction (Bailey et al., 2005). However, early detectors did not include this information in construction of the LOR, which was subsequently drawn from the end face of the scintillator as shown in figure 1.7. This error results in an offset of the assigned LOR from the actual flight path relative to the depth within the crystal that the light photons were produced and orientation of the detectors. Recent designs that take the depth of interaction into account are able to alleviate the parallax error and are discussed in more depth in section 1.1.3.

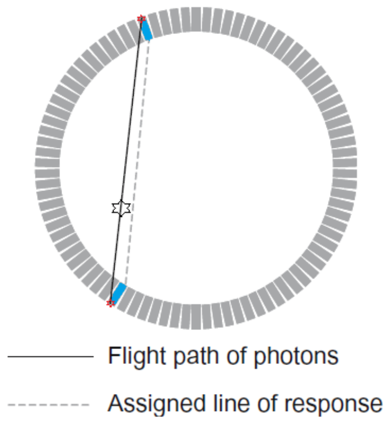

Figure 1.7 Illustration of depth of interaction. Annihilation at the site marked by the star produces photons near the edge of the detector. These photons penetrate nearby detectors before being absorbed in the detector pair marked in blue. This pair then draws the LOR from their entrance faces, shown as the dotted line. This figure is adapted from (Bailey et al., 2005).

Before any of these factors are taken into account the system must be able to confirm that the detected photons represent a true event and it does this by using energy and timing measurements. Energy resolution is a detector property that indicates the ability of the detector to determine the energy of an incident beam of monoenergetic photons. The energy resolution, R, of a photopeak in an energy spectrum is mathematically defined in equation 1.8,

$$R = \frac{FWHM}{E_0} = \frac{2.35\sigma}{E_0} \tag{1.8}$$

where $FWHM$ is the FWHM of a Gaussian function fitted to the peak with standard deviation σ, centered at E_0, and is conventionally a unit-less percentage assuming any superimposed baseline or continuum has been removed (Knoll, 2000). A lower energy resolution indicates better ability to differentiate photons of similar energies, typically two energy peaks are considered differentiable if they are separated by more than one FWHM of the detector's resolution. Figure 1.8 illustrates a typical PET energy spectrum, a histogram of all energy readings made by the detector, showing photopeaks centered at 511keV. There is usually a continuum of energy readings that must be accounted for in the calculation caused by background radiation, scatter within the detector, and in some scintillators, such as LSO, self illumination.

Ideally, the energy spectrum will feature a delta function centered at the energy of incident photons, but due to fluctuations in photon and charge production, and noise sources in front end electronics, this is not the case. In a linear detector, the centroid of the photopeak E_0 is directly proportional to the number of charge carriers produced in the detector, N, by some constant k (Knoll, 2000).

$$E_0 = kN \tag{1.9}$$

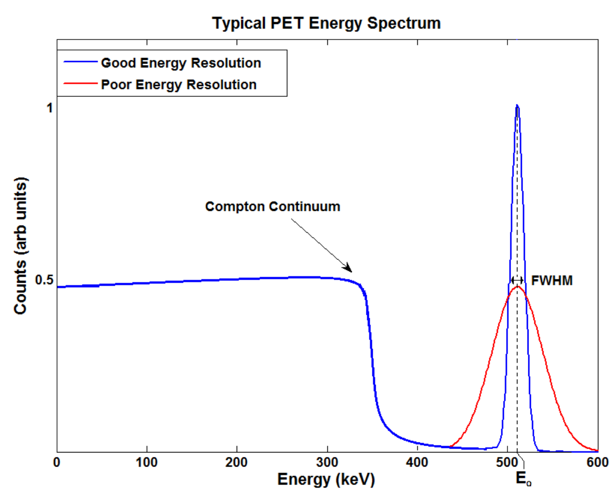

Figure 1.8 A typical PET energy spectrum. The FWHM of the peak featuring good energy resolution is indicated on the graph. The center of the 511keV energy peaks is indicated by E_o. These two properties of the spectrum determine the energy resolution of the system. The Compton continuum is also indicated, representing single scatter events resulting in the maximum deposition of energy from incident photons at the steep decline, and multiple scatter and multiple interaction events resulting in energy distributions between the Compton edge, photopeak, and beyond.

If Poisson statistics are assumed for the generation of these charge carriers, then the standard deviation of the charge carrier distribution, σ, is proportional to the square-root of *N*. Substituting this equivalence and the results of equation 1.9 into equation 1.8, equation 1.10 gives the theoretical limit, R_{lim}, of energy resolution due to charge carrier statistics:

$$\sigma = k\sqrt{N}, \quad \therefore R_{\lim} = \frac{2.35k\sqrt{N}}{kN} = \frac{2.35}{\sqrt{N}} \qquad (1.10)$$

In order to express this limit for detection systems which do not exactly exhibit Poisson statistics the Fano factor is introduced (Knoll, 2000). The Fano factor, *F*, relates the observed variance, σ^2, of a detector's charge carrier production to the theoretical Poisson variance and the equivalent expression for R_{lim} becomes:

$$R_{\lim} = \frac{2.35k\sqrt{N}\sqrt{F}}{kN} = 2.35\sqrt{\frac{F}{N}} \qquad (1.11)$$

This result is most relevant to solid state detectors or proportional counters where *F* can be very small (on the order of ~0.1 or less), while scintillation detectors appear to follow Poisson limitations (Zulliger and Aitken, 1970; Knoll, 2000). Assuming a factor of 0.05, a germanium detector would capable of 1% energy resolution with as little as 2762 charge carriers, while a scintillation detector would require over 55000.

These equations assume that variance among carrier production is the only source of fluctuations in the signal but this is not technically correct. Every step along the signal chain will add noise, however negligible. Many detectors suffer from thermal carrier generation, many detectors have wavelength dependent quantum efficiency, active circuit components have a bandwidth dependent noise spectrum, and passive components exhibit thermal noise. All of these independent noise sources, if symmetric, shape the overall response function like a Gaussian distribution, and their contributions can be summed in quadrature (Knoll,2000):

$$(FWHM)^2_{overall} = (FWHM)^2_{statistical} + (FWHM)^2_{noise} + (FWHM)^2_{detector} + \ldots \qquad (1.12)$$

where each term is the equivalent degradation of the overall FWHM independent of other sources. Finally, the energy resolution determines the energy window to apply to incoming photons to determine how to classify them. A typical window is 350-650keV, though this can be reduced based on energy resolution to reject more cases of pile-up (multiple annihilation photon interactions within a scintillator within the time window) (Cherry et al., 2006).

Coincidence timing resolution is analogous to energy resolution but is instead relative to the ability of the PET system to determine exact time differences between two detection events. Unlike energy resolution, coincidence time resolution is characterized only by the FWHM of a Gaussian distribution fitted to the time spectrum; the centroid of the function is not as important as the accuracy of the measurement. Typically, the time window used by the system to reject random coincidences is set to 3 to 4 times the timing resolution, though in very accurate systems the size of the detector ring may impose a minimum requirement on this window according to equation 1.4 (Bailey et al., 2005). Though it may seem to be a simple task, fluctuations that confound the measurement are always present and can be divided into two categories: time jitter, for noise sources affecting timing measurements of a series of identical pulses, and amplitude walk, for variations in signal shapes.

Timing jitter is caused by many of the same sources that contribute to degradation of the energy resolution: Poisson statistics, amplifier noise, and the others that have already been discussed. Amplitude walk is the larger of the two contributions and is related to changes in the signal shape, particularly the rise time which is typically the portion of the signal with the highest frequency components, which occur when the amplitude of the signal changes and subsequently changes the slope of the edges. The most common method for timing pick-off is the simple leading edge trigger threshold. Knoll has documented the other most prevalent methods in his recent edition of Radiation Detection and Measurement in chapter 17 (2000). The effect of amplitude walk on a system utilizing leading edge triggers is illustrated in figure 1.9.

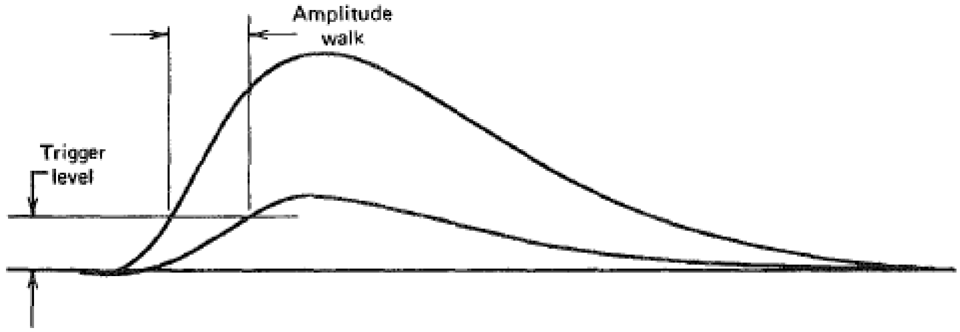

Figure 1.9 Illustration of the timing uncertainty introduced by amplitude walk. Changes in the amplitude of scintillation signals result in proportional changes to trigger detection time, resulting in reduced time pick-off accuracy. This figure reproduced from Knoll (2000).

These effects can be related to the limit of timing resolution, τ_{lim}, by equation 1.13, showing the dependence of the timing spectrum FWHM on the slope of the rising edge and its root-mean-square (rms) noise, σ_{noise} (Radeka, 1974; Spanoudaki et al., 2007).

$$\tau_{\lim} = \frac{\sigma_{noise}}{\frac{dV}{dt}} \qquad (1.13)$$

Clearly, the best ways to improve timing performance are to increase signal-to-noise ratio (SNR) and reduce the effect of amplitude walk. Even though there is a minimum requirement for the coincidence time window set by the system dimensions, improvements in time resolution are able to provide SNR improvements during image reconstruction using methods discussed in section 1.1.3.

With energy and timing windows in place, the sensitivity of the system is the final major system parameter. The sensitivity of a PET scanner is the mean number of event counts per unit time relative to the actual activity of sources present in the FOV; it is expressed in counts per second (cps) per microCurie (μCi) or megaBecquerel (MBq). The sensitivity depends on a variety of factors including: the geometric efficiency of the system, the timing and energy window settings, the detection efficiency and system dead time. The factors that have not yet been discussed are explained here: the geometric efficiency of the system is defined by the solid angle projected by the source upon the detection apparatus which depends on the distance from source to detector ring and number of detectors; the system dead time is the minimum amount of time it takes for the detector electronics to effectively process a single coincidence event in the absence of pulse pile-up, and becomes more problematic as source activity increases (Saha, 2005). Based on these factors, the sensitivity of the system is described by equation 1.14 proposed by Budinger in 1998 for point sources at the center of the FOV:

$$S = \frac{A\varepsilon^2 e^{-\mu t} 3.7x10^4}{4\pi r^2}(cps/\mu Ci) \qquad (1.14)$$

where A is the area of the detector, ε is the detection efficiency, μ is the linear attenuation coefficient of the detector material of thickness t for 511keV photons, r is the detector ring radius and S is the true counts per second per microCurie of activity. A higher sensitivity implies improved image quality but does not explicitly state the relationship to image noise. For that figure, the noise equivalent count rate (NECR) is used as given by equation 1.15:

$$NECR = \frac{T^2}{T+S+R} \qquad (1.15)$$

where T, S and R are the number of true, scatter and random coincidence event count rates (Saha, 2005). The NECR is proportional to the SNR in the reconstructed image from sources related to the detector, and is a good indicator of system performance. Image noise from physiological sources (such as bladder uptake) and reconstruction (such as streaking or tearing) are not considered by the NECR (Saha, 2005).

Though certainly not exhaustive, these system parameters are able to provide an initial impression of system and detector performance. Some more recent developments in PET technology will be discussed in the following section.

1.1.3 Recent Developments

It has been mentioned that the minimum time window during acquisition is limited by the size of the detector geometry, so what purpose can be served by improving the system time resolution beyond satisfying this limit? If the timing of detection events was accurate to very small units of time, detectors would be able to localize the annihilation event to some portion of the LOR based on the time difference and the speed of light, given by equation 1.16:

$$\Delta x = \frac{c\Delta t}{2} \tag{1.16}$$

where Δx is the axial distance from the center of the FOV, c is the speed of light, and Δt is the difference in arrival time between the two annihilation photons. In this equation, there will be some uncertainty associated with Δt according to the time resolution of the system, and so instead of a single point where annihilation occurred, there is a position uncertainty centered there, whose width is determined in the same way, instead using the system time resolution in equation 1.16. After applying this method, during the image reconstruction stage a reduction in back-projection noise is achieved and SNR improved; this is the basis of time of flight (TOF) PET. In conventional image reconstruction, called filtered back projection, all of the pixels overlapped by the LOR are incremented causing statistical noise; other sources may be overlapped by that LOR and are also incremented. In TOF PET, only the region of position uncertainty is incremented using a distribution according to the time resolution; only nearby sources are at risk of being overlapped thus reducing statistical noise (Moses, 2007). Budinger (1983) developed framework showing that the SNR and sensitivity of the system is improved by TOF PET according to equation 1.17:

$$\frac{SNR_{TOF}}{SNR_{NO-TOF}} = \sqrt{\frac{D}{\Delta x}} \quad G = \frac{2D}{c\Delta t} \tag{1.17}$$

where D is the diameter of the object being imaged, Δx is as in equation 1.16, Δt is the arrival time difference, and G is the effective sensitivity gain.

Though postulated as early as 1969 by G. Brownell et al. (According to Allemand et al., 1980), scintillators appropriate to PET applications were either too slow, too insensitive (in the case of plastic scintillators), or had insufficient light output. The development of TOF appropriate scintillators (such as LSO, LYSO, $LaBr_3$:Ce(5%)) over the past few decades allowed TOF PET to become clinically available in late 2006 using LYSO crystals to achieve 600ps timing resolution (Surti et al., 2007). Combination of these scintillators with solid state photomultipliers, such as silicon photomultipliers (SiPMs), and faster PMTs has continued to improve results. Very recently, using LYSO or LSO crystals, groups have been able to achieve timing resolutions of 290ps and 400ps (5mm and 20mm lengths, using SiPM) (Yeom et al., 2011), ~400ps (10mm crystal length, using PMT and SiPM) (Cosentino et al., 2012), 279.6ps and 300ps (10mm crystal length, two different PMTs) (Ito et al., 2013) and as low as 220ps (10mm LSO crystal length, using many SiPMs) (Gundacker et al., 2012). Using even faster cerium doped $LaBr_3$ crystals, groups have been able to achieve time resolutions of 163ps and 249ps (5 and 30mm crystals, using SiPMs) (Wiener et al., 2011), 375ps (30mm crystal length, using PMTs) (Daube-Witherspoon et al., 2009), as low as 198ps (10mm monolithic crystal length, using SiPMs) (Seifert et al., 2012), and the lowest recorded value of 100ps (5mm crystal length, using SiPMs) (Schaart et al., 2010). These crystals are still not fast enough to result in improvements to spatial resolution, where Δx is less than the system's current spatial resolution. Faster crystals do exist (LuI_3:Ce, $CeBr_3$) but they are not widely used as of yet (Moses, 2007). As detector and scintillator technology continues to develop, TOF PET will strive towards its' theoretical ability to improve spatial resolution but currently is only capable of improving SNR.

Another development intended to improve spatial resolution, Depth of interaction (DOI) methods aim to alleviate the effects of parallax error and directly reduce the axial dependence of spatial resolution in PET systems. There are two main approaches to DOI:

detector configuration and crystal configuration, which can employ either continuous or discrete DOI detection. Some of these designs are given in figure 1.10:

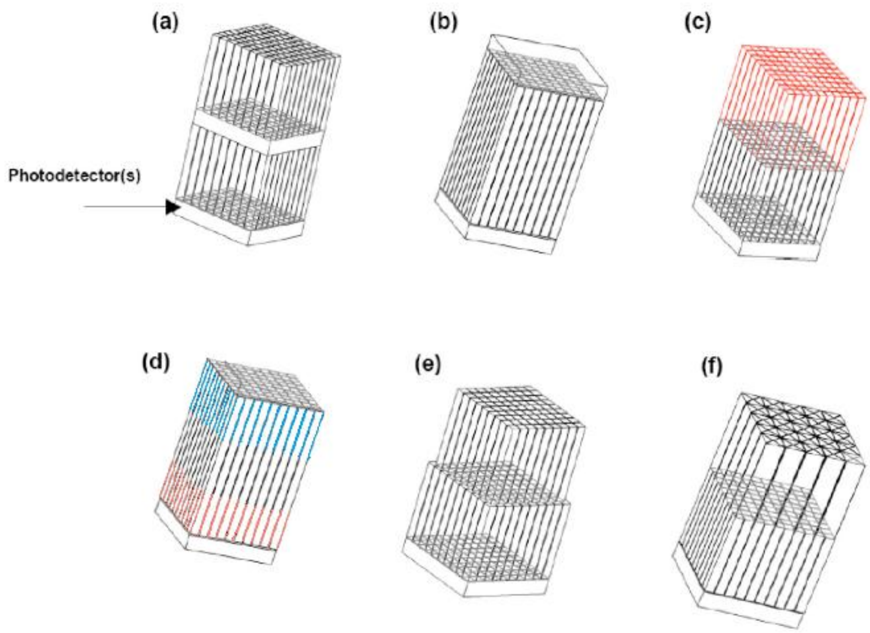

Figure 1.10 Illustration of several DOI design concepts for PET. (a) Dual crystal-photodetector(s) layers. (b) Single crystal layer with photodetectors at each end. (c) Phoswich design with two types of scintillation materials. (d) Depth dependent absorbers or reflectors. (e) Dual layer crystals with offset positions. (f) Dual layer crystals of mixed shapes. Adapted from Peng and Levin (2010).

Designs (a) and (b) from figure 1.10 represent discrete and continuous DOI detector configurations respectively. Configuration (a) has been investigated by some groups (Rafecas, 2001), and while this method does not compromise detector performance, in order to attain higher levels of DOI segmentation many detectors are required. Alternative edge-on versions have been used by (Levin, 2002; Vandenbroucke et al., 2010) to reduce wiring complexity, and with thin flexible printed circuits are able to reduce the dead-space that is introduced between scintillators to provide as low as 1mm DOI resolution. More recently, Gu et al. (2011) have used cadmium zinc telluride (CZT) solid state detectors in edge on configuration to also achieve 1mm 3D resolution. Configuration (b) uses the proportions of light gathered at each detector to determine the position of absorption to some statistical region. The advantage of this method is that it only requires two detectors for any DOI length, though some performance degradation can occur as reported by groups using solid state detectors (Yang et al., 2006; Shao et al., 2007; Kishimoto et al., 2013) that achieved 3D resolutions as low as 3.5mm, 4.5mm and 3mm, respectively.

Designs (c) and (d) from figure 1.10 are scintillator designs that attempt to differentiate the light produced within the scintillator block by using different scintillator materials as in (c), called phoswich design, or different reflector or absorber layers as in (d). Phoswich detectors employ pulse shape discrimination techniques to differentiate photon production in different scintillators based on their timing properties and pulse shape (Lewellen, 2008). This method is often expensive, and imposes a limitation on timing resolution based on the slowest scintillator and is discrete DOI based on the number of layers used. Nonetheless, this method is still being used by groups to achieve DOI resolutions of: 5mm using LuYAP and LSO crystals (Eriksson et al., 2010), 5-6mm using LGSO crystals of different Ce concentrations (Yamamoto et al., 2010), and 4mm using LSO and GSO crystals (Vaquerro et al., 2011) though much of the research focuses on discriminating the layers rather than pushing the limits of DOI. Similarly, using different surface treatments on different regions of scintillators will also change the signal characteristics. This method results in a continuous DOI measurement as the isotropic emission of photons will hit the nearest layers in proportion to their solid angle to the emission site. This method has been employed less often by groups, but has achieved DOI resolutions of: 3-4mm for groups using absorbers between crystals (Lewellen, 2008) and 4.2mm using reflectors of different geometric shapes (Ito et al., 2013).

The final two designs use scintillator positions and shapes to determine, discretely, the DOI. Design (e) offsets crystal layers and uses light sharing to determine the 2D position of the emitting crystal to identify it within the detector, and thus identify which layer emitted the photons. This method has recently been used by Thompson et al. (2011) to achieve 4mm and 6mm DOI steps in a PET/MR system, and 7mm DOI resolution by (Ito et al., 2010) using a four layer design. The final design, (f), uses a combination of crystal shapes and reflector schemes to differentiate crystal layers based on their 2D position encoding. Through clever use of the reflectors to influence light sharing, each crystal layer, though stacked vertically, produces a different light sharing profile for each crystal. Only one group has found to be using this method and achieved DOI resolution of 10mm using two and three layer designs (Inadama at al., 2008).

Though many of the groups whose work was discussed here achieved their results in bench top arrangements or using higher energy γ-rays, their developments look promising and will hopefully translate into clinical systems in the future.

1.2 Solid State Photomultipliers

Before recent developments in solid state photomultipliers (SSPMs) are discussed it is useful to investigate the physics behind their detection capabilities. SSPMs are comprised of semiconductors. Semiconductors are characterized as being able to act as both an insulator and conductor depending on how they are used. These material types are classified as such based on the energy required to excite charge carriers into conduction, known as the band gap energy, and their charge carrier density. An energy diagram of the charge carriers in semiconductors is shown in figure 1.11a, where the blue region represents electrons without enough energy to move from their position in the crystal lattice, called the valence band, and the yellow region represents empty energy levels that electrons could occupy to move freely, called the conduction band, and the white space between them represents how much energy an electron needs to jump to the next band, the band gap E_g, which is ~1eV in semiconductors (Serway and Jewitt, 2008). The distribution of electrons within these bands is temperature and Fermi level, E_F, dependent, and is given by the Boltzmann distribution (Ahmed, 2007):

$$f(E) = \frac{1}{1 + e^{(E-E_f)/k_b T}} \qquad (1.18)$$

where k_b is Boltzmann's constant, and T is temperature. At temperatures around 0K no electrons have enough energy to move to the conduction band in a semiconductor, while at higher temperatures, around 300K, there will be a distribution of electrons that are elevated to the conduction band through thermal excitation, leaving behind a hole. Figure 1.11b illustrates how these excitations cause charge carriers to move and produce current. In semiconductors of one element or compound these electrons and holes are in equal distribution, these are intrinsic semiconductors. By mixing in atoms with ±1 valence shell electrons relative to the intrinsic semiconductor, the compound formed is an extrinsic semiconductor and the process is called doping. In doped semiconductors, the additional electron or hole exists at an energy level either ~0.05eV below the conduction band or directly above the valence band forming an n-type or p-type semiconductor, respectively (Serway and Jewitt, 2008). This small energy difference is easily satisfied by thermal excitation and enters the conduction band; or conversely in p-type, an electron falls into the new hole, leaving a hole in the conduction band. Through doping, the properties of the semiconductor can be changed.

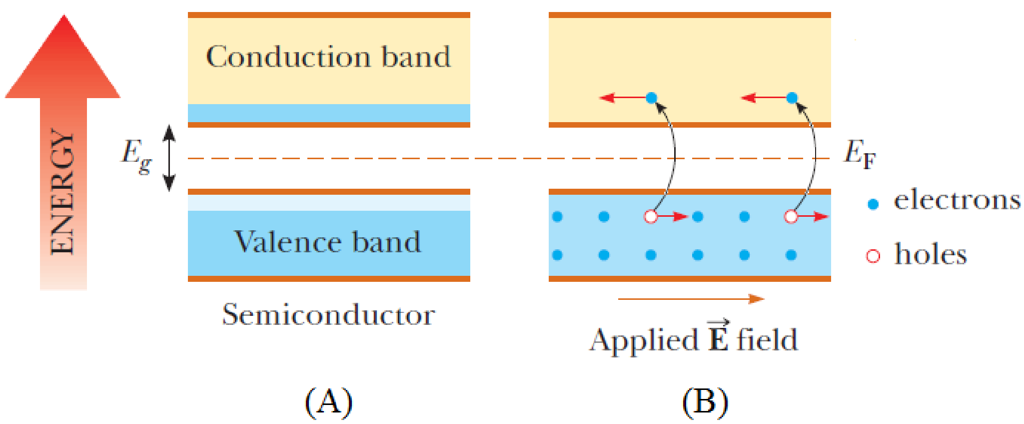

Figure 1.11 Illustration of energy bands. (a) Energy bands in a semiconductor at T>>0K, note that some electrons (shown in blue) are excited to the conduction band. (b) when an electric field is applied, excited electrons and holes left behind in the valence band move, producing current. Adapted from (Serway and Jewitt, 2008).

If n-type and p-type semiconductors are combined, the additional electrons and holes supplied by doping combine with one another at the interface between the two, migrating away from the interface. Once these charge carriers diffuse almost completely, the dopant atoms at the junction become ions that are locked into the lattice, positively charged in the n-type, and negatively in the p-type, forming a p-n junction. These charged particles form an electric field on the order of 10^4-10^6V/cm at the junction from n- to p-, and the charge carriers are no longer free to drift across and an equilibrium is found; this region becomes known as the depletion region (Serway and Jewitt, 2008). In this configuration, any electrons or holes generated in the depletion region are quickly pushed towards the n- and p- type regions, respectively, and only immobile charges are left in the depletion region; forming a high resistivity region. If an energized particle were to pass through this region of the device, it would transfer some energy to the charge carriers there and excite them into the conduction band according to the band gap, at which point the depletion region will sweep them away, forming current from the moving charges; this also applies to carriers generated by thermal activation or impurities (Knoll, 2000). This is the basic structure of the diode.

If an externally generated potential is applied across the p-n junction, positive with respect to n from p, the diode is said to be forward biased. The potential will overcome the depletion region and pull electrons from and push holes into the n-region, readily conducting current. If the diode were to be reverse biased, the potential difference between the two semiconductors is increased and the current would be restricted to whatever leakage occurs across the very small conductance of the region. Due to Poisson's equation for electrostatics, this reverse bias must also physically extend the range of the depletion region (Knoll, 2000). As mentioned earlier, ionizing radiation has the potential to energize electrons in the depletion region and cause current to be generated, and this process follows the interactions with matter discussed in section 1.1.1. The average energy expended by the ionizing particle to free the e-h pair is known as the ionization energy, ϵ, and is largely independent of the type of particle or its energy, but is inversely proportional to temperature. It can be inferred then that the physical width of this region is directly related to the sensitivity of the device to incident radiation. In order to increase the likelihood of interactions the depletion layer must be large. The size of this layer, *d*, is given by equation 1.19:

$$d = \sqrt{\frac{2\varepsilon V}{eN}} \tag{1.19}$$

where V is the applied voltage, e is the electron charge, ε is the dielectric constant, and N is the dopant concentration (often much higher on one side). It is evident that only the applied voltage can affect the size of the depletion region after doping, and the width is typically on the order of micrometers (Knoll, 2000). However, in many detectors this is not enough material to interact with high energy γ-rays reliably, and thus diodes are usually not suitable for direct radiation detection. To summarize: a reverse biased p-n junction diode or doped semiconductor that interacts with energized particles will produce a number of charge carriers proportional to its energy, and there we have the basis of solid-state detectors.

Semiconductor detectors have been in use in radiation detection for quite some time, yet most have not been compatible with PET designs due to their physical constraints – for example, the cooling requirement of germanium detectors to 77K, or the stopping power of silicon (Knoll, 2000). There is one recent semiconductor detector that looks promising: cadmium zinc telluride (CZT). CZT detectors have a higher effective atomic number, density, and a low intrinsic carrier concentration resulting in less thermal noise, and can thus be operated with acceptable SNR at room temperature (Ahmed, 2007). The result of the higher atomic number and density is improved stopping power, and thus an improved probability of photoelectric detection of incident γ-rays. The biggest benefit of CZT as a PET detector is that it does not require scintillation, and is therefore no longer at the mercy of Poisson noise from light photon emissions. In fact, the charge carrier production in SSPMs as a result of ionization follows a distribution that is less variable than Poisson distributions, governed by the Fano factor mentioned in equation 1.11, resulting in very low theoretical energy resolution limits.

There are two major drawbacks to CZT detectors. Firstly, CZT detectors suffer from low hole mobility; electron lifetimes are recorded at 0.1-several μs, while hole lifetimes 50-300ns. This is an intrinsic property of the material and can only be alleviated by increasing bias voltage (Ahmed, 2007). Secondly detector imperfections are a large problem for CZT, and contribute impurities which can add energy levels to the band gap and reduce device effectiveness.

Photodiode detectors are a more recent introduction to PET applications, particularly avalanche photodiodes (APDs). These devices offer a distinct advantage in that they can not only detect e-h pairs produced by ionization, but amplify the signal as well. However, these devices are not used to detect high energy particles directly and instead detect scintillation photons, much like PMTs. In order to ionize the device, the incident photons must overcome the ionization energy of the detector material, ~3.62eV for silicon (Ahmed, 2007).

The size of the depletion region in these devices must usually be large in order to detect scintillation photons from large area scintillators; areas larger than can be achieved by applying voltage as per equation 1.19. To achieve this a third layer of an intrinsic or lightly doped semiconductor is inserted between heavily doped n- and p- layers, forming the p-i-n structure often referred to as a p-i-n photodiode (Ahmed 2007). This process essentially fixes the depletion region to the width of the intrinsic layer. Additionally, another p-type region is introduced between the intrinsic, or π, layer and heavily doped n-type regions as shown in figure 1.12a. The result is that of a large depletion region with moderate electric field strength, and a small portion of this region with very large field strength as shown in figure 1.12b. Amplification occurs via a process called impact ionization. In the presence of a very high reverse voltage, the drift velocity of ionized electrons is so large that it may collide with other electrons in the depletion region, creating additional e-h pairs, which are in turn accelerated towards the electrodes creating new pairs in kind, called the avalanche effect. In the APD, primary ionization usually occurs in the region indicated by R_{abs} where the e-h pair will drift to their respective electrodes. Once an electron drifts into the R_{multi} region, impact ionization occurs and the number of carriers multiplies. This charge can be read out by appropriate electronics to read an electrical signal that is proportional to incident photon energy, and amplified on the order of 1000s to increase SNR. Noise in these detectors occurs via thermally generated carriers that initiate avalanches, and a small leakage current across the terminals as a result of the high voltage drop and extremely low conductivity of the depletion region, typically on the order of nA (Knoll, 2000).

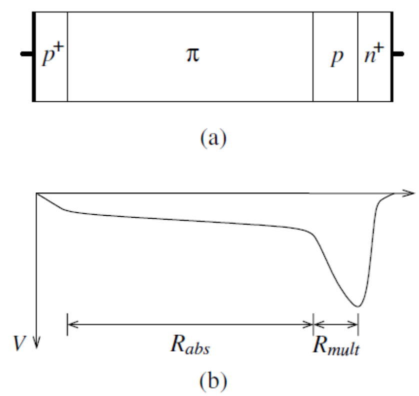

Figure 1.12 Illustration of the structure of an avalanche photodiode. (a) Orientation of the doped semiconductors. Electrodes indicated on either end. (b) The electric field profile of the device. R_{multi} indicates region of gain multiplication, and R_{abs} the absorption region. Image from Ahmed (2007).

An important distinction is that the applied reverse voltage for the APD is not unlimited. Above a certain voltage potential, V_{br}, called the breakdown voltage, the current produced is exponential, not proportional as shown in figure 1.13. When operated in this region, called Geiger mode operation, e-h pairs formed will both partake in an avalanche process that diverges until the response is saturated. At this point the reaction must be quenched to stop the avalanche, which is often achieved by an ohmic contact or external circuitry that reduces the voltage back below breakdown (Otte, 2006). Because nearly every carrier generation results in this saturation current, these are binary devices and not proportional to the incident photon energy. The area of a device operated above breakdown is limited by the rate of free carrier generation, since probability of thermal generation increases as the area of the depletion region does. These generations, called dark current, can reach count rates in the 100kHz to several MHz per mm^2 at room temperature, and emulate incoming photon events (Renker, 2006).

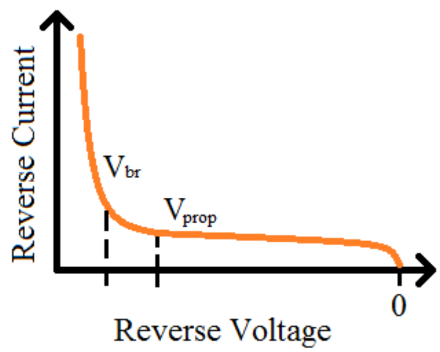

Figure 1.13 I-V curve for a reverse biased photodiode. V_{prop} indicates the region of proportional avalanche gain; V_{br} the region of exponential gain in the breakdown region.

Silicon Photomultipliers (SiPM) are devices composed of thousands of small area Geiger mode APDs called microcells in a large parallel array. Since each of the microcells is a binary device, SiPMs operate as scintillation photon counters. The output of the SiPM is the sum of all signals from the microcells. While the APD had gain in the 1000s, the SiPM has gain in the 10^5-10^6 range, and each microcell has gain given by equation 1.20:

$$G = \frac{C_{cell}}{e}(V - V_{br}) \tag{1.20}$$

where C_{cell} is the effective capacitance of the microcell (~fF), V is the applied voltage, V_{br} is the breakdown voltage, and e is the electron charge (McClish et al., 2007). These signals are fast due to the small microcell size and speed of gieger mode discharge (~1ns).

There are some limiting factors concerning the SiPM. First, the device contains a finite number of microcells and as such, at photon fluxes approaching the saturation of these cells non-linearities occur as many photons begin to strike the same microcell. The statistical relationship is such that linearity can deviate as much as 20% if the photon flux is equal to 50% of available microcells, and as such should be considered when designing a SiPM detector (Otte, 2006). An agitator to this factor is the recovery time of the microcell, which is more accurately related to the photon detection efficiency (PDE).

The PDE of the SiPM is related to the quantum efficiency (QE), effective area, breakdown probability and recovery time. The QE of silicon is quite high for light photons (80-90%) depending on wavelength (Renker, 2006). UV range photons do not tend to penetrate very deep into the material and the e-h pair is often lost due to short recombination times, but longer wavelength IR photons tend to penetrate more deeply and require larger depletion layers; the QE is affected by these factors (Otte, 2006). The effective area of the device is the ratio of sensitive area to overall area, and can be anywhere from 25%-80%. The breakdown probability is simply the probability that the initial e-h pair causes breakdown. This is related to the electric field strength but can often approach 100%. The recovery time is the period of recharge for a microcell. After firing, it takes the microcell <1us to recharge its capacitance. Due to dark noise, approximately 1% of microcells are in recovery at any given time (Otte, 2006). The product of all of these factors gives PDE in the range of 14% (SensL, 2011) to 50% (Hamamatsu, 2011) in recent devices.

Due to the arrangement of the SiPM array, optical crosstalk may occur. For every 10^5 carriers produced above the band gap of silicon, approximately 3 photons are emitted (Renker, 2006). These photons may go on to cause breakdown in nearby microcells, adding to the overall noise of the signal via this stochastic process. This effect can be reduced by using lower gain, or introducing a physical barrier between microcells, at the cost of gain or sensitive area. This cross talk, combined with the dark counts of individual microcells are the major sources of noise in SiPMs. Due to their much higher gain however, SiPMs still have an SNR advantage over large area APD detectors.

Despite these limitations, APDs and SiPMs have a major advantage over PMTs for PET applications: these devices are immune to magnetic fields (España et al., 2010). This, combined with their small size, lower voltage requirements, and comparable gain (in the SiPM) makes them an attractive alternative to PMTs as scintillation detectors for PET. This is especially true considering dual modality applications.

1.3 Multimodal Imaging: PET/MR

Magnetic resonance imaging (MRI) is a very versatile non-invasive imaging modality that can be used for high resolution imaging of both physiological structure and function. This section will introduce some basic MRI principles and then discuss the benefits and challenges associated with the development of an integrated PET/MR dual modality scanner.

1.3.1 Basic MRI Principles

MRI uses strong magnetic fields and radiofrequency pulses to extract valuable spatial and functional information from tissues. There are three main components of an MRI system: the main magnet, the gradient coils and the radiofrequency coils.

There are some basic principles that must be introduced before discussing these components. The components of an atom, the nucleus, electrons, protons and neutrons, are spinning along their own axes. A moving, unbalanced charge will induce a magnetic field about itself in a direction and size referred to as its magnetic moment. In atoms with odd numbers of protons and mass number, for instance hydrogen, there is a net magnetic moment resulting from the vector sum of all moments within the nucleus (Westbrook, 2002). In the presence of an external magnetic field, *B*, these moments will align themselves either parallel or antiparallel with the direction of that field. The ratio of parallel to antiparallel nuclei is calculated by the Boltzmann distribution and results in a net magnetization vector, denoted M_0, in a volume of tissue that is aligned parallel with *B* at room temperature (McRobbie et al., 2002). Since these nuclei had a net spin, their interaction with *B* actually causes their magnetic moment to precess (spin gyroscopically) about the axis of B at an angular frequency defined by the Larmor equation (Haacke et al., 1999):

$$\omega = \gamma B \tag{1.21}$$

where ω is the Larmor frequency of precession, and γ is the gyromagnetic ratio of a specific nucleus. The important note here is that specific nuclei, usually the proton of hydrogen, will precess at a very specific, calculated frequency according to the external magnetic field and at equilibrium all affected nuclei precess out of phase. The first component of the MRI system provides this magnetic field. The main magnet in clinical systems is usually a superconducting magnet that is cooled by liquid helium, is cylindrical in shape, and produces a strong, uniform magnetic field denoted B_0 along its axis defined as the *z* axis. This field is on the order of Tesla (T) while the net magnetization vector of water at body temperature is ~0.02μT/ml (McRobbie et al., 2002).

The second component of the MRI system is the gradient coils. These coils are placed inside the main magnet coils in various configurations in order to produce additional magnetic fields parallel to B_0. However, the fields produced by these coils are designed to vary linearly in strength along the three spatial dimensions in a controlled fashion, leaving the isocenter of the system at B_0. The result is that by varying the current through these coils, the magnetic field within the system changes as a function of *x, y* and *z,* and thus spatially encodes the frequency of a volume within the imaging field of view (Westbrook, 2002). By measuring the frequency and relative phase of the net magnetization vectors they can be localized within the field of view to produce volumetric images based on their amplitude.

The final component of the MR system is the radiofrequency (RF) coils, often combined into one transceiver coil, which are used to measure the properties of M_0. Due to the difference in magnitude of M_0 and B_0 it is difficult to measure M_0. However, if M_0 were aligned in the transverse plane, orthogonal to B_0, even such small magnitudes could be detected by a coil that is tuned to only measure magnetization in that plane. The transceiver coil fulfills both of these requirements by emitting RF pulses and then detecting the result. Using the principles of resonance, by applying a RF pulse orthogonal to the B_0 field at the exact Larmor frequency of a specific nucleus those nuclei will gain energy and begin to precess exactly in the transverse plane at that same frequency with no net magnetization along *z*, described as being tipped 90^o (McRobbie et al., 2002). The key here is that the precessions of all affected nuclei are put into phase by the RF pulse, and thus M_0 rotates in the transverse plane about B_0, shown in figure 1.14. This new net magnetization, isolated from B_0, can be detected by the same resonance principle using a coil tuned to the Larmor frequency in the transverse axis. By enabling the gradient coils, and changing the frequency of the RF pulse a specific volume of the field of view is excited due to differences in their Larmor frequency. The amplitude of M_0 in the transverse plane is determined by many factors, the most important of which are: the properties of the RF and gradient sequences, and the ability of nuclei in the volume to absorb energy (Westbrook, 2002). Conveniently, the composition of tissues affects the ability of nuclei to absorb and release energy from the RF pulse and this is the key to the contrast between tissues in MRI.

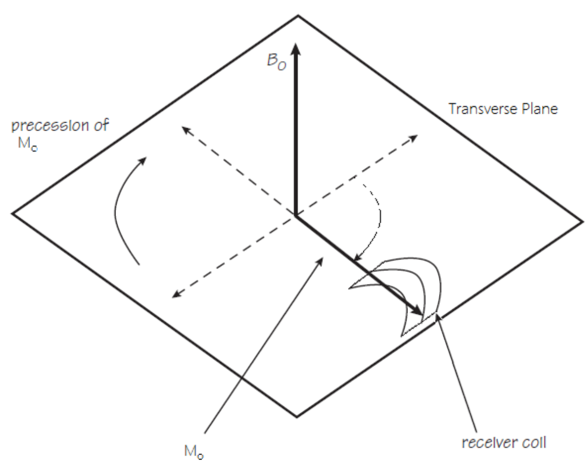

Figure 1.14 Illustration of net magnetization vector M_0 precessing in the transverse axis after an RF pulse. The receiver coil is tuned to resonate with M_0 only in the transverse plane. Adapted from (Westbrook, 2002).

To summarize: by combining these three components an MRI system is able to align, encode, tip, and detect the spins of nuclei in the field of view based on their 3D position and the tissue composition of the voxel. These concepts only scratch the surface of the physics behind MRI but are sufficient to understanding the challenges that lay ahead when designing a dual modality PET/MRI system.

1.3.2 Benefits

PET/CT already exists in clinical settings and has for some time, so what is the benefit of PET/MR? PET/CT offers fast, spatially co-registered scans and the ability to measure attenuation levels in tissues (introduced in section 1.1.1) in order to provide anatomical landmarks for the functional information provided by PET (Cherry et al., 2006). Unfortunately, CT contributes a substantial amount of radiation dose in addition to the amount patients are already receiving from PET. For example, a typical FDG-PET deposited ~7-14 mSv per scan depending upon the injected dose, whereas CT increased that amount by ~2-4 mSv per low dose scan and by ~14-19 mSv for full diagnostic scans according to a dosimetry study by Brix et al. in 2005. Since MRI does not use ionizing radiation while still providing the anatomical landmarks and offering additional versatility in functional imaging it is a very complimentary modality to PET that is an attractive alternative to CT.

In addition to lacking ionizing radiation MRI has the potential to enable simultaneous acquisition between the two systems provided their FOVs can be matched, as opposed to the sequential scans used in PET/CT. PET/CT is unable to achieve this currently due to the interference of the γ-rays from both systems with one another. This time correlation opens up exciting possibilities in dynamic functional studies using PET with magnetic resonance spectroscopy, chemical shift imaging, functional brain MRI, and MRI perfusion capabilities. This capability could result in simultaneous study of: anatomy, perfusion, glucose consumption, oxygenation, cell labeling, neurotransmitters, receptor density, tissue pH, metabolite concentration and metabolism, many including correlated data from both modalities; a feat which is currently unattainable (Wehrl et al., 2009).

MRI is also known to have superior soft tissue contrast compared to CT, proving advantageous over CT in the original motivation for PET/CT (von Schulthess, 2009). Though it may seem like a perfect fit, combining MR and PET is not without its difficulties and shortcomings.

1.3.3 Challenges

From a clinical perspective PET/MRI is missing the ability to quickly perform attenuation correction for PET images. MRI only gives information about tissue proton properties, and in fact in MRI scans bone and air appear with similar intensity despite having opposite photon attenuation properties (von Schulthess, 2009). Though this may be compensated by computational algorithms or specific pulse sequences the timing of the CT attenuation scan will be difficult to match.

From an engineering perspective an integrated, simultaneous PET/MR scanner design has to face the challenge of mutual interference between the two systems. The magnetic susceptibility, χ, of a material is the extent to which a material becomes magnetized in a field, and differences in χ cause magnetic gradient effects around materials. This is one of the sources of contrast in MR images, but can also be a source of artefacts and signal drop-out in MR images (McRobbie et al., 2002). The various components of the PET system will affect the homogeneity of B_0, which will cause a change in the Larmor frequencies and subsequent affects on the MR signal. In particular the scintillators have relatively large values of χ: common scintillators (NaI, CsI, BGO, LSO) vary from -30 to 10 $\times10^{-6}$, and gadolinium containing scintillators (LGSO, GSO) 790+ $\times10^{-6}$, while human tissues are around -11 to -7 $\times10^{-6}$ at common clinical magnet strengths (Yamamoto, 2003). Shielding is used to protect circuitry from RF interference and is usually made of copper or aluminum, which themselves have χ of -5.46 and +16.5 $\times10^{-6}$ (Lide, 2000), also outside the range of human tissues. For this reason the PET components must be kept distant from the field of view of the magnet, which can be challenging in the case of a PET ring insert.

Changing magnetic fields will induce currents, known as eddy currents, in conductors such as those present in the PET detector electronics. By Lenz's law, the eddy currents produced in PET components will create an opposing magnetic field that will attenuate the gradient field for a short time, thus interfering with spatial positioning in the MRI system (Olcott et al., 2009a). Any conductors, including shielding, must then be made as transparent as possible to the gradients, and designed in such a way as to reduce eddy currents (i.e. higher resistance). If the PET ring is a full ring, continuous conductors in this ring shape will act as shielding to the FOV inside, and as such the RF transmitter is unable to transmit through the PET ring (Olcott et al., 2009a). Additionally, PET signals on any wires may cause electric fields which couple to the RF receiver causing additional interference. If any of these factors cause magnetic field disruptions close in proximity to the FOV or RF coils of the MRI system, they will cause interference in what is already a delicate system.

The MRI system not only suffers interference, but causes its own with respect to the PET system. Due to these factors the PET ring will need to be located outside of the RF coils. In this physical region the gradient coils operate and cause large temperature increases (>10^{o}C) which can affect the operation of the PET detectors (Ziegler and Delso, 2013). Though PMTs are not as sensitive to temperature as solid state devices, they are very sensitive to magnetic fields and their use is impractical; the extent of this interference is shown in figure 1.15 (Pichler et al., 2008). Due to the size of the PMT this was a likely result regardless, as the size restrictions within the bore of the MRI are problematic. For example, a PET insert in a typical 60cm MRI bore will degrade its own maximum FOV by two times the length of its detectors, and PMTs are typically several cm in length.

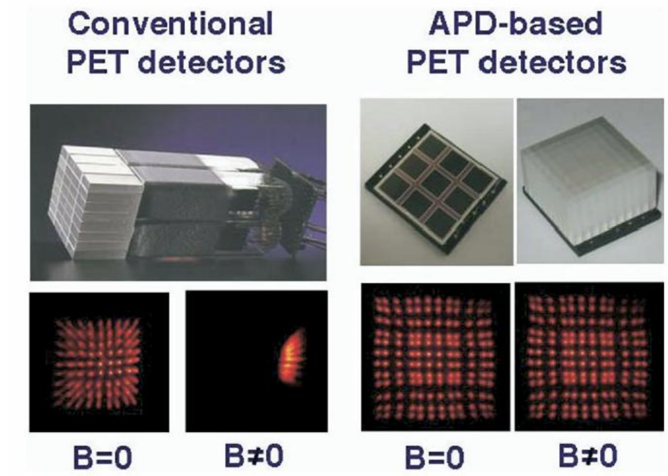

Figure 1.15 The effects of magnetic fields on PMTs and APDs. The PMT signal is distorted by a horseshoe magnet placed near the detector, while the APD functions in a 7T magnetic field. Image from Pichler et al., (2008).

The gradient and RF coils also interfere with signals on PET circuit board traces and wires. Though the gradient coil frequencies are such that they are usually filtered out by PET electronics, the RF frequencies are in the 50-400MHz range which coincides with scintillation pulse frequency components. This requires the PET components to be shielded by an appropriate amount of a conductor with low susceptibility, such as copper or aluminum, which in turn interferes with the MRI as noted previously. Regardless of these challenges, PET/MR technology has forged ahead; these developments will be discussed in the next section.

1.3.4 Recent Developments

Research groups have been quick to address the issue of attenuation correction in PET/MR. Hoffman et al. (2009) produced a study that investigated many methods of MR attenuation correction (MR-AC) from several different groups. The study found differences between MR-AC and standard PET point or rod source or CT-AC for two methods. For torso AC, coregistration and morphing of MRI into CT-like torso images was performed to transform MR images to match CT-AC scans, the best result was ~3.2% average difference and ~10% maximum to conventional CT-AC. For brain AC, brain MR images were segmented and attenuation coefficients assigned to the regions to form the AC map and compared to standard PET-AC; best results in this case were similarly a maximum of ~10% error. More recently, Bezrukov et al. (2013) performed an updated study examining three methods. The first two, continuous atlas-based and segmentation-based approaches were included in the previous study, and the third method examines PET emission data with respect to anatomical MRI scans to compute the AC. The updated study is extensive, encompassing 100s of scans, and notes that it is difficult to compare results from different methods and groups. Still, their data shows a minimum average error of 0.6±3.4%, 0.9±0.9% and ~10% for the methods, respectively. These results are promising and even with these errors clinical PET/MR has become a reality.

As mentioned previously, Pichler et al., (2006) have investigated the effectiveness of APDs in magnetic fields up to 7T, and Spanoudaki et al. (2007) and España et al. (2010) confirmed the suspicion that SiPMs were also unaffected. In light of this result, and because of the potential advantages of SSPMs for conventional PET, many groups have been working with APDs and SiPMs in recent years: Dokhale et al. (2009), Schaart et al. (2010), Peng et al. (2011), Thompson et al. (2011) , and Yang et al. (2011), to name just a few. There have also been studies investigating simultaneous PET/MR.

Kolb et al., (2012) investigated a clinical brain PET/MR system by Siemens healthcare. The system uses LSO coupled to APDs with energy resolution of 17.1±0.7% and timing resolution of 4.9ns, and the group found a small effect on SNR of the MRI, though this did not significantly affect imaging capabilities. Also in 2012, Yoon et al., investigated a SiPM based PET/MR system they designed. They found the PET performance unaffected by the MRI system and reported energy resolution of 13.9% and timing resolution of 1.23ns; they did find a 14% reduction in MRI SNR, but they were also using LGSO crystals, known for poor MRI compatibility.

The most recent development has come in the form of digital SiPMs, devices that incorporate much of the front end electronics of a PET system right into the SiPM using CMOS technology; outputs are digitized immediately (Degenhardt et al., 2009). Frach et al., (2009) performed an initial study of the device capabilities and found energy and timing resolutions of 10.7% and 153ps, respectively, with a 4x4x22mm and 3x3x5mm LYSO crystal, respectively. Radoslaw et al., performed a more recent study in 2012 that found 14.5±1.3% average energy and 376ps average timing resolutions using a larger array of 2x2x22mm LYSO crystals. Devices with performance such as these are an exciting development for PET and PET/MR alike.

1.4 Motivation and Organization

The purpose of the projects presented in this thesis is to develop an MR compatible PET detector block that has acceptable performance, a small profile, and low cost requirement. The end goal of the project is to design brain, and eventually full body, PET/MR insert rings for use in research by our group. Given the recent developments discussed in this paper, the SiPM seemed like a natural choice for this project. The challenges associated with such an undertaking have been discussed, and considerations made to assess those challenges.

Firstly, the small profile of the detector is important. The goal was to design a detector block that is ~5cm in length using 20mm long LSO crystals. Since the SiPM device contains 16 channels, analog signal multiplexing is used to reduce the amount of front end electronics and cabling that are required to be placed within the MRI. In order to determine which of the many potential multiplexing schemes to use, a study was performed comparing two candidates using electronics designed in house. Second, to improve the MR compatibility of the device copper cabling into the bore was undesirable. In this design, vertical cavity surface emitting lasers (VCSELs) are employed to transmit the signal from the block detector over MR compatible fiber optics.

In chapter 2 a discussion of the methodology and equipment used in these projects is presented. There has been significant work performed in the design of the analog electronics and digital signal processing scripts which will be presented in this chapter. The materials and components used in our experiments are discussed and circuit diagrams provided. Any significant departures from the materials and methods presented here will be discussed in the corresponding chapter.

Chapter 3 describes the first of the two projects, a comparison of multiplexing schemes for PET block detectors. Analog signal multiplexing is a useful tool to reduce the number of output channels in a system but comes at the cost of detector performance. In order to characterize the effect on detector performance, two multiplexing schemes were investigated and compared to each other and a detector without multiplexing. Relevant background, simulated and experimental results, discussion and the conclusion of this work are presented in this chapter.

Chapter 4 introduces the second project: the development of an electro-optical coupling system for MR compatible PET block detectors. This chapter further discusses the challenges of integrating PET and MRI by presenting recent work in this area and provides the motivations for this work. This section will describe the electro-optical system design and experimental results and provide a discussion and conclusions.

Finally, Chapter 5 summarizes the conclusions of the previous chapters and discusses future directions for these projects.

Chapter 2

Materials and Methodology

This section will describe the materials and methods that are used in the experiments in the following sections with discussion about the choices surrounding them where applicable. Any significant differences between either of the experiments and any general procedures introduced here will be noted in their respective sections.

2.1 Materials

2.1.1 Scintillation Detector

The scintillation detector includes the scintillation crystal, scintillation light detector and any light diffuser or accompanying apparatus. As mentioned in chapter 1, PET systems favour faster scintillators such as LSO, LYSO, and LaBr3, with scintillation decay times on the order of ~40-47ns, ~41ns, and ~35ns respectively (Lima 2011). Table 2.1 shows the properties of many common scintillators for comparison and indicates desirable properties for these experiments. It is evident from the table that the two best candidates for this work are LSO and LYSO. Though BGO is within the desired emission wavelength it is very slow, and although $LaBr_3$ is an excellent candidate its emission wavelength is too low and it suffers from problems with its hygroscopicity. For the experiments performed in this paper, LYSO crystals of various sizes, arrays and surface treatments were used. For certain timing experiments, a 3x3x20mm^3 LYSO crystal with polished surfaces and specular reflectors was used; for other experiments including energy resolution and positioning, two arrays of polished, diffuse reflector crystals were used: a 2x2 array of 3x3x20mm^3 LYSO crystals (~3.1mm pitch) and a 6x6 array of 2x2x20mm^3 LYSO crystals (~2.1mm pitch), all of which can be seen in figure 2.1a through c. Finally, for all coincidence experiments a Teflon wrapped 4x4x4mm^3 LYSO crystal was coupled to the reference detector.

Table 2.1: Properties of typical scintillation materials. Elements after a semicolon indicate dopant; some properties can change depending on the dopant concentration. LYSO properties vary based on Yttrium/Lutetium fraction. Compiled using data from (Knoll, 2000; Cherry, 2006; Lima, 2011).

Scintillator	Density (g/cm^3)	Light Yield (photons/keV)	Decay Constant (ns)	Emission Peak (nm)	Refractive Index	Photoelectric Fraction (%)
NaI:Tl	3.67	41	230	410	1.85	17
CsI:Na	4.51	40	630	420	1.84	21
BGO ($Bi_4Ge_3O_{12}$)	7.13	9	300	480	2.15	40
LSO (Lu_2SiO_5:Ce)	7.4	26	40-47	420	1.82	32
LYSO ($LuYSiO_5$:Ce)	6-7.1	26	41	420	1.81	21-32
$LaBr_3$:Ce	5.3	61	35	358	1.9	13
Ideal	High	High	Low	470-590	-	High

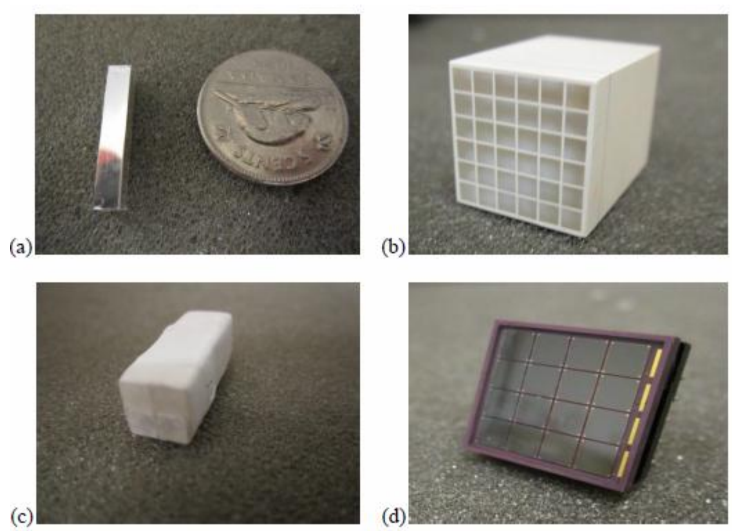

Figure 2.1 (a) A 3x3x20 mm3 LYSO crystal with specular reflectors. (b) The 6x6 array of 2x2x20 mm3 LYSO crystals with Teflon wrappings with pitch of 2.1 mm. (c) The 2x2 array of 2x2x20 mm3 LYSO crystals with Teflon wrappings with pitch of 3.0 mm. (d) The 4x4 SiPM array from SensL (pixel size: ~3 mm)

The surface treatment of the crystals is not the focus of this research but is an important consideration. Heinrichs et al., (2002) performed an extensive study that examined the effects of surface roughness treatments and reflective coatings on the energy resolution and light output of LSO crystals. More recently, Auffray et al., in 2011 examined the reflector's effects on timing resolution experimentally, and Yang et al., (2013) examined both properties' effects in simulation and experimentally with respect to timing, energy and light output characteristics. The findings of these papers indicate that a high reflectance wrapping will result in higher light output and improved energy resolution, and polished crystal surfaces are superior to untreated ones. Additionally, Yang et al., (2013) found that specular (mirror-like) reflectors yield slightly improved timing characteristics. Following from this research, experiments in this paper make use of Teflon and specular reflectors and polished crystals.

The reason that emission wavelength is important is due to the scintillation detector. As this work is done with the goal of a PET insert for a PET/MR system in mind, a SSPM was required. For these experiments, the SiPM based SensL ArraySL-4 was chosen and can be seen in figure 2.1d. Table 2.2 shows some of the device specifications, while figure 2.2 shows some operating properties of the device. Note that in figure 2.2a, the peak PDE (>12%) occurs in the 470-590nm region, and that at wavelengths around 385 (emission peak of $LaBr_3$) the detection efficiency is ~1%. This is a limiting factor in scintillator choice for this device and is what led to the use of LYSO. Figure 2.2 also indicates a dependency of pixel gain upon bias voltage; 2V over breakdown is required to achieve the listed gain and is the standard operating voltage. Due to heating from the device, temperature monitoring, bias control and cooling are necessary in schemes with poor air circulation and tightly packed designs due to the temperature dependence of the gain in SiPMs. The important qualities and operating principles of SiPMs have been discussed in section 1.2.

Table 2.2: Properties of the ArraySL-4. (SensL, 2011)

Property	Value	Property	Value
Pixel Chip Area	3.16x3.16mm^2	Microcells per Pixel	4774
Pixel Active Area	3.05x3.05mm^2	Array Layout	4x4
Operating Voltage (typ.)	29.5V	Total Active Area	13.4x13.4mm^2
Microcell Recovery Time	131ns	Pixel Pitch	3.36mm^2
Pixel Gain (@V_{op})	2.4x10^6		

Finally, the scintillation crystal and SiPM may make use of a light diffuser for experiments with a greater than one to one crystal pixel to detector pixel ratio. A light diffuser facilitates the spreading of light from many crystal pixels onto fewer detector pixels in order to split light between them in a way that is proportional. In detectors with smaller ratios of crystal pixels to detector pixels a diffuser is not always necessary, but in setups with a higher ratio (larger than 2:1, without position sensitive detectors) many crystals may be entirely situated above the same detector pixel and be indiscernible without light multiplexing. Figure 2.3 illustrates light multiplexing in a scintillation detector. The proportional signal can be decoded to determine the position of the crystal where scintillation occurred. Potential loss of scintillation photons can occur in the dead space between detector pixels, by transmission through the reflectors of the light diffuser, and reflection at the crystal/diffuser interface. Another concern when using diffusers is edge compression, where pixels near the edge of the array blend together because of reflections at the side of the diffuser affecting the uniformity of the light spreading (Peng et al., 2011). In this paper, a 1mm thick, uniform, glass diffuser is used in some experiments.

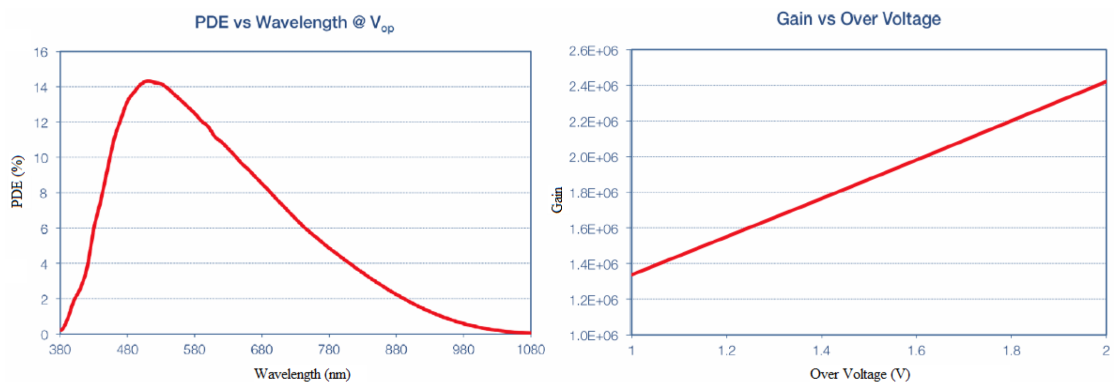

Figure 2.2 Properties of the SensL ArraySL-4. Left: Wavelength dependant response of the detector. The maximum PDE occurs at ~500nm. Right: Linear dependence of detector pixel gain on the applied over voltage. Reproduced from SensL (2011).

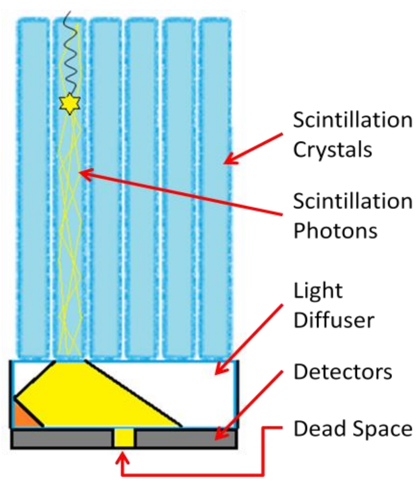

Figure 2.3 Light Multiplexing in a scintillation detector. Photons emitted isotropically from the absorbed γ-ray are reflected until they exit the bottom face. Refraction and diffusion within the light diffuser spreads out the photon beam exiting the crystal splitting the scintillation signal across many detectors (and their dead space).

2.1.2 PET Electronics

This section will describe the electronic elements of the detection system used in these experiments. Figure 2.4 shows a block diagram of the general PET detector signal chain that is used, from scintillation detector to digitization. As the detector has already been discussed, this section will focus on the preamplifiers, shaping/filter, summation and fast trigger, and the analog-to-digital converter (ADC); the multiplexing stage will be discussed in more detail in chapter 3. Due to the availability of standard nuclear instrumentation modules (NIMs), analog signal processing was performed using custom built electronics.

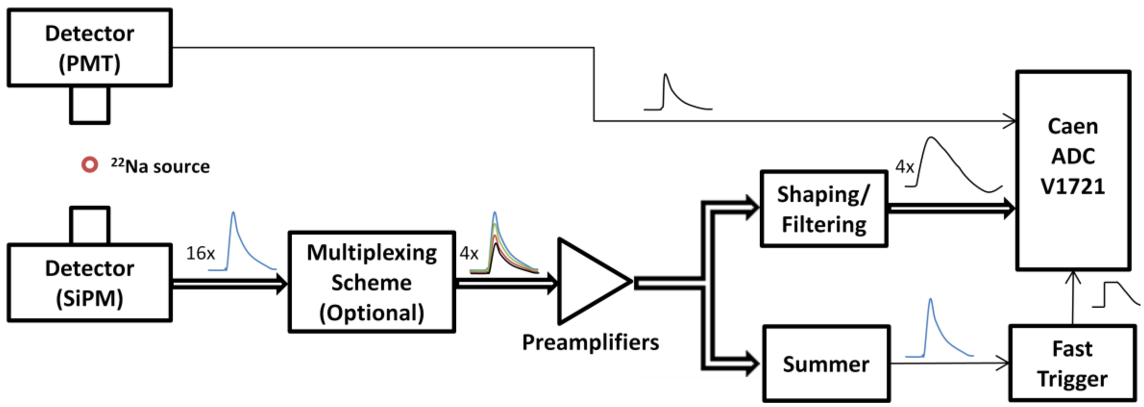

Figure 2.4 Block diagram of electrical signal chain for PET detector.

It is important to first mention the capabilities of the ADC, since many of the design decisions are based on these parameters. The ADC used in these experiments is the Caen V1721, an 8-bit free running ADC with sampling period of 2ns (equivalent to 500MS/s) and input voltage range of 1V. The resolution of the ADC, or least significant bit, is 1/256V or ~3.9mV. Typically, NIMs are used as inputs to the ADC and their outputs can be easily controlled to match its capabilities. As that is not the case here, each stage of the signal chain must be designed with this ADC in mind.

The first stage of the signal chain is the preamplifier. The purpose of the preamplifier is to increase the amplitude of detector signals to a measurable level. Often, the PET detector signals are very small and very fast, on the μA and several nanosecond scales, which can be difficult to digitize and measure (Ahmed, 2007). These signals contain information about the charge produced in the scintillation detector which is proportional to the energy deposited in the scintillator and thus accurate measurement of these signals is important for determining the energy of the incoming γ-ray. For this first stage of the signal chain the Analog Devices AD8001 was used in a low impedance front end amplifier configuration as shown in figure 2.5 (Säckinger, 2005). The AD8001 is a high speed, current feedback amplifier with an input capacitance of 1.5pF and a gain-bandwidth of 800 MHz. This particular type of amplifier was used instead of the more common charge sensitive preamplifier because the light output of the LYSO crystals combined with the large gain of the SiPM produced signals that are large enough to make use of the full range of the ADC input by a transimpedance of as little as 50Ω, as used here. This design is specifically chosen for its high bandwidth and easily controlled input impedance which will become important in some experiments. The bandwidth of a low impedance front end amplifier, taking in to account the input capacitance and capacitance of the detector pixel, is given by equation 2.1, while the output of the amplifier is given by 2.2:

$$BW = \frac{1}{2\pi R_{in}(C_a + C_d)} \tag{2.1}$$

$$V_{out} = (R_{in} \times I_d)(1 + R_f / R_g) \tag{2.2}$$

where BW is the 3-db bandwidth of the amplifier, R_{in} is the transimpedance resistor, C_a is the capacitance of the amplifier and C_d is the capacitance of the detector which are assumed to be in parallel; the other parameters can be found in figure 2.5. This assumption may not apply when certain analog charge multiplexing designs are included. Without the significant effect of the detector capacitance this front end has a bandwidth of just over 2.1 GHz. The typical output of a single detector pixel, before and after the op-amp in the preamplifier, can be seen in figure 2.6 and shows the rise time of the signal pulse to be ~40ns before and ~50ns after this stage. Reducing the resistance, and thus increasing the bandwidth, of the front end did not affect the signal rise time indicating that only the bandwidth of the op-amp was limiting at the time of this figure. This effect could be alleviated by reducing the gain of the non-inverting amplifier at the cost of the signal dynamic range, and was adjusted as necessary based on the detector setup. All circuit boards used in these experiments were designed for 4 signal chains, and 1 summed signal which will be referred to as channels A through D and 'sum,' as the multiplexing stage is often included to reduce the 16 SiPM outputs to 4.

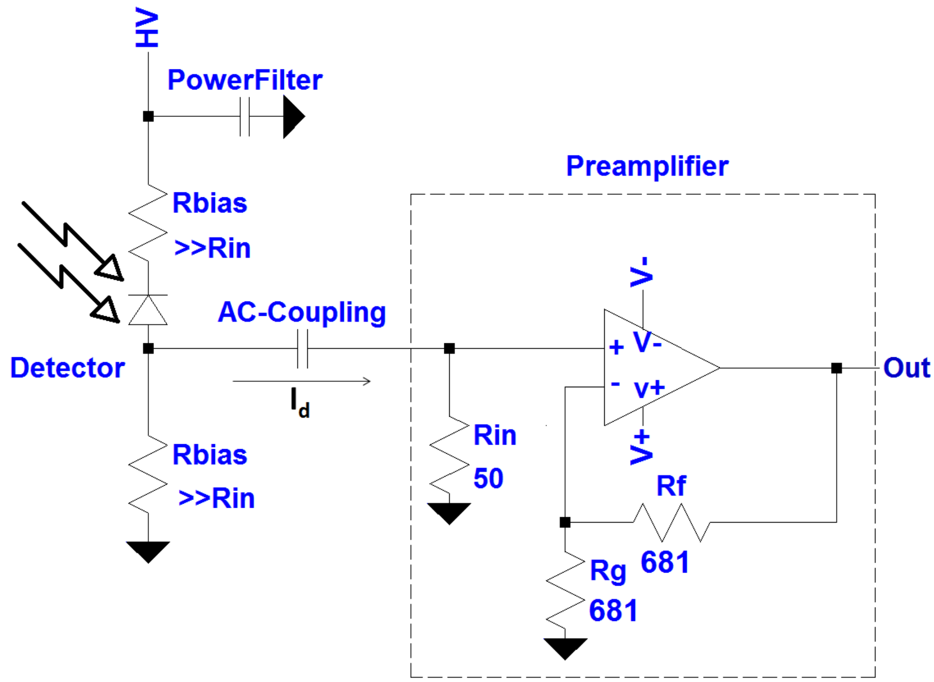

Figure 2.5 Circuit diagram consisting of the detector biasing and preamplifier. The low-impedance front end is formed by the resistor R_{in} and op-amp. The resistor, R_{bias}, is included to properly bias the detector with respect to ground prior to the AC coupling capacitor. R_{bias} must be much larger than R_{in} to divert the detector current, I_d, to the preamplifier.

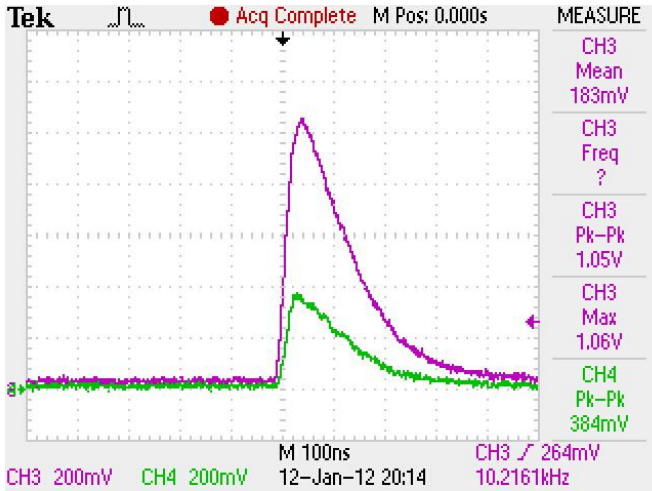

Figure 2.6 Oscilloscope trace from the output pin of the preamplifier. CH4, green, is the detector signal at the non-inverting input of the op-amp. CH3, pink, is the output of the preamplifier op-amp. Note that this signal is measured with the oscilloscope probe, and thus the electronic noise of the device is amplified 10x. One 3x3x20mm^3 LYSO crystal coupled to one SiPM pixel with no electrical multiplexing was used to produce this data.

The next stage in the design is the shaping amplifier (also known as pulse shaping). The use of the pulse shaper arose from the need to measure the amplitude of very narrow-peaked, but very long preamplifier signals that were too fast for digital conversion to accurately measure, and which would cause pile-up (Knoll, 2000). Pile-up results from two or more detector signals in close temporal proximity interfering with subsequent pulses which ride upon the tail of the preceding pulses, causing a change in pulse shape and height which can confound measurements. The purpose of pulse shaping is then to round the peak and shorten the signal tail to facilitate this measurement and avoid pile-up as shown in figure 2.7a. Typical pulse shaping is performed using a differentiator-integrator pair called CR-RC shaping (an example is given in figure 2.7b); when using higher order integrators the practice is referred to as Gaussian shaping due to the resulting signal shape. These two components of the shaping system are also known as high and low-pass filters, respectively, and there exists many circuit topologies using active components that can be advantageous over their passive implementations; adding gain above unity, higher filter quality, and improved SNR (Ahmed, 2007). A common issue arising from the use of pulse shaping is baseline wandering. Because a capacitor cannot conduct direct current, the average DC voltage of an isolated node following it must be equal to zero (Knoll, 2000). As a result, the baseline of the signal shifts to equate the integrated area of the pulse above and below 0V DC; this shift will affect the amplitude of the signal. The shift is proportional to the distance between signal pulses and is thus more relevant to applications expecting high count rates. Shapers that produce bipolar pulses can alleviate this problem.

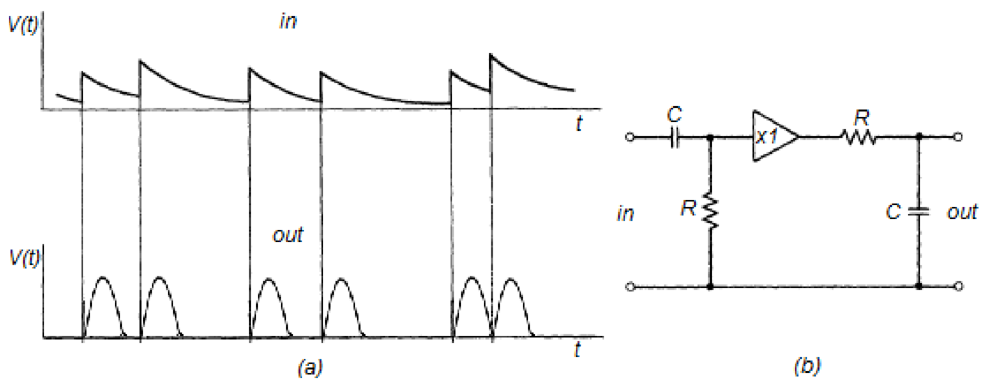

Figure 2.7 The effect of pulse shaping on long preamplifier signals to avoid pile-up. (a) Pile-up is evident in the top graph, changing the peak amplitude of each pulse. In the lower graph all peaks are the same, after pulse shaping performed by the circuit in (b). Figure adapted from Knoll (2000).

Because of the speed of the ADC, the shape of the preamplifier output is easily measured and due to its short duration of ~500ns pile-up is not a significant issue with counts per second in the low kHz. Thus, pulse shaping is primarily used to filter noise and improve SNR. Filtering is performed using a band pass filter comprised of a 2nd order high pass filter and 2nd order low pass filter, both using the Sallen-Key topology and Butterworth coefficients (Mancini, 2003). The circuit diagram for this stage of the signal processing chain can be seen in figure 2.8. The time constants (or corner frequencies) of the filters are usually significantly smaller than the decay constant of the preamplifier. However, in the preamplifier configuration used here, the decay constant of the signal pulse is roughly equivalent to the decay of the scintillation photon signal which is already quite small. The transfer function of the low-pass stage of this filter design is described by equation 2.3 (Mancini, 2003):

$$H(s) = \frac{A_0}{1+\omega_c[C_1(R_1+R_2)+(1-A_0)R_1C_2]s+\omega_c{}^2R_1R_2C_1C_2s^2}, \quad A_0 = 1+\frac{R_3}{R_4} \qquad (2.3)$$

where s is the Laplace variable (complex angular frequency), R and C correspond to the resistors and capacitors of figure 2.8, A_0 is the gain of the filter stage, and ω_c is the cut-off frequency of the filter. The equation is presented in this way since the coefficients of s and s^2 are often used as design variables known as a_i an b_i, respectively, where i is the stage number for multi-stage, higher order filters. Certain values of these design variables yield particular properties of the frequency response of the filter; specific sets of values have been developed to aid in filter design such as Butterworth (flat pass-band) or Tschebyscheff (steep roll-off). The transfer function of the high pass stage is similar, with the denominator of equation 2.3 divided by b_is^2. The overall frequency response of this filter can be seen in figure 2.9, and indicates the cut off frequencies and gain of the circuit. Thus, the corner frequencies are chosen as 1MHz and 20MHz for the high and low pass filters, respectively, corresponding to the fall and rise times of the preamplifier signal. In a filter there is an inverse relationship between the Q-values (a measure of the quality of the filter) and the damping factor ζ (which describes system oscillations) which is dependent upon the component values. In this work a Q-value of ~0.5 is obtained resulting in an approximately critically damped filter to avoid excessive oscillations in the pass-band while maintaining a -40dB/decade roll-off, at some cost in the sharpness of the inflection at the corner frequencies. There are some limitations on the components that can be used; if capacitances are too small, parasitic capacitance of the op-amp will become large in comparison and thus sets a lower limit on these values; if resistances are too high, leakage current from the op-amp will cause significant noise and offset in the signal, requiring more filtering or causing saturation.

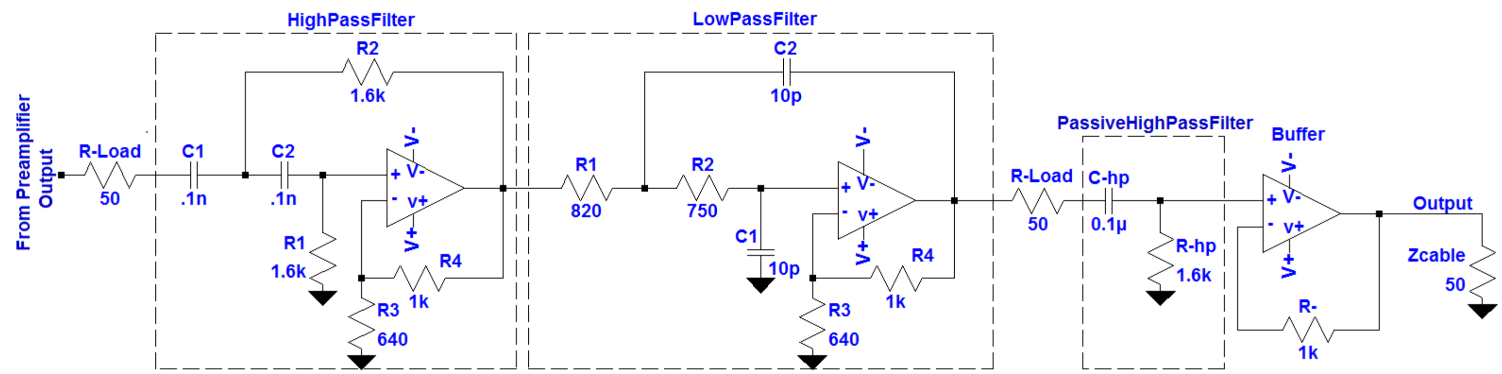

Figure 2.8 Circuit diagram of pulse shaping stage. Since the AD8001 is not suited to drive capacitive loads, a small resistance R_{load} is introduced before capacitors. For feedback stability in the op-amp, a 1kΩ resistor, $R_{\_}$, is kept in the feedback loop of unity gain buffers.

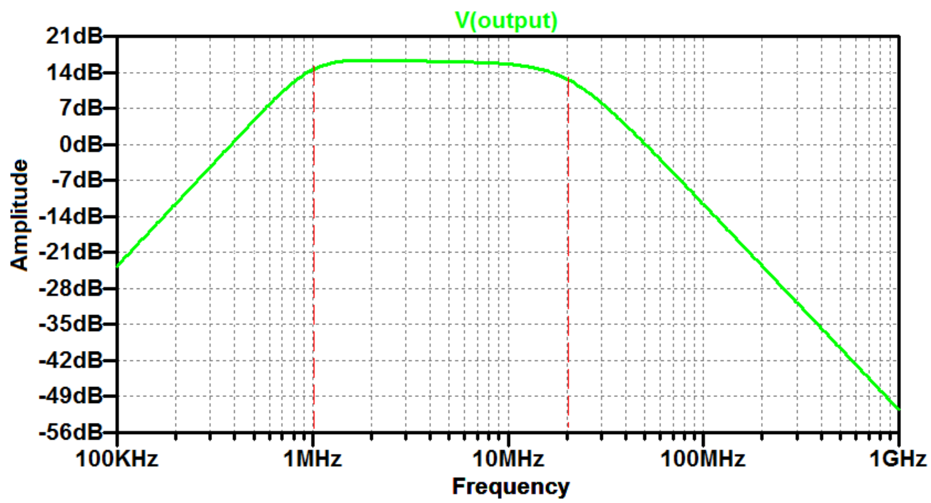

Figure 2.9 Frequency response of the circuit in figure 2.8, produced in LTSpice (Linear Technologies, 2012). The corner frequencies are indicated by the red dotted line.

Following the low pass filter is a passive high pass filter and voltage follower. This is included as a baseline restoration technique which was included for cases where higher count rates would be expected such as larger crystal arrays or more active sources. The output of the filtering stage can be seen in figure 2.10 which clearly shows the bipolar pulse shape. This output is fed directly into the ADC for digital pulse processing. The rise time of the output signal is seen to be ~100ns, indicating that parasitic capacitances did have some effect on the real corner frequencies in the filter (by decreasing it), as mentioned previously. The four outputs from this stage are used for energy and position measurements, while the next stage is primarily focused on timing.

The summer and fast trigger are implemented to improve timing measurements and act as a trigger for the ADC in experiments using two detectors in coincidence. Directly after amplification in the preamp, the channel is split into the filter stage and a voltage follower. The voltage follower decouples the filter stage input from the input of the inverting summer circuit that follows. All 4 channels are summed, and an additional inverter is included with greater than unity gain, resulting in a net positive gain on the sum of the 4 preamplifier signals. This summed signal is used as a trigger for the ADC since its amplitude is consistent regardless of the position of detected events (i.e. in the

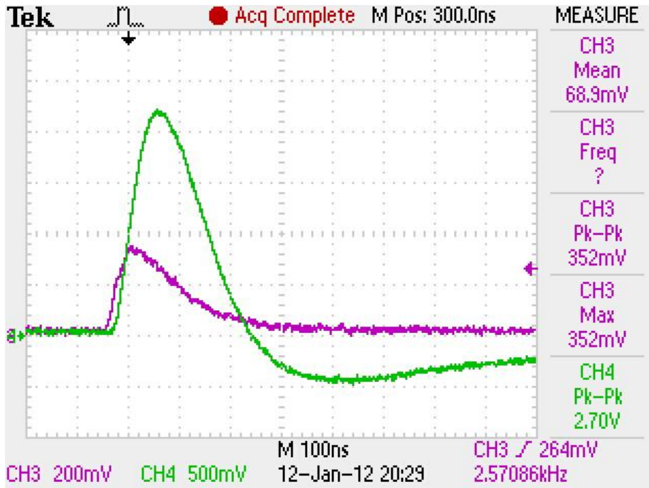

Figure 2.10 Output of one channel of the signal processing chain. CH4, green, is the output of the buffer from figure 2.8. CH3, pink, is the detector signal at the non-inverting input of the op-amp. Note that this signal is measured with the oscilloscope probe, and thus the electronic noise of the device is amplified 10x. As in figure 2.6, this is the output from one LYSO crystal coupled directly to one SiPM pixel. Since the bipolar shape makes the peak to peak value misleading, note that the maximum value of CH4 is 2.22V.

multiplexed case). In addition, due to the amplification of the summed signal, its rising edge has a large slope compared to the individual channels which correlates with improved timing performance, as mentioned in section 1.1.2 and equation 1.13. As such, this signal is recorded and used in digital time resolution processing. Because the 4 filter channels are also available, they can be used for energy measurements while the summed channel can be amplified to the point of saturating the op-amps in order to provide a very large rising slope to improve timing, without affecting energy measurements (Lau et al., 2010). However, in this case an energy window would need to be applied digitally as the energy information within the summed signal is lost. The circuit diagram of this stage can be seen in figure 2.11.

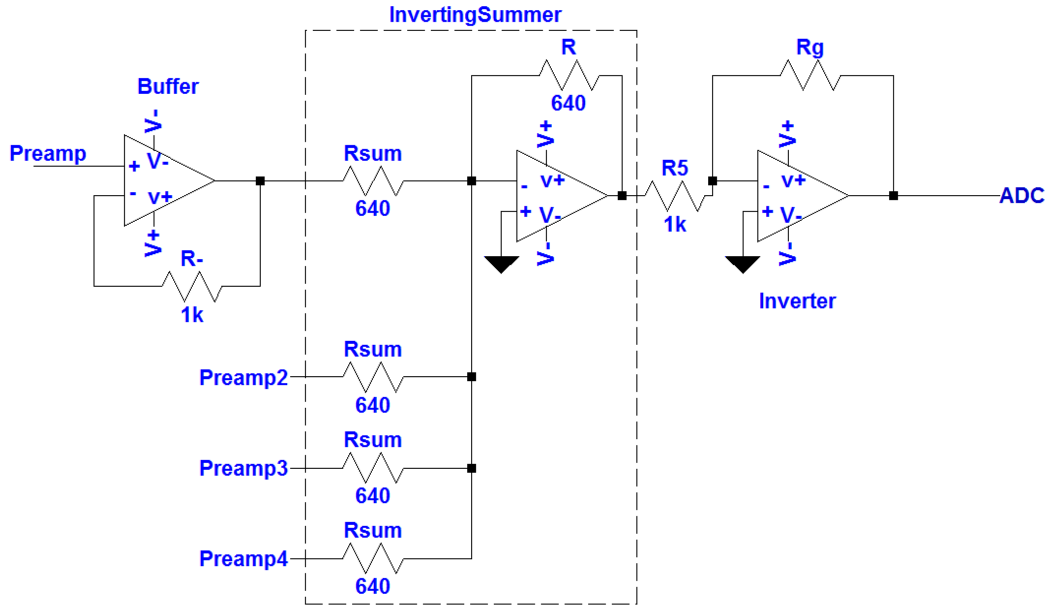

Figure 2.11 Circuit diagram of summer and trigger stage. The resistor R_g controls the gain of the inverter. For feedback stability in the op-amp, a 1kΩ resistor, $R\_$, is kept in the feedback loop of unity gain buffers. Note that a buffer is present for all 4 preamplifier input channels, but only shown for the first.

2.2 Methodology

2.2.1 Experimental Setup

All of the experiments in this work were performed inside of a custom built light tight enclosure. As seen in figure 2.12, the detectors are aligned along a track which facilitates coincidence detection experiments. A PMT holder is also present, and is adjustable in vertical position to facilitate better alignment or DOI measurements. In this work a fast PMT (R10560, Hamamatsu Photonics K.K) is used in coincidence timing resolution measurements as the 'gold standard' reference detector. This device is coupled to a 4x4x4 mm3 LYSO crystal, wrapped in Teflon tape. All crystals are coupled to their respective detectors using BC-630 optical grease from Saint-Gobain Ceramics & Plastics, Inc, which has a refractive index of 1.465. This coupling is performed to reduce the amount of refraction and reflection that would occur at the crystal-air interface.

In this work, 511keV γ-rays are emitted from a sealed ^{22}Na source with an activity of 3.7MBq. Other sealed sources were used for calibration of the detector equipment; ^{137}Cs for 662keV γ-rays, and ^{57}Co for 122keV γ-rays.

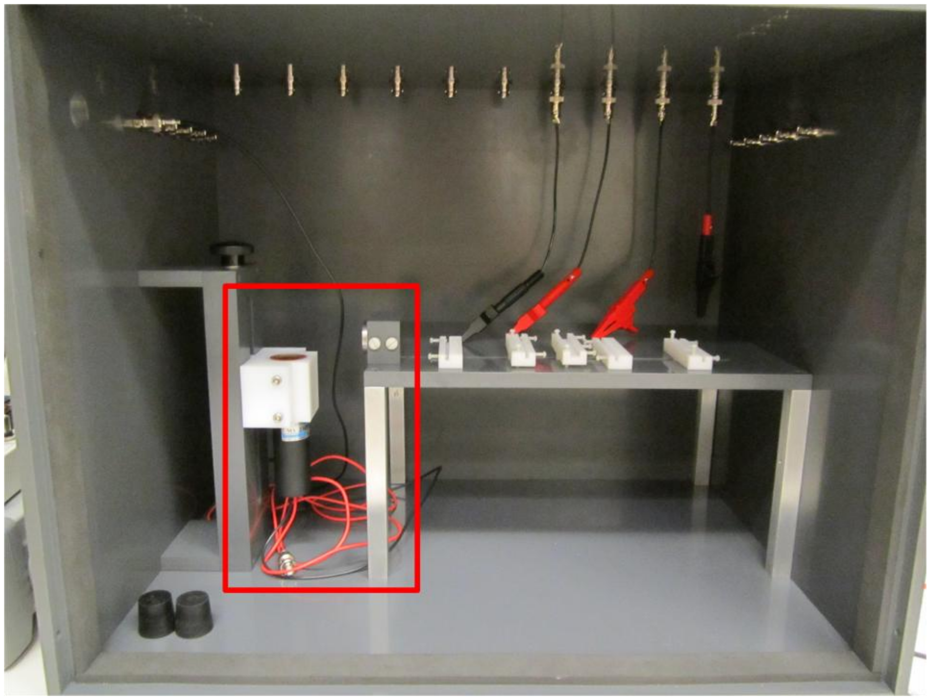

Figure 2.12 Light tight enclosure for scintillation detector experiments. BNC connectors are used to transmit signal and power across the box. The white stages are made of Delrin and aligned along the track in the platform, as is the PMT holder. Collimator and adjustable PMT holder (red box) are optional for experiments; the collimator is not used in this work.

2.2.2 Digital Signal Processing

In order to facilitate digital signal processing, all data from the experiments is acquired in what is known as 'list-mode.' In this method, all of the raw event signals are stored in chronological order. From these raw signals the energy (and where applicable, timing) information is determined and stored in order, such that the final output is a large array of event data numbered chronologically and indicating the energy level and difference in arrival times between the SiPM detector and reference PMT. During this process events that do not fall within the desired energy or timing windows can be ignored. The ADC records 256 data points (equivalent to 512ns) from each channel simultaneously whenever any of the channels designated as a trigger pass a threshold. In the case of coincidence experiments, the ADC will only trigger when all channels in the same trigger group pass their threshold within the same 512ns recording window. Data is not necessarily acquired using timing window discrimination, such as in experiments where the 1.27MeV photopeak of ^{22}Na is visible and the energy spectra was all that was desired. Table 2.3 helps illustrate list-mode data storage in this experiment:

Table 2.3: An example of list-mode acquisition for *n* events. Raw data is stored in a separate Array for each channel.

Event ID	Energy A	Energy B	Energy C	Energy D	PMT Energy	Coincidence Time
1	A_1	B_1	C_1	D_1	PMT_1	$Time_1$
2	A_2	B_2	C_2	D_2	PMT_2	$Time_2$
⋮	⋮	⋮	⋮	⋮	⋮	⋮
n	A_n	B_n	C_n	D_n	PMT_n	$Time_n$

To obtain the energy information of each incoming photon, a triangular shaping method was applied to each SiPM detector signal channel, A through D, as well as the summed timing channel, and PMT signals (if applicable) after digitization (Peng *et al* 2007). This method is similar to the aforementioned analog pulse shaping and is expected to provide good SNR performance and to help remove possible pile-up and baseline wandering. Essentially, it calculates the difference between the summation of two regions of length *L* separated by a gap *G*, as shown in formula 2.4:

$$\mathrm{L} \cdot V_k = -\sum_{i=k-2L-G}^{k-L-G} V_i + \sum_{i=k-L+1}^{k} V_i \qquad (2.4)$$

Equation 2.4 gives the shaped value of *V* at data point *k* where *k* is the set of points from (2*L*+*G*) to the total number of data points in the signal. This method was designed primarily with field programmable gate arrays (FPGAs) as the intended signal processor, since these kinds of operations are well suited for those devices. The effect of this method can be seen more clearly in figure 2.13. Energy information is derived from the value of the absolute peak of this shaped signal, from each signal channel, and stored in memory corresponding to that event ID. A histogram is formed using this data: for each channel individually, or, more commonly, for the sum of channels A-D when multiplexing was included. The photopeak of the histogram is fitted to a Gaussian curve with both linear and constant components described by equation 2.5:

$$y(x) = ae^{\left(\frac{(x-b)^2}{d^2}\right)} + lx + c,\ d = \sqrt{2}\sigma \qquad (2.5)$$

where a is the amplitude of the fitted Gaussian, b is its centroid, and d is related to the standard deviation by the relationship shown. l and c are included to account for the low energy tail on the left hand side of the 511 keV photopeak due to scatter events and the self-illumination of the LYSO crystal, and allows for their removal before assigning the Gaussian fit in order to improve the fitting and characterization of the energy resolution. The energy resolution is determined according to equation 1.8.

Typically, energy spectra are presented with energy values on the x-axis. However, in this work the bins of the histogram correspond to the measured peak value from the previous discussion as calibration revealed a quite linear detector response. Conversion from bin number to energy values would have yielded only a slight improvement in energy resolution and was deemed unnecessary. To calibrate potential non-linear detector response and nonzero-offset of the ADC, three energy peaks (511 keV from the ^{22}Nasource, 662 keV from a ^{137}Cs source, 122 keV from a ^{57}Co source) were tested and the result can be seen in figure 2.14.

The coincidence timing resolution is determined by forming a histogram of the differences in arrival times between the SiPM detector and the reference detector. To determine the differences in arrival time between the two detectors a constant fraction discrimination (CFD) method is used. The CFD is a method that aims to alleviate the time walk issue introduced in section 1.1.2 and figure 1.9. It does this by altering the input signal such that the zero crossing of the output is independent of the slope of the rising edge in an ideal case. In reality, noise will still interfere with the measurement, but time walk is greatly alleviated. Equation 2.6 describes the CFD method:

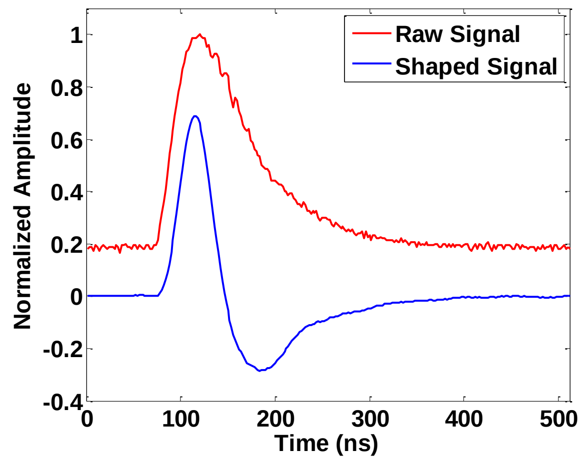

Figure 2.13 Triangular shaping algorithm performed on the summed signal channel. Note that the baseline has returned to approximately 0 and that noise has been reduced.

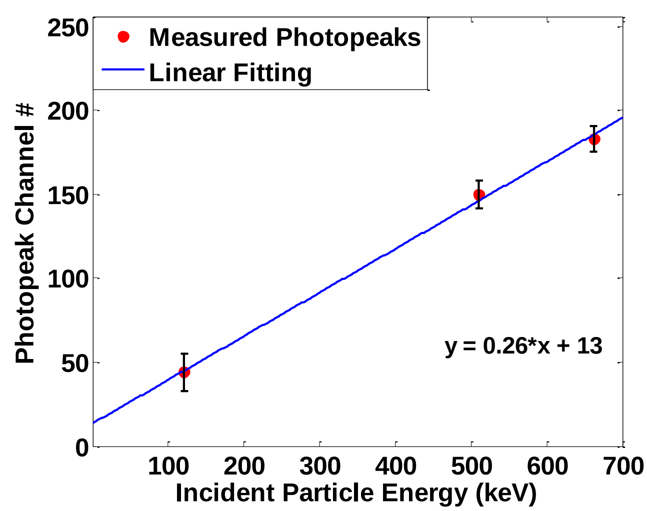

Figure 2.14 Calibration of the SiPM detector for a single 3x3x20mm^3 LYSO crystal. Error bars represent the FWHM of the photopeak for the 511 keV incident γ-rays from the ^{22}Nasource, 662 keV from a ^{137}Cs source, and 122 keV from a ^{57}Co source. Linear fitting is applied to the measured photopeaks without the error bars.

$$V_{CFD} = \sum_{i=1}^{L} (f \times V_i - V_{i-d}) \tag{2.6}$$

where i is the index of the digital signal, f is the attenuation factor, d is the delay applied to the inverted signal, L is the length of the signal and V_{CFD} is the output of the CFD. Since the signal is discrete, the zero crossing is determined by linear interpolation of the two points of V_{CFD} straddling the zero axis. Figure 2.15 illustrates the CFD method. This process is performed for both the summed SiPM signal and PMT signal and the difference in the two zero crossing indices is compared. The histogram of these differences is fitted by a Gaussian without any linear or constant components, and the FWHM is recorded as the time resolution.

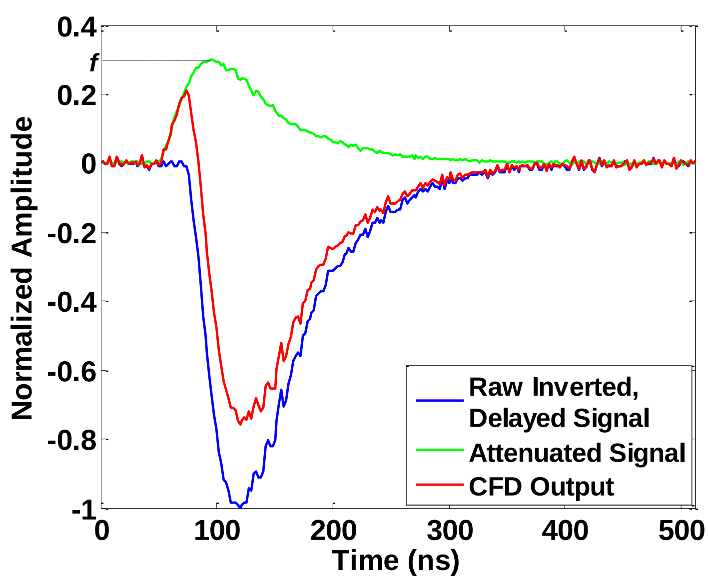

Figure 2.15 Application of the CFD to the summed signal channel. The attenuation factor, 0.3, is indicated by *f*. The delay on the inverted signal was 20ns. These values can be optimized for the input

The previously discussed signal processing is performed for the event data of a single scintillation crystal, yet most detectors will feature pixelated arrays of crystals. In the case where each crystal is coupled directly to a single detector whose output is fed directly into signal processing, identifying which crystal the event belonged to is as easy as identifying the channel number. However, as is discussed in chapter 3, there is sometimes a need to reduce the total number of channels by using multiplexing which necessitates some method of decoding the position at which the annihilation event occurred inside the crystal array. An investigation of the method of decoding is left for chapter 3, but the important result is the flood histogram (or flood map). This is a histogram of all of the positions recorded by the decoding method arranged in 2 dimensions, usually normalized to [-1, 1] in both directions. In the ideal flood histogram, each peak identifies a crystal in the array whose spatial position is used in forming a line of response for image reconstruction. Thus, crystal identification is an important part of signal processing; the flood map must be segmented into crystal regions and event data attributed to those regions.

In this work, the flood map is formed as a 2-D matrix of cells, each cell representing one location bin in the histogram and containing a 2-D array of the list mode data for all events localized to that bin. The intensity of the bin is then defined as the length of the list mode data in that cell. Initially, the data has not been subjected to energy gating; only the energy values recorded, raw data catalogued and with no timing information. This is because of slight variations in gain and detection efficiency that occur within the detector, causing each crystal to have a different photopeak position in the energy spectra. The gain for each crystal must be calibrated to be approximately equal, which requires a first pass to determine the magnitude of the calibration. Once known, the gain correction can be applied to events in that crystal and the sum of all crystal energy spectra is formed; this global energy spectrum can then used for energy gating of subsequently processed data.

After the flood histogram is produced it is segmented using Voronoi tessellation in MATLAB (MathWorks, Inc.) (Peng *et al* 2011). Figure 2.16 illustrates the Voronoi tessellation method, including seeding points and Delaunay triangulation. Seeding points are found by determining local maxima in the histogram intensity. Edge contours are closed by adding 4 seed points well outside of the histogram area before performing the segmentation, and deleting their Voronoi cells afterwards; otherwise some edge contours are described by points at infinity.

Once segmented, the cells within each segment are combined to form a single list of all data for that crystal. From this data, the energy spectrum is formed and photopeak position and resolution determined. The raw data for each event is processed by the CFD and the timing data organized into a histogram with timing resolution recorded. Next, the average photopeak is determined and the energy data in the list for each crystal are multiplied by a factor to stretch the photopeak of its energy spectra to that position, simulating a change in gain. Finally, the global energy spectrum is formed from the sum of all calibrated spectra. The edges of the 511keV photopeak of this spectrum can be used to reject scattered photon events; processing the data again with this energy gating can improve the flood histogram.

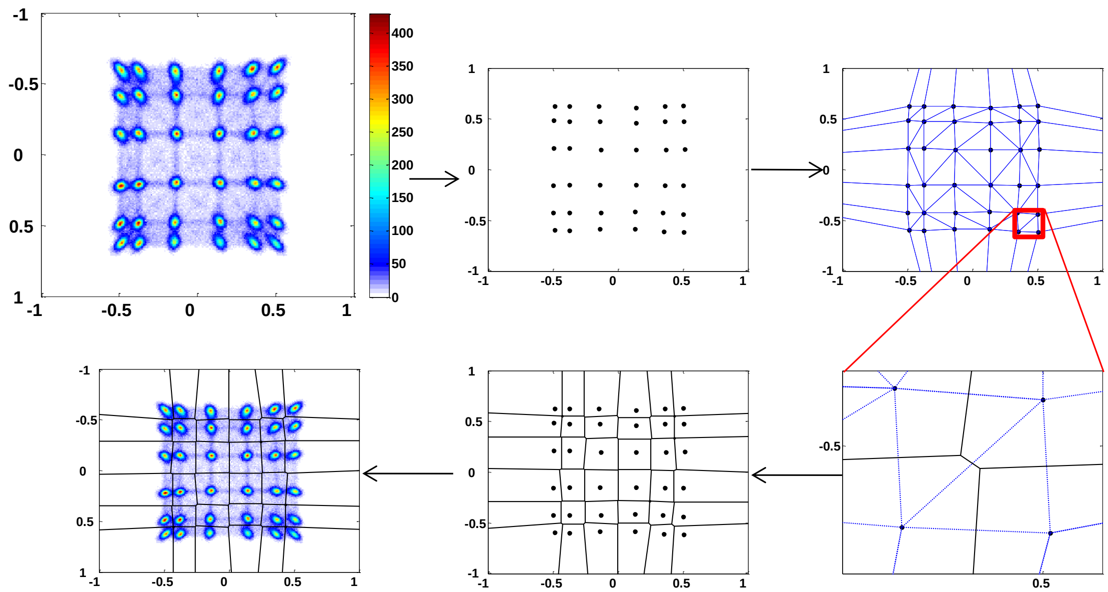

Figure 2.16 The crystal segmentation method using Voronoi tessellation. Clockwise from top left: Initial flood histogram is formed. Local peaks are used as seeds for Delaunay triangulation. Delaunay triangulation produces the triangulation of the points. Perpendicular bisection of the edges of the triangles meets at the center of the circumcircle of the triangles. These lines are the contours of the cells formed by Voronoi tessellation.

Chapter 3

Investigation of Two Analog Electrical Multiplexing Schemes for PET Detectors

3.1 Introduction

Recently, solid-state photomultipliers have been the subject of investigation for PET detector design as a replacement for PMTs as mentioned in section 1.3.4. In particular, silicon photomultipliers (SiPMs) are comparable in performance to PMTs in terms of multiplication gain and photon detection efficiency, while being more compact, immune to magnetic fields, having fast temporal response, and operating at lower bias voltages. While avalanche photodiodes (APDs) and position-sensitive variations (PSAPDs) are also being widely used for PET detector design (Olcott et al., 2005a, Catana et al., 2006, Lau et al., 2010, Yang et al., 2011), their performances are mainly limited by two factors: lower gain (~100-1000) when compared to SiPMs with gain on the order of ~10^6, and inferior temporal response due to the large parasitic capacitance across the p-n junction of their larger area, among other comparisons discussed in section 1.2. Superiority to APDs and the advantages over PMTs make SiPMs a very attractive replacement for PMTs in PET/MRI systems.

Two advantages of SiPMs stand out with regards to developing PET/MRI hybrid systems: compactness and insensitivity to magnetic fields. The first advantage will enable use of smaller crystal elements and achieve higher spatial resolution due to reduced detector pixel sizes. Both advantages will allow for the detector to be brought right into the limited available space in the bore of an MR scanner and perform simultaneous PET/MR imaging without comprising the performances of each modality. The challenges of integrating PET components in an MRI bore have been discussed in section 1.3.3. Of particular interest for this work, to design a single PET/MRI insert ring of 50 cm diameter, around 100 of the ArraySL-4 SiPM detectors are required and thus 1600 output channels as well as associated front-end electronics. To address this challenge, multiplexing schemes are explored as a method to reduce the number of readout channels and thus the complexity, cost, and physical space of the system.

There are generally two categories of multiplexing in PET detector development: light multiplexing (also known as light sharing) and charge multiplexing. In the former, when the pitch of the crystals is smaller than the size of photodetectors, a light diffuser is introduced to provide light sharing among a number of photodetectors which is unique for each crystal and can be used to determine spatial information using a positioning algorithm (i.e. Anger logic) (Peng et al., 2011). However, this multiplexing does come with some trade-offs. For instance, some light photons will be lost during the transmission through the optical interfaces (i.e., crystal/diffuser/photodetector), as well as in the dead-space between detector units, as described in section 2.1.1 and figure 2.3.

Charge multiplexing schemes include two implementations: resistive and capacitive. Previously, one group investigated the resistive multiplexing schemes for signals of a PMT (Seigal et al., 1996). The work aimed to reduce the 64 outputs of a multi-channel PMT system to just 4 using a variety of resistor networks. The resistive scheme has also been adapted by many groups in recent years (Herrero-Bosch et al., 2008, Song et al., 2010, Thompson et al., 2011, Janececk et al., 2012). In essence, the current signal from a detector unit is injected into a network of resistors and split among outputs based on the impedance between that node and each output channel. The current splitting and position encoding depend on a number of parameters, such as resistor values, input impedance of amplifiers, and the parasitic capacitance of detectors. A slightly different version has also been applied to PSAPDS (Lau et al., 2010), in which the charge was split through a resistive sheet on the anode side instead of discrete resistors. Four electrodes at the four corners of the sheet were used to read out signals and determine the spatial/energy information. To minimize the effect of this resistive sheet on timing performance, the cathode signal without any resistive multiplexing was used to extract timing information.

More recently, capacitive multiplexing has been proposed for the SiPM-based PET detector development (Olcott et al., 2009b), in which detector signals were read out for each row and column individually. This concept had been originally designed as a cross-strip readout method for germanium detectors (Gerber et al., 1977). In essence, the scheme uses capacitor pairs of different capacitance values to divide charge. The capacitive scheme mainly differs from the resistive network in that each row and column of a detector unit are tied together to determine positions rather than distributing charge across a network. In addition, it is expected to introduce less degradation on timing performance as the resistance in the circuit is kept to a minimum, compared to the resistive multiplexing.

In spite of the benefit of reducing the number of readout channels, it should be noted uncorrelated noise from other detector units would be added for both resistive and capacitive multiplexing, dissimilar to the case of one-to-one coupling without multiplexing. This might consequently degrade energy resolution, time resolution, and positioning. Also, the light multiplexing and charge multiplexing can be used at the same time to achieve the highest degree of reduction of readout channels. In that case, the detector's performance might be affected in a more complicated way, compared to that of either light multiplexing or charge multiplexing alone.

Research has found that no published studies have focused on a direct comparison between the two multiplexing schemes described above for novel SiPM-based PET detectors, which is the main focus of this work. In this chapter, two charge multiplexing schemes are investigated and a comprehensive comparison with respect to energy resolution, time resolution, and spatial information (flood histogram) is provided. This chapter consists of two parts. In the first part, both schemes are examined using a circuit simulation tool to gain insight into their operation and determine optimum values for circuit components. In the second part, both schemes are implemented in circuitry and their performance measured for two crystal array configurations (crystal pitch: 3.1 mm and 2.1 mm, from section 2.1.1) coupled to the SiPM. For the 2.1 mm crystal array, both light multiplexing (using a light diffuser of 1.0 mm height) and charge multiplexing were present. Possible causes for the different performances between the two multiplexing schemes, as well as several potential challenges in the implementation will be discussed.

3.2 Methods

3.2.1 Multiplexing Schemes

The two schemes that have been investigated are based on previous work (Siegal et al., 1996, Olcott et al., 2009b), as shown in figure 3.1. The resistive multiplexing scheme is shown in figure 3.1a. The charge produced at each pixel is split between the four output channels through the resistor network. The positioning information for each incident 511 keV high energy photon is encoded by the relative magnitudes of the charge distributed to each channel. This encoding is controlled by the values of the resistors in the network. For the second and third rows, no resistor (R_0) was put at the ends of the resistor chain as in the first and fourth rows. The reason for this is to minimize the negative effect on timing characteristics due to the effect of larger resistances in the RC circuits formed within the multiplexing scheme and spatial non-linearity. The position is encoded by Anger logic according to equation 3.1:

$$X = \frac{B+D-(A+C)}{A+B+C+D} \quad Y = \frac{A+B-(C+D)}{A+B+C+D} \qquad (3.1)$$

The capacitive multiplexing scheme is shown in figure 3.1b. The current/charge signal produced at the anodes and cathodes of 16 pixels is grouped along rows and columns, separately. For each row or column, the current signal is consequently divided by a pair of capacitors (C_a and C_b) at the end of each 'strip' that encode the position based on their relative values of capacitance. The total capacitance for each strip (C_a+C_b) is equal and thus the total output current is expected to be constant for all pixels. Also note that for these two-terminal devices, the voltage signals measured from the anode and cathode sides are of the same amplitude but opposite polarity, and could be used as differential signals. A critical trade-off here is that the values of capacitors (C_a and C_b)

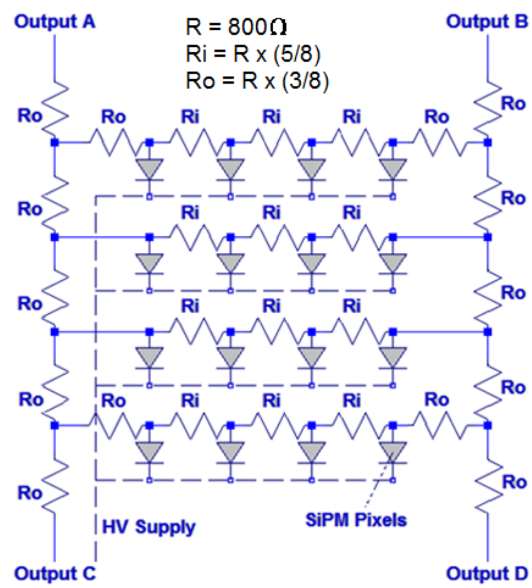

(a)

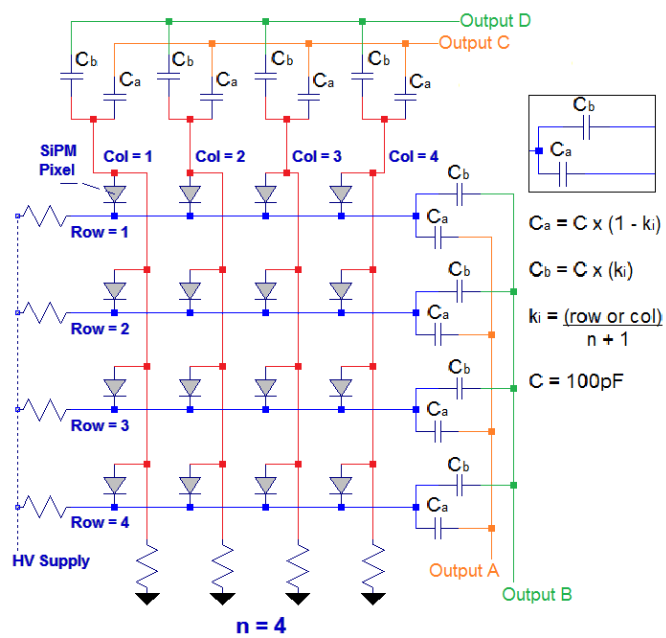

(b)

Figure 3.1 Circuit representations of the two multiplexing schemes used in this experiment. (a) shows the resistor network including the values of the resistors used at different nodes in the scheme. (b) shows the capacitor network including the values of the encoding capacitors at the end of each column and row. Each layout acts as a charge multiplexer, dividing the charge produced at each SiPM pixel among the 4 outputs. Note that each scheme has reflective symmetry between each quadrant of 4 pixels. Each 4x4 array of pixels can be referenced by row or column number starting at the top left corner at (1,1) and ending at the bottom right at (4,4).

must be chosen carefully with respect to the parasitic and package capacitances of the individual SiPM pixels (not shown in figure 3.1b). For instance, a smaller capacitance would result in higher impedance and thus less charge transferred to the output node; while larger capacitance would result in more charge transferred to the output node but degrade temporal response due to a larger RC time constant. The position is encoded by equation 3.2:

$$X = \frac{C-D}{C+D} \quad Y = \frac{A-B}{A+B} \tag{3.2}$$

The unlabeled resistors in figure 3.1b act to limit current passing through the SiPM and properly bias the pixels with respect to ground. In the resistor scheme in figure 3.1a, just before the preamplifier as shown in figure 2.5, an AC coupling stage was implemented that included a 1μF capacitor and bias resistor. The values of these components did not have any measurable impact on the signal of the multiplexing scheme in simulation or experiments. The distinction is made in the diagram in figure 3.1b since the capacitors in that scheme accomplish the AC coupling, and thus a ground path must be made available to the anode prior to the preamplifier stage. The impedance of the resistors should be large compared to C_a and C_b in order to avoid splitting too much of the signal to ground.

The component values were picked with the help of the simulation and optimized, partly through trial and error. Optimizing the values is difficult as they will affect everything from signal amplitude, timing, dynamic range (maximum and minimum signal height), and flood map positioning and shape. These effects will be discussed in greater detail in section 3.4. The relative values for the resistors were picked after examining the relationship between R_o and R_i and the dynamic range, shown in figure 3.2, and trying to maximize the range in both x and y directions. The relative capacitor values are chosen to be a linear progression, resulting in 4 evenly differentiated current dividers, resulting in a linearly distributed flood map. The absolute values were chosen after considering these aforementioned effects and trying to find a compromise that allowed reasonable comparison between the schemes (i.e. to avoid making one scheme sacrifice timing and energy resolution for flood map performance).

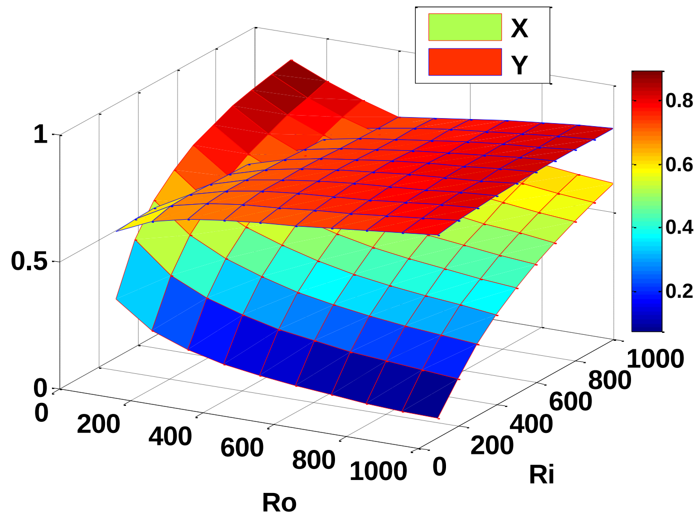

Figure 3.2 Dynamic range in the positive X and Y directions VS the relative values of the multiplexing resistors. In order to achieve a square shape the ratio of *Ro* to *Ri* was chosen to be near the intersection of the two planes, thus maximizing the dynamic range for both directions. The actual values depend on many design decisions.

3.2.2 Simulation Study

The goal of this simulation was to examine the output signals after multiplexing (i.e., amplitude and rising edge), and the quality of flood histogram using the positioning logic. In order to do this, a train of pulses representing the signal from scintillation photons generated by a 511 keV high energy photon, were generated in LTSpice (Linear Technology, 2012). The characteristic signal resulting from scintillation of a LYSO crystal was simulated using formula 3.3 (McCallum et al., 2002).

$$I = C(e^{\frac{-t}{\tau_R}} - e^{\frac{-t}{\tau_F}}) \tag{3.3}$$

where I is the detector current signal, and τ_R and τ_F are the rise and falling time constants of LYSO scintillation, respectively using values of 3 ns and 42 ns. C is based on the charge produced in each pixel, which is found from formula 3.4:

$$C = \frac{Q}{\tau_f - \tau_R}, \quad Q = e \times PDE \times N \times G \qquad (3.4)$$

where Q is the charge produced by the detector, e is the electron charge, PDE is the overall detector photon detection efficiency, N is the number of photons produced in the scintillation event, and G is the gain of the scintillation detector.

These pulses were then added to a noise signal modeled as Gaussian white noise with standard deviation depending on the desired SNR. The SNR values were chosen based on the measured SNR of an existing detection system (32.2 dB) and decreased from that point in order to simulate the noise produced in the generation of photons and charge carriers (Poisson, shot noise), passive or active circuit elements (Johnson-Nyquist, thermal noise), and effects of light multiplexing. 800 of these pulses were used as piecewise linear signals originating from the equivalent circuit of the detector which was modeled in LTSpice. These detector circuits were used in the multiplexing circuit spice models as indicated in figure 3.1, including the 50Ω input resistance of the preamplifier. After the simulation in LTSpice, the output waveform file at each of the four outputs was exported to a tab-delimited text file that was read as a raw signal data file in Matlab and subsequently processed as a real signal would be as described by section 2.2.2.

The equivalent circuit of the SiPM pixel was investigated by Seifert et al. in 2009. In this simulation, however, it has been simplified to be a current source in parallel with a capacitor to model the total parasitic capacitance. This change is made since the internal resistance had no significant effect on multiplexing or simulation results due to its comparatively large value, the lack of an externally triggered switch for the simulation, and the simulation complexity of simulating several thousand microcells. The value of the parasitic capacitance was selected to be 50 pF per pixel, based on the previous work

(Seifert et al., 2009). In the capacitive multiplexing case, the bias resistors were made to be 10 kΩ. An output load resistance of 50 Ω was used for each circuit.

3.2.3 Experimental Setup

There are few details of the setup for these experiments that was not discussed in section 2.2.1. First, due to the amplitude of signals from a single 3x3x20mm^3 LYSO crystal coupled to the SiPM without multiplexing, the bias of the SiPM was reduced slightly to 29.0V in that case in order to keep the preamplifier consistent between experiments. The standard operating voltage for these devices was 30.3V for all other experiments. As the gain of these devices depends on temperature, a thermistor was placed directly beneath the detector in some experiments to monitor temperature. And, lastly, in experiments involving the 6x6 array of LYSO crystals data was acquired only in coincidence with the PMT in order to reduce the signal processing time, acquisition time, and data storage. Because of this, the 1.27MeV photopeak, LYSO self illumination and a significant portion of noise events are absent from the energy spectra for those crystals. Figure 3.3 shows the final set up of the detectors within the light tight enclosure.

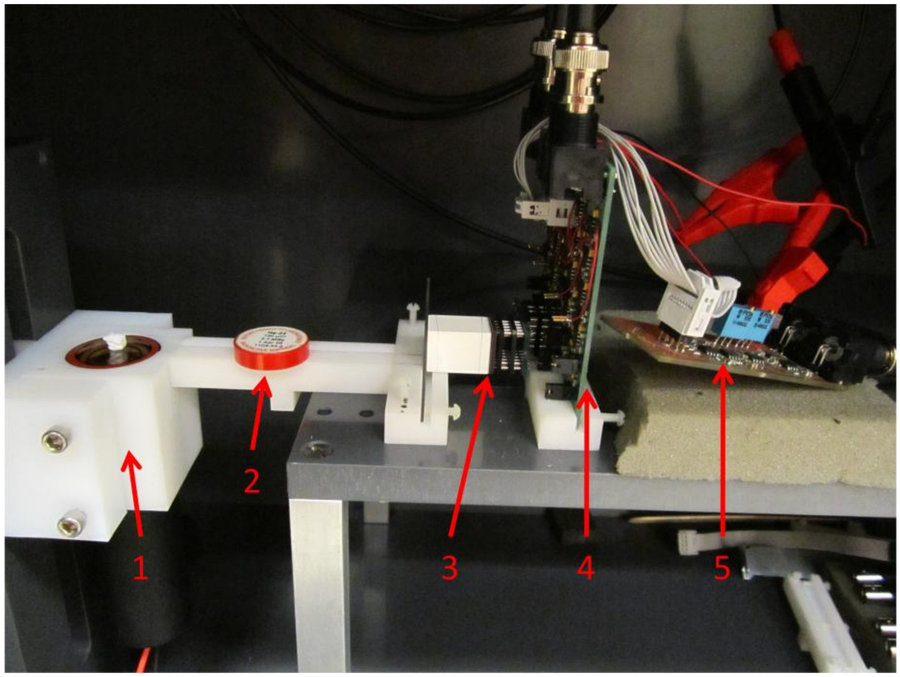

Figure 3.3 Typical experimental setup for multiplexing design experiments. (1) Reference PMT detector and 4x4x4mm^3 LYSO crystal. (2) ^{22}Na source, centered between detectors. (3) SiPM detector and scintillator. The SiPM is mounted on an interchangeable circuit board, which can be replaced with either multiplexing scheme. (4) Circuit board containing much of the signal processing chain. (5) Trigger circuit board containing the summing circuit.

3.2.4 Figures of Merit (FoMs)

For the simulation, the chosen FoMs are the rising slopes of signals and the quality of the flood map as a function of the signal SNR. The 10%-to-90% rising slopes of the output signals are good indicators of timing performance as time resolution is limited by the ratio of noise to the slope of the rising edge of the signal as shown in equation 1.13. For the flood map, the dynamic range is defined as the difference between the maxima and minima of the range of position values taken in the central region, in both x and y directions.

In the experiments, the chosen FoMs are energy resolution, time resolution, and the quality of the flood map. For energy resolution and time resolution, the results of individual crystals (best, worst and average) are reported. For the flood map, we compared both the dynamic range and peak-to-valley ratio (PVR). The dynamic range is defined similar to that in the simulation study, and where only one quadrant is available it is extrapolated to the symmetric case to keep the values comparable between crystal arrays. The PVR reflects the overlapping in the flood map between two adjacent crystals, which is associated with the noise characteristics of each multiplexing scheme (Peng et al., 2011). In this work, the PVR value for each peak in the one-dimensional profile was analyzed by calculating its peak value divided by the local minimum value on either side, in both x and y directions. Then the average PVR value was obtained for multiple peaks.

3.3 Results

3.3.1 Simulation Results

The simulation results are shown in figures 3.4 and 3.5. In LTSpice simulation, for a given input, four output signals are obtained for each event (table 3.1). The flood histograms (also called flood map) after the position decoding are shown in figure 3.4, for two selected SNR values (3 and 30). It is evident that at the component values chosen, the capacitive multiplexing scheme has superior dynamic range, 1.55 to the 1.05 of resistive multiplexing, but appears to be more susceptible to noise (i.e. broader distribution for each pixel). A clear dependency of the crystal separation in the flood map on SNR is observed, as previously reported (Peng et al., 2011). This reflects a fundamental challenge for implementing multiplexing schemes for PET block detector as noise from adjacent pixels will be introduced and thus degrade SNR.

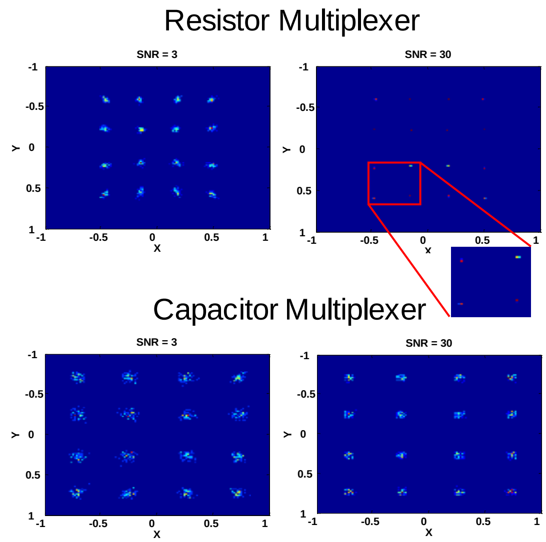

Figure 3.4 Resulting flood histograms for SPICE simulation of two proposed multiplexing schemes. The flood map is created by using 800 pulses generated in Matlab at a specified signal-to-noise ratio as inputs to the simulated circuit in SPICE. Noise is generated as Gaussian white noise; all pulses are identical prior to applying this noise. Inset: zoom of one quadrant of the resistor multiplexer at SNR = 30 flood map, this ratio resulted in single pixel distributions which are difficult to see on the full map.

The output signals of four channels after multiplexing can be seen in figure 3.5. The rising edge slope for each channel and the sum of four channels is provided in table 3.1, for both resistive and capacitive multiplexing schemes. The rising slopes of individual channels vary with position in both schemes, and were determined from a noiseless case in order to focus on the effect of the position. It is observed that the capacitive multiplexer has larger slope values in every case and there is less fluctuation observed in the summed signal among pixels, which is 9.00, 8.96 and 8.95 mV/ns for the three pixels selected. For the resistor multiplexer, the values are 2.24, 1.04 and 1.06, respectively. As expected, as the total impedance to the output nodes increases as we traverse the resistor multiplexer from the edge towards center pixels, the rising slopes significantly decrease indicating that edge pixels are able to achieve better timing performance. For all cases, the sum of the four output signals has the largest slope and was chosen as the trigger for coincidence measurements in the following sections.

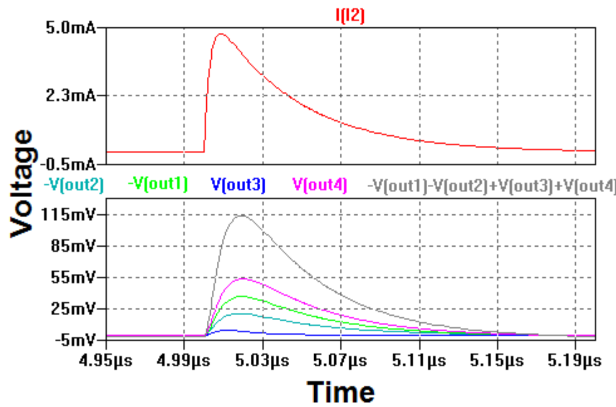

Figure 3.5 LTSpice simulation results. Top: Input current signal at location (1,2) from figure 3.1. Bottom: 4 output signals (and sum) of the capacitor multiplexing scheme used to determine rising slope values, without noise for illustrative purposes. Signals 'Vout1' to 'Vout4' correspond to outputs C, D, B, A from

Table 3.1**:** 10-90% Rising edge slopes for multiplexing scheme outputs generated by simulation at specified detector pixels. Pixel labels correspond to the description in figure 3.1.

Pixel\Channel	Sum (mV/ns)	A (mV/ns)	B (mV/ns)	C (mV/ns)	D (mV/ns)
		Resistor Multiplexer			
(1,1)	2.24	2.47	0.17	0.14	0.05
(1,2)	1.04	0.76	0.33	0.07	0.05
(2,2)	1.06	0.57	0.24	0.25	0.14
		Capacitor Multiplexer			
(1,1)	9.00	3.98	0.55	3.98	0.55
(1,2)	8.96	3.97	0.55	2.78	1.67
(2,2)	8.95	2.79	1.67	2.78	1.67

3.3.2 Experimental Results: Energy Performance and Flood Map

Single Crystal without Multiplexing

The energy spectrum of a single SiPM pixel coupled to a 3x3x20 mm^3 LYSO crystal without multiplexing is shown in figure 3.6. Under this setting, signals of 1.27 MeV high energy photons (also from Na-22 source) saturated the system even with the reduced bias voltage and were discarded. For the 511 keV photopeak, the detector demonstrates an energy resolution of 12.3±0.2% FWHM. This measurement was then repeated with the two multiplexing schemes and the energy resolution results were found to be 12.9±0.2%

and 14.8±0.3% for the resistive and capacitive schemes, respectively. When a comparison between the multiplexing and non-multiplexing cases is made, it should be pointed out that the change in bias will slightly affect energy and timing performance compared to the 29.0 V case due to increased gain of the SiPM.

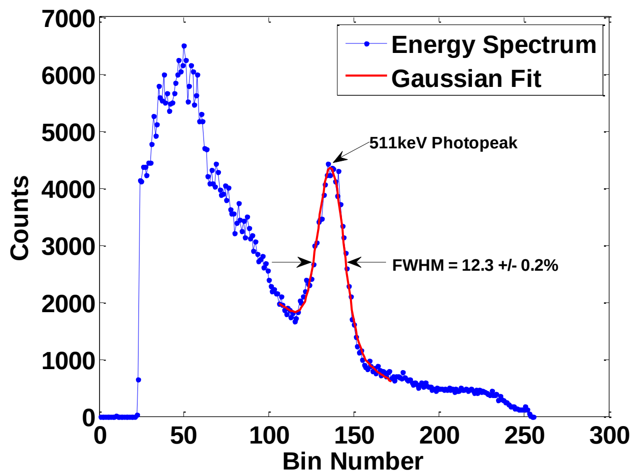

Figure 3.6 Energy spectrum of ^{22}Na for a 3x3x20mm^3 crystal with specular reflectors coupled directly to the SiPM without multiplexing. Note that the 1.27 MeV peak is lost due to saturation. Energy calibration was performed using three different energy peaks (not shown in the figure) before the energy resolution was calculated to ensure detector linearity.

2x2 Crystal Array

The results of the 2x2 crystal array are shown in figure 3.7 and table 3.2. Due to the symmetry of the multiplexing designs and the availability of crystals, only the quadrant occupied by the crystal array is studied. Results of the analysis of the spatial positioning using the line profile in the x and y dimensions across the 4th crystal indicated in the flood map are shown in table 3.3. The average PVR is 49.9 (resistor multiplexer) and 47.6 (capacitive multiplexer). Assuming the flood map is symmetric, the dynamic range is 1.02 (resistor multiplexer) and 1.81 (capacitive multiplexer), which is in good agreement with the simulation results shown in figure 3.4.

The global energy spectrum and energy resolution results, after correcting for gain variation among crystal pixels, are also shown in figure 3.7. It is observed that the resistor multiplexer has a lower energy resolution, 11.0±0.1%, than the capacitor case, 12.0±0.1%. The energy resolution for each crystal after crystal segmentation is summarized in table 3.2. The resolutions for the resistor multiplexer are slightly improved compared to those of the capacitive multiplexer.

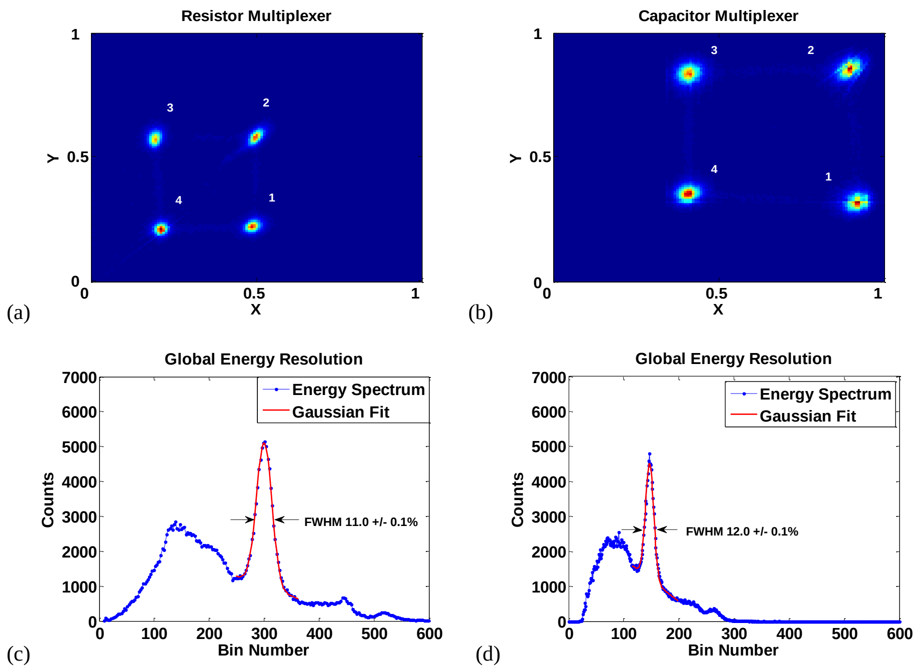

Figure 3.7 (a) and (b): Top right quadrant of the flood map produced using the 2x2 array. The numbers next to each crystal are used as reference for their spatial positions. (c) and (d): Global energy resolutions for the resistive and capacitive multiplexing, respectively. The data was not gated using the coincidence time window. The global energy resolution was obtained by scaling the raw energy data for each crystal by a factor to account for gain variations among pixels. The difference in peak positions between the two arises from differences in detected signal amplitudes. The energy resolutions of individual crystals can be found in table 3.2.

Table 3.2**:** Energy resolutions for individual crystals from 2x2 LYSO crystal array for both multiplexing schemes.

Crystal	Energy Resolution	
	Resistor Multiplexer	Capacitor Multiplexer
1	11.5±0.4%	12.8±0.4%
2	10.5±0.3%	10.7±0.3%
3	11.3±0.4%	11.8±0.3%
4	11.2±0.4%	12.7±0.2%

Table 3.3: Figures of merit for all combinations of pixelated crystal arrays and multiplexing schemes based on flood histogram data.

Scheme	Resistor Multiplexer		Capacitive Multiplexer	
Crystal Design	2x2 Array	6x6 Array	2x2 Array	6x6 Array
Peak-to-Valley Ratio (Avg)	49.9	7.95	47.6	10.64
Dynamic Range (Row)	1.02	1.01	1.81	1.78

6x6 Crystal Array

As mentioned earlier, the study of the 6x6 array of 2x2x20 mm^3 LYSO crystals is similar to the 2x2 array, except for two changes made here: a thin light guide of 1 mm height was added to provide light multiplexing; coincidence gating was applied to help improve the efficiency and effectiveness of the signal processing.

First, spatial analysis was performed using the line profile in the x and y dimensions across the center pixel indicated in red (figure 3.8) and the numerical results are shown in table 3.3. The average PVR is 7.95 for the resistive multiplexer, and 10.64 for the capacitive multiplexer. Such a significant difference is not observed for the 2x2 array. The dynamic ranges are 1.01 and 1.78, respectively.

Next, the global energy spectrum and energy resolution results, after correcting for gain variation among crystal pixels, are also shown in figure 3.8. The energy resolution for crystals from one quadrant of the array after segmentation can be found in figure 3.9 and table 3.4, with respect to “best”, “worst”, “center” and “corner” referencing the crystal position and results. As predicted, the results for the 2 mm array are consistently inferior compared to that of the 3 mm array, as shown in table 3.2, due to the reduced light detection associated with the smaller crystal size, reflections on the light guide, and crystals positioned above detector dead space. It is also observed that the resistor multiplexer consistently provides improved energy resolution performance. For both schemes, the corner crystals exhibit inferior energy resolution compared to the center crystals. Taking the resistive multiplier for an example, the energy resolution is 18.8±1.1% (center) and 21.5±1.6% (corner), respectively. Similarly, an unexpected difference of nearly 14% is found between the “best” case and “worst” case, which we believe is largely due to other factors rather than the multiplexing schemes themselves. In our study, the "worst" energy resolution is always found for those crystals on the edge of the array, which suffer most significantly from several factors including edge compression within the light diffuser and dead space inside/between detectors (Peng et al., 2011).

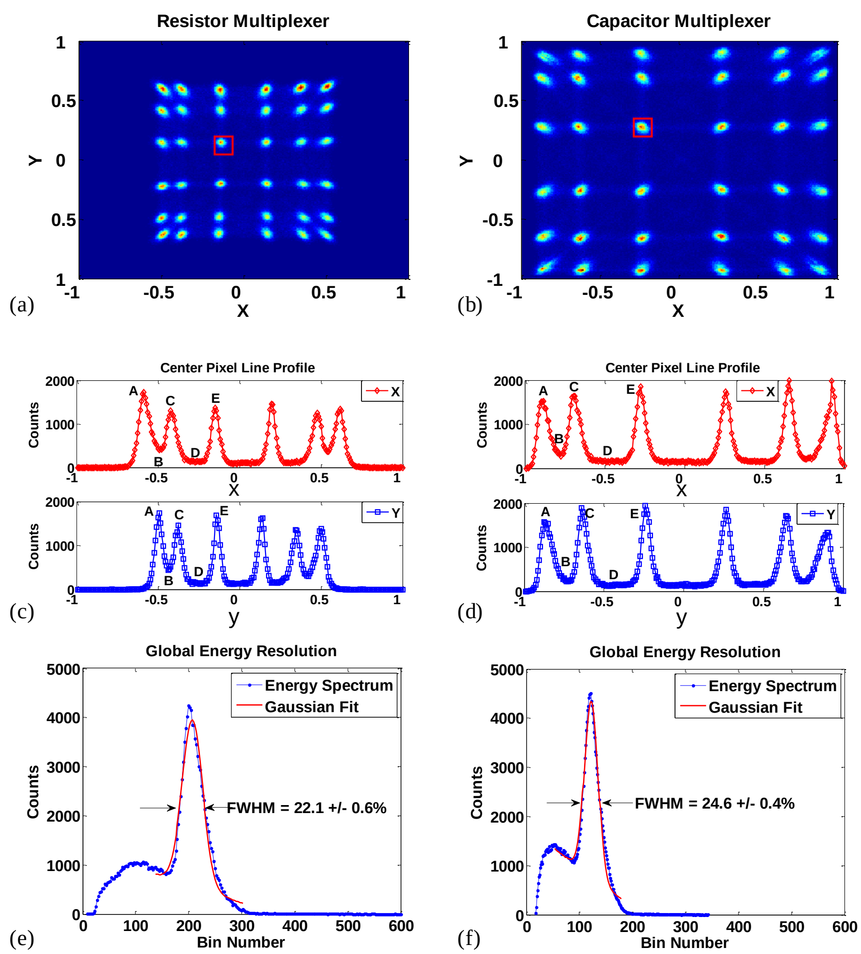

Figure 3.8 (a) and (b): Flood maps produced using the 6x6 array coupled to the SiPM using a 1 mm thick optical diffuser. The highlighted peak (red square) is used to produce the line profiles of (c) and (d). PVRs were calculated using the maximum peak value at peak 'A' divided by the minimum valley value at valley 'B' for both the 'x' and 'y' directions. This process is repeated for all pairs C:B, C:D, E:D and so on for all peaks to calculate the average PVR for comparison shown in Table 3.3. (e) and (f): Global energy resolutions for the two schemes with a coincidence time window applied to reduce the effect of scatter and higher energy interactions.

Table 3.4**:** Energy resolutions for various crystals from one quadrant of the 6x6 pixelated crystal array for both multiplexing schemes.

	Resistor Multiplexer	Capacitor Multiplexer
Best	16.4±0.7%	19.5±0.6%
Worst	29.8±1.6%	30.0±0.9%
Center	18.8±1.1%	20.0±0.7%
Corner	18.0±1.1%	26.2±1.0%

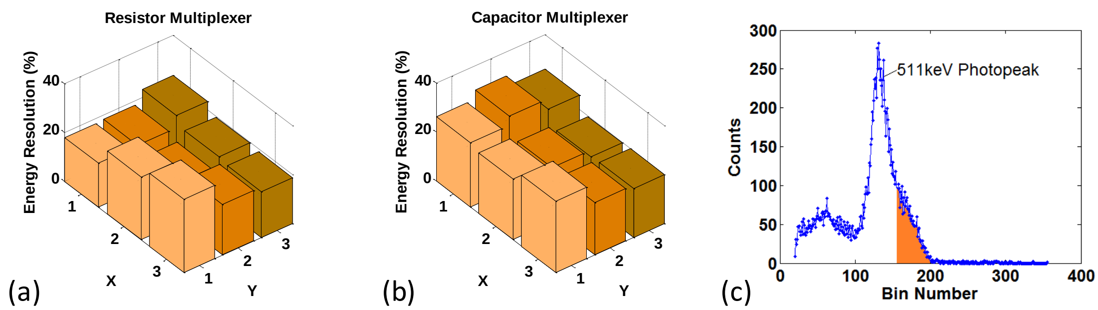

Figure 3.9 (a) and (b): Energy resolutions for the top left quadrant of the 6x6 array. Only one quadrant is displayed due to the symmetry of the multiplexing designs. X and Y coordinates refer to the crystals in the array, starting with the top left at (1, 1); the centermost crystal is (3, 3). (c): An example of the energy spectrum for a single crystal in the capacitive multiplexing scheme, showing the distortion of the 511keV photopeak highlighted in orange. This effect is not present in all crystals and is believed to be caused by gain variation between SiPM pixels and light multiplexing.

3.3.3 Experimental Results: Timing Performance

Single Crystal without Multiplexing

The time spectrum of a 3x3x20 mm^3 LYSO crystal is shown in figure 3.10, with the energy-gating applied to both the SiPM and the PMT. The bias for the SiPM was set back to 30.3 V to better compare timing performance to the following experiments. However, this saturates the output signal of the SiPM in the region of the 511keV photopeak (specifically, to the right of the peak). This is done since the PMT aids in the energy gating of the coincidence events, and the count rate was low, such that higher energy interactions with the SiPM detector that would coincide with 511keV interactions in the PMT would be rare. In producing an energy spectrum, this would be unacceptable as the photopeak is distorted. The bin width of the time spectrum is 50 ps and the peak position depends on the parameters used for the CFD algorithm shown in equation 2.6. A time resolution of 904±9.4 ps is found for this case.

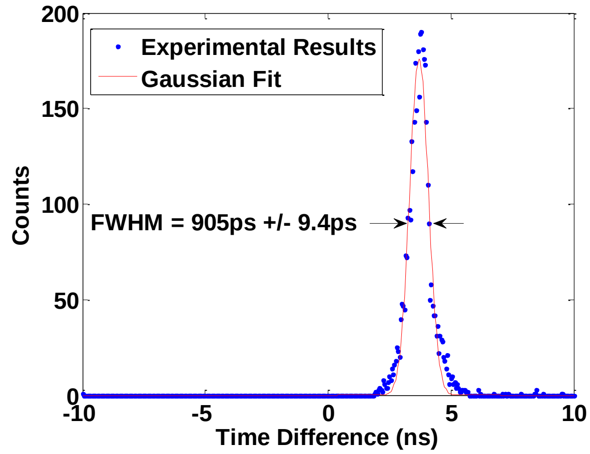

Figure 3.10 Time spectrum for the 3x3x20mm^3 LYSO crystal coupled directly to a SiPM pixel without multiplexing. The spectrum was produced using a digital CFD with values: f = 0.11, D(PMT) = 8 ns, D(SiPM) = 6 ns.

2x2 Array

The results of time resolution for the four crystals in the 2x2 array (see figure 3.7), are shown in figure 3.11 and 3.12 for the resistive and capacitive schemes, respectively. For the resistive multiplexer, the time resolutions (from crystal 1 to 4) are 1.78±0.03 ns, 1.59±0.03 ns, 2.03±0.03 ns and 2.39±0.03 ns, respectively. For the capacitive multiplexer, the time resolutions (from crystal 1 to 4) are 1.09±0.01 ns, 1.13±0.01 ns, 1.14±0.02 ns and 1.09±0.01 ns, respectively. The average value of the four crystals is 1.95±0.03 ns (resistive scheme) and 1.11±0.01 ns (capacitive scheme), which agrees with the simulation of the rise time slopes in section 3.3.1. In contrast to the results of the energy performance experiment, the timing performance for the resistive multiplexer exhibits a much stronger position-dependency compared to that of the capacitive scheme. In particular, the corner crystal has the best timing performance (1.59±0.03 ns) and the center crystal has the worst time resolution (2.39±0.03 ns), resulting in a degradation of nearly 63%.

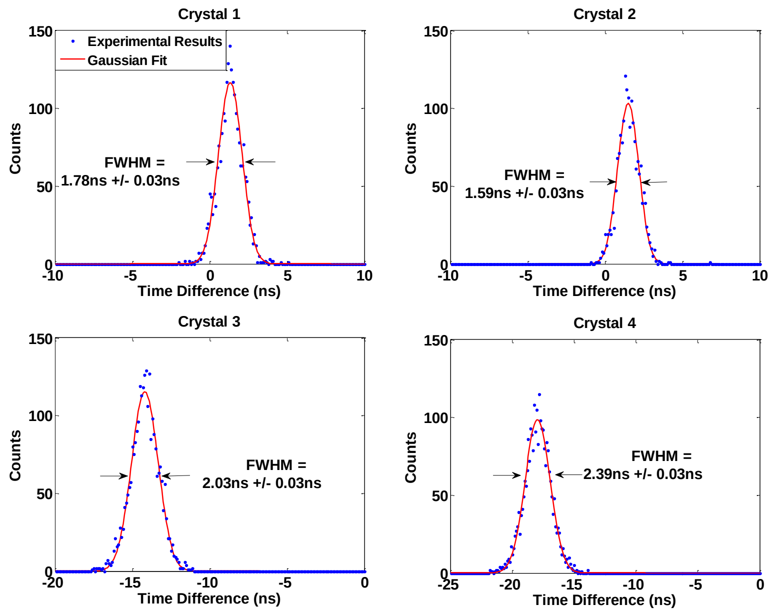

Figure 3.11 Time spectra for the 2x2 array using the resistive multiplexing scheme. Parameters of the CFD method were optimized on a per crystal basis. Due to this optimization step, different parameters were used for each crystal which and affects where the centroid of the peak occurs. CFD parameters for crystal 4 are: *f* = 0.16, *D(PMT)* = 8ns, *D(SiPM)* = 86ns.

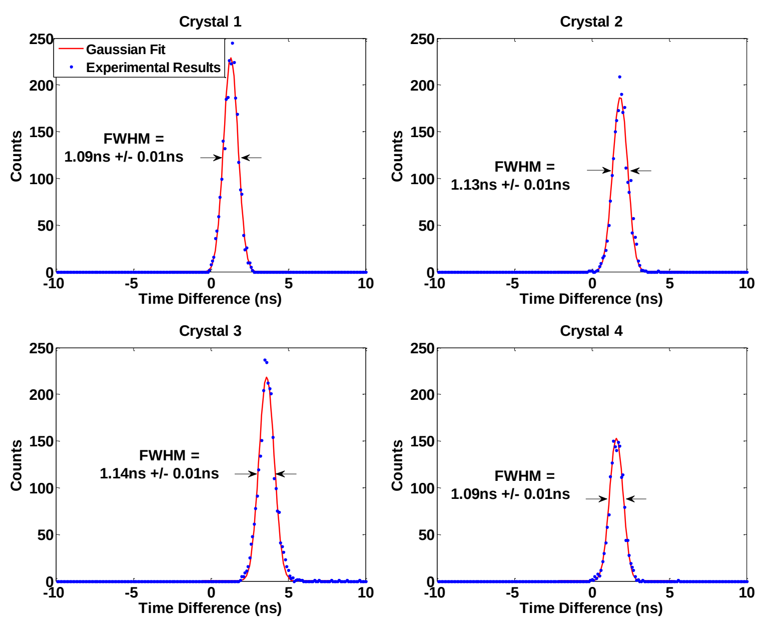

Figure 3.12 Time spectra for the 2x2 array using the capacitive multiplexing scheme. Parameters of the CFD were optimized on a per crystal basis as explained in figure 3.11. CFD parameters for crystal 4 are: *f* = 0.09, *D(PMT)* = 8ns, *D(SiPM)* = 61ns.

6x6 Array

The results of time resolution for the 6x6 array are presented in figure 3.13 and table 3.5. Due to the symmetry, only a quadrant of the full array comprising 9 crystals was selected. For the resistive multiplexer, the time resolutions (“best”, “worst”, “average”) are 2.83±0.06 ns, 3.76±0.13 ns and 3.21±0.10 ns, respectively. For the capacitive multiplexer, the time resolution is 1.61±0.01 ns, 2.03±0.01 ns and 1.74±0.03 ns, respectively. First, the results in table 3.5 clearly show that the capacitor multiplexer achieves superior timing performance over the resistive multiplexer. Second, due to the use of smaller crystals and a light guide, the average time resolution is inferior to that of the 2x2 array, degrading by approximately 71% and 64% for resistive and capacitive schemes, respectively. Third, a similar pattern is found in figure 3.13 as that of the 2x2 array: the center crystals in the resistor multiplexer have the worst timing resolutions while the capacitor multiplexer obtains very uniform time resolution for all crystals.

As this data was collected as coincidence events in the experiment in section 3.3.2, the problems with light collection for the edge crystals are still present and are responsible for the inferior timing performance, such as the 2.03±0.01 ns case in the capacitive scheme. The effect of this on the timing performance is less severe than on the energy performance and this result still agrees with the simulation.

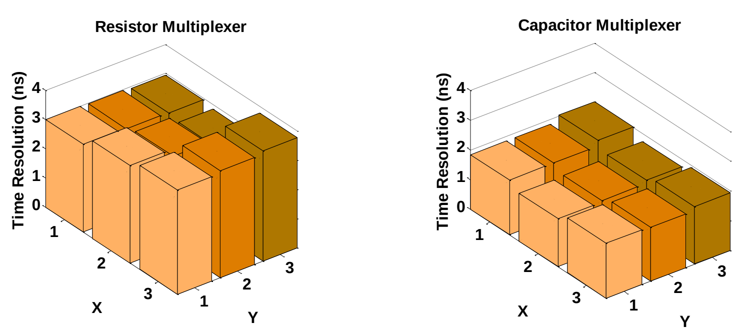

Figure 3.13 Time resolutions for the top left quadrant of the 6x6 array. X and Y coordinates refer to the crystals in the array (see figure 3.9). Time resolutions were determined by measuring the FWHM of the Gaussian fit performed on the timing spectra.

Table 3.5**:** Time resolutions (ns) for various crystals from one quadrant of the 6x6 pixelated crystal array for both multiplexing schemes.

	Resistor Multiplexer	Capacitor Multiplexer
Best	2.83±0.06	1.61±0.01
Worst	3.76±0.13	2.03±0.01
Center	3.76±0.13	1.93±0.01
Corner	3.02±0.02	1.84±0.01
Average	3.21±0.10	1.74±0.03

3.4 Discussion

3.4.1 Simulation Studies

Based on the results of our simulation, it is expected that that the capacitive multiplexer will have superior timing characteristics and good uniformity across the detector array, while the resistor scheme will have better timing at the corners relative to the center. The flood maps shown in figure 3.4 appear to be of much more clear separation than those in the experiments, which is due to noise factors not taken into account in the simulation such as light sharing, inter-crystal scattering, and the non-uniform gain of SiPM pixels. The simulation is able to assist in investigating the dependency of positioning capability on the SNR, which is a major challenge when implementing any multiplexing scheme. For example, the SNR performance of a single SiPM pixel would degrade by a factor of square root of N for a multiplexing ratio of N (i.e., a ratio of N = 4 when 16 channels are reduced down to 4), assuming the noise from different pixels are not correlated. Though such degradation may not be reflected from the measurement of energy resolution, it certainly affects the performance of spatial and time resolution and poses a limitation on the extent to which the multiplexing can be done.

There are several important factors to optimizing the multiplexing components for the system. First, an important consideration when splitting current amongst the components in these schemes is the input impedance of preamplifiers. A commonly used 50 Ω impedance amplifier is used in both simulations and experiments and acts as a constant load in series with the multiplexer components, regardless of pixel position, at the multiplexer outputs. The consequence of this is that for component values that are small or similar relative to this 50 Ω load, the input impedance will become the dominant factor in current distribution and result in less splitting of signal current among the outputs (i.e. less dynamic range). The second consideration is the parasitic capacitance of the SiPM pixel (assumed to be 50 pF in this study), which will affect the output signal, relative to the impedances in the multiplexing network, as it will act as a high impedance path for high frequency signals. Finally, the components of both multiplexing schemes interact with the output load (including parasitic capacitance, feedback capacitance, and input impedance of the preamplifier) and the parasitic capacitance of the detector to form RC circuits which may act as filters and attenuate output signals. These factors and their effect on performance must be considered when determining appropriate values for components.

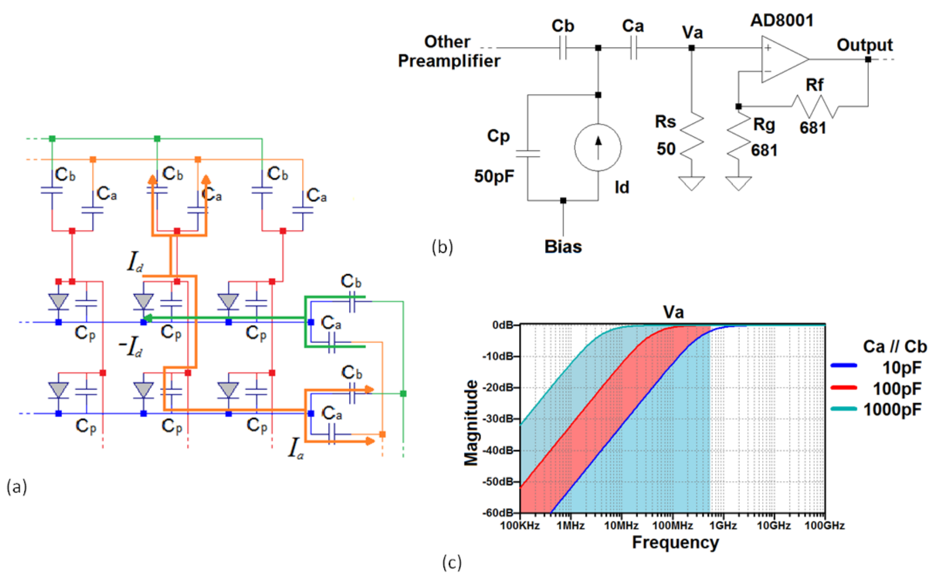

Figure 3.14 (a): A figure illustrating a potential alternate path taken by current across adjacent detector pixels experienced in simulation. The detector pixel is represented as the diode and its parasitic capacitance C_p. (b): The equivalent output circuit for one output rail of the capacitive multiplexer. The RC circuit is formed between C_a and R_s and acts as a high pass filter. The configuration of the preamplifier results in a bandwidth of ~440MHz. (c): The frequency response of the high pass filter in (b) is shown for 3 different values of the parallel combination of C_a and C_b (at the corner of the detector C_a and C_b are 80% and 20% of this value, respectively). The 440MHz bandwidth of the preamplifier is shown beneath each curve, and illustrates how much of the signal is attenuated in each case. In the 10pF case, the entire 440MHz bandwidth is attenuated at by at least 3dB.

For the capacitive multiplexing scheme, there are two possible charge loss mechanisms. The first is the alternative current path through adjacent detector units on the same row/column, as shown in figure 3.14a. For instance, in simulation a portion of the detector current, I_d, indicated by I_a (the second column), flows downwards into the second row, which then interferes with the signal on the opposite side of the diode I_d after it passes through the output capacitors, C_a and C_b. This explains why we observe a charge loss as much as 50% of the input current across a detector row, since the effective load between the two paths are on the same order of magnitude. This may have a larger impact in simulation than in experiments as the detector pixel is represented simply as a current source and its parasitic capacitance C_p. The change in bias voltage (due to quenching of the APDs within the detector pixel and leakage currents) would necessitate fluctuations in charge on this capacitance according to the voltage-current relationship for capacitors. More accurate simulation of the equivalent circuit of the detector pixel may better predict the effect (Seifert et al., 2009) and may be different between inactive and active modes (Aull et al., 2002); the parasitic capacitance may decrease substantially between these modes to reduce the effect of this alternate path. However, even if that is not the case, it should be noted that the effect on the current splitting should be the same for both signal and noise, and the signal quality in terms of SNR should remain the same. Olcott et al., (2005b) have reported charge loss paths in another multiplexing design; the key difference between these cases is that here possible charge loss occurs due to the parasitic capacitance of parallel detectors and not unintended nodal connections.

The second mechanism is the formation of RC circuits. Such impact has been well studied for the resistive multiplexer (Janececk et al., 2012) and it has a significant impact. Because of the impedance of the preamplifier, the capacitive scheme will introduce a passive RC circuit acting as a high pass filter, in contrast to the low pass filter formed in the resistive scheme (Janececk et al., 2012). To illustrate this, an equivalent circuit is shown in figure 3.14b and its frequency response is shown in figure 3.14c. The RC circuit is formed between C_a and R_s acting as a high pass filter. The frequency response is shown for 3 different values of the parallel combination of C_a and C_b (10 pF, 100 pF and 1000 pF), while the ratio between C_a and C_b remains constant (4:1 for the first column). The bandwidth of the selected amplifier (i.e., low pass) is 440 MHz. Figure 3.14c illustrates that as the total capacitance decreases, the corner frequency shifts to the right and the signal is attenuated in each case. In the 10 pF case, the entire amplifier bandwidth is attenuated at by at least 3 dB.

In summary, large resistors would be preferred to increase the impedance of the network (i.e. dynamic range) in the resistive multiplexer. However, simply picking large values would reduce the corner frequency of the RC circuits and reduce rising slopes, and thus timing performance. Similarly, for the capacitive multiplexer, the values of capacitor pairs are to be kept small to increase dynamic range. However, when they are selected to be too small the high pass filter has a corner frequency so high that much of the signal is attenuated. For example, increasing the capacitor values (C_a+C_b) from 100 pF to 1 nF would increase the signal amplitude by ~232% (in part because of the decrease in charge loss to parasitic capacitances), but reduce the dynamic range by ~60%. Within these constraints we arrived at the values shown in figure 3.1, as they provide good all-around performance based on the selected figures of merit.

3.4.2 Experimental Studies

The experimental results are consistent with our simulation results, with respect to energy resolution, time resolution, and flood histogram. The energy resolution of a PET detector mainly depends on two factors: Poisson statistics of light photons and detector/electronic noises while the time resolution depends on the slope-to-noise ratio (Spanadouki et al., 2007). Positioning performance depends on the positioning logic, light sharing, and SNR, as described in the previous work by Peng et al. (2011).

The most significant finding in this work is that the capacitive scheme has better dynamic range and timing performance, while the resistive scheme has better energy performance. The reasons for these differences are provided below. Referring to table 3.6, the total resistance between a detector pixel and its nearest output (i.e. output A for the top left pixel, (1,1) in figure 3.1) is between 575 to 930 ohms in the resistive scheme, while the capacitance between the detector pixel and the outputs (i.e. the top left pixel to any output A through D) in the capacitive scheme is between 20 and 80 pico-farads. The impedance of the preamplifier is the same for both cases. At frequencies of ~500 kHz, the impedances of both multiplexing schemes are similar. However, as the frequency increases to ~10-100 MHz (corresponding to a scintillation pulse with a rising edge time in the ns regime), the impedance of the output capacitors in the capacitive scheme are much higher (several kilo-ohms) than the input impedance of the preamplifiers at the outputs, compared to the resistive case, and this load has a much smaller effect on current splitting, as mentioned in the previous section, resulting in a higher dynamic range.

Table 3.6**:** Effective impedance (Ω) between detector nodes and outputs for one quadrant of the resistive multiplexer without preamplifiers.

Pixel	A	B	C	D
(1,1)	575	1.17k	1.24k	1.40k
(1,2)	916	1.11k	1.44k	1.49k
(2,1)	575	1.04k	815	1.10k
(2,2)	930	1.08k	1.11k	1.20k

The reason why the resistive multiplexing obtains slightly improved energy resolution in this work needs further investigation. Two important aspects should be mentioned prior to giving a possible explanation. First, both schemes suffer from the addition of noise from adjacent pixels (16 pixels in total) and the degradation of SNR in the same manner. Second, for the capacitive multiplexing scheme, though the signals from anode and cathode of a pixel are added together to derive the amplitude information, it does not improve the SNR as both signal and noise are doubled. No difference with respect to the energy resolution was found when only (A+B) or (C+D) was used instead of (A+B+C+D). Combined with the simulation results, the degradation of energy resolution is attributed to the attenuation of scintillation signals based on the aforementioned RC filter formed by the output load, splitting capacitors and parasitic capacitances of the detector, and the bandwidth of the operational amplifier used in the preamplifier. The capacitor values used in the capacitive multiplexer contribute to a high corner frequency (~ 31 MHz) in the RC circuit. On the other hand, for the resistor multiplexer, the RC circuit formed by the resistors and the parasitic capacitance of the preamplifier and detector pixels acts as a low-pass filter (with the corner frequency of around 2.1 to 3.5MHz). Considering the preamplifier's bandwidth of ~440 MHz in this work, the capacitor scheme will attenuate the majority of this bandwidth, while the resistor scheme will only do so for the very high frequency components. These low frequency components contribute greatly to the amplitude of the signal and thus the high pass filter in the capacitor scheme will result in signal loss and poorer energy resolution. The resistor networks low pass filter results in the slower rising edge but will not attenuate signal as much as that for the capacitive case.

Another possible explanation for this discrepancy involves in the bias voltage applied to the detector pixels in each scheme. It has been mentioned that the gain of the SiPM pixel is related to its applied bias voltage, and increased gain will slightly improve energy measurements due to increased SNR based on the Poisson statistics of the SiPM gain. While care was made to match the resistance on both the anode and cathode of the detector using the bias resistors between schemes, this is a difficult task. Due to the nature of the resistive multiplexing scheme the resistance seen at the anode of the detector pixels is position dependent and based on the network of resistors, while in the capacitive scheme it is simply equal to the bias resistor. Though the differences are small, at the operating voltage of 30.3V a difference of approximately 50mV was observed between the applied bias voltages of the two schemes; the resistive multiplexer had a higher bias voltage. This difference occurs due to DC leakage current that causes a voltage drop across the resistor network and bias resistor of the capacitive scheme, altering the bias of the SiPM with respect to the applied voltage source. This small difference would account for ~2% of the applied voltage over breakdown which could have a significant effect on the detector performance. This effect could be alleviated by introducing a bias resistor and DC blocking capacitors between adjacent SiPM pixels, however this would likely have significant consequences in the performance and space requirement of the scheme.

Another important finding is position-dependent time resolution found in the resistive multiplexing scheme, which was not the case for the capacitive multiplexing. In particular, the corner crystals have the best timing performance as predicted by the simulation, due to its lower impedance to the nearest output preamplifier (i.e., 575 Ω between pixel (1,1) and output A); while the center pixel has the largest impedance to the nearest output channels (i.e., 930 Ω between pixel (2,2) and output A) and thus the lowest corner frequency in the filter that is formed (i.e., more attenuation of high frequency signals), resulting in the worst timing performance. Opposite this, the total impedance to the output rails remains the same for all positions in the capacitive scheme since the rising slope of the sum of the output signals provides consistent timing performance, as it is determined by the total capacitance from the parallel capacitor pairs C_a and C_b which is consistent between rows or columns. Such dependency has also been reported for the PSAPD (Wu et al., 2009), where a difference of 1.7 ns in the time resolution was found between corner and center crystals. In practice, a look-up table could be used to apply different time window settings for individual crystals to correct for this problem. Furthermore, it should be pointed out that such position-dependency could be improved at the cost of dynamic range and this may be advantageous in cases with very high PVR (i.e. good crystal separation) and/or without using light multiplexing. The analogous case in the capacitive multiplexer is the sacrifice of dynamic range to improve signal amplitude which may be advantageous in the same cases as mentioned previously.

3.4.3 Relevancy to PET Block Detector Design

Two crystal arrays were studied in this work. The 2x2 array (~3.1 mm pitch) is one-to-one coupling (except a very thin glass layer on the surface of SiPM array for packaging), with a multiplexing ratio of 4 (16 SiPM pixels to 4 channels). The 6x6 array (~2.1 mm pitch) involves both light multiplexing (a light diffuser of 1 mm height) and charge multiplexing, with a multiplexing ratio of 9 (36 crystals to 16 SiPM and then to 4 channels). The latter is able to achieve better spatial resolution and higher multiplexing ratio, at the cost of degraded energy and time resolution. In addition, the results presented in this work are produced using digital processing in place of standard nuclear imaging modules. This provides an advantage in that differences in pulse shape (i.e. rise time) arising from spatial encoding in the multiplexing schemes can be accounted for and their effects on energy resolution and spatial positioning minimized.

With regard to the shape of the 511 keV photopeak for the individual crystals in the 6x6 array as shown in figure 3.9c, there are two main factors: light multiplexing and possible gain variation among detector pixels. Due to the smaller crystal pitch (i.e. less than the SiPM pixel), light multiplexing is employed to spread the scintillation light among many pixels. If these pixels have different gain values, the resulting signal will reflect these differences and suffer from non-linearity. Furthermore, the dead space of ~0.2 mm width on the four sides of each SiPM pixel also contributes to non-uniform light loss for crystals. Gain is affected by the bias voltage of the detector, which was constant for all pixels in these experiments due to the detector design. Controlling it for each pixel separately would improve uniformity but this is only possible on a row by row basis with this SiPM array. Temperature also affects the gain of the detector, though temperature monitoring was performed during these experiments and no significant increase in temperature was observed in operation; the acquisitions were performed at 21^{o}C where the thermistor monitor stabilized. This result could also be contributed to positioning errors, such as sliding during acquisition, but after repeated experiments provided the same results this can likely be ruled out. These factors may also contribute to the improved energy resolution of crystal #2 in table 3.2. Gain variation is likely the biggest factor since the relative improvement (10.5±0.3% and 10.7±0.3% compared to all other crystals over 11%) is present in repeated experiments with the detector.

3.5 Conclusions

This work compared the timing, energy and spatial performance of two different multiplexing schemes. Simulations of both methods and examination of the properties of the resulting flood histograms and output pulse shapes were performed in order to predict the relative performance of each scheme. The simulation results were compared to experimental results and found to be in good agreement. The resistor based multiplexer had superior energy resolution (11±0.1% and 22±0.6%) to the capacitor based multiplexer (12±0.1% and 24±0.4%) for both the 2x2 and 6x6 crystal arrays. However, the capacitive multiplexer had superior timing performance (average of 1.11ns and 1.90ns) compared to the resistive multiplexer (average of 1.95ns and 3.33ns) as predicted by simulation for those cases.

The result of this comparison show that a multiplexing scheme based on capacitive charge division of the rows and columns has superior timing resolution and spatial performance, but poorer energy resolution, than a multiplexing scheme based on a resistor network for charge division. Specifically, the capacitive scheme showed a 70% improvement in dynamic range and 33% improvement in peak to valley ratio over the resistive scheme when using the large crystal array. The timing resolution of the capacitive scheme showed a greater than 40% reduction compared to the resistor network making it the more attractive option for time sensitive applications, such as time-of-flight PET. The resistor network did display a 10% reduction in energy resolution and comparable PVR in cases without light multiplexing and may still be a useful tool in time insensitive modalities such as single photon emission computed tomography. Both schemes did cause some performance reduction compared to a scheme without any multiplexing in exchange for a reduction in cost and complexity of the system. As a result of this study, the multiplexing scheme best suited for the applications will be employed in future work and will reduce the channel density of a PET ring based on this design by 75% over those without charge multiplexing. In the future, we hope to continue improving these designs and explore other, newer, multiplexing solutions based on our experiences in these experiments with this system.

Chapter 4

Investigation of an Electro-optical Coupling System for PET/MR Block Detectors

4.1 Introduction

Section 1.3 looked at the potential benefits of merging PET and MRI technologies as well as the mutual interference of the two systems that makes this a challenging task. It is no surprise that many groups have stepped up to this challenge and developed both prototype and commercial PET/MR systems and ring inserts. One aspect of the PET/MR system design is addressing the mutual interference between the two systems, particularly with respect to shielding and the design of the PET detector.

In order to prevent eddy currents forming in the PET electronics, any vulnerable parts of the PET detector that are located inside the magnet are shielded, typically by copper. As the name implies, doing this shields the contained components from the magnetic field. España et al. (2010) found that shielding reduced the interference of the RF pulse on the output of a SiPM by a factor of ~24. Materials can provide shielding because the amplitude of an electromagnetic wave decays exponentially as it passes through a conductor. The skin depth of a material describes this decay and is based on the frequency of the wave and the conductivity and magnetic susceptibility of the material; at high frequencies tens of μm of copper will cause ~99% attenuation (Ulaby, 2006). However, the presence of this shielding causes fluctuations in local magnetic fields, and the time-varying magnetic fields induce eddy currents in the conductor, both of which interfere with the MRI. Peng et al. (2010) examined different shielding lengths and configurations inside the bore of a 7T magnet, placed near a typical birdcage coil. They found that at a distance from the isocenter of the FOV of the MRI, interference was mostly negligible; though this distance depends greatly on the magnet strength. Close to the isocenter, shielding caused significant shifts in the resonant frequency of CH_2 in a chemical shift imaging protocol designed to measure the effects of the eddy currents. The authors note that designs that deviate from a solid cylindrical shield reduce the interference enough to potentially be used at the center.

Regardless of this interference, many groups have designed PET/MR ring inserts that place the scintillation detectors inside of the MRI bore using shielded cables and enclosures. Most recent among these groups are Wehrl et al., in 2011, Yoon et al., in 2012, and Hong et al., in 2013. Wehrl et al. report significant decreases in MRI SNR with the PET components present, but negligible changes in image homogeneity in most cases. Yoon et al. report a drop in MRI SNR from 27.1 to 23.4 in the presence of their PET insert. Finally, Hong et al. recently reported a very significant drop in MRI SNR during gradient and spin echo sequences using their gold and aluminum shielded insert. However, none of these groups reported significant interference from the MRI in the PET electronics.

To avoid this interference, many recent designs have investigated the use of fiber optics to place as much of the PET components outside the MRI as possible. One approach is to couple scintillation crystals to the detector using long optical fibers, thus placing the detector and electronics outside of the FOV of the MRI, and with long enough fibers, outside of the field entirely allowing for the use of PMTs. Mackewn et al. (2005) introduced 3.5m fibers between the crystals and PMTs located outside the magnetic field and found that 70% of scintillation photons were lost in transmission resulting in a 45% energy resolution and 10.9ns coincidence time resolution. Catana et al. (2006) used much shorter fiber bundles of approximately 10cm length. They were able to test their insert within an MRI and found no significant change in its performance. However, the PET system suffered from light loss in the curvature of the fiber bundles (up to 50%) and slight rotation of the flood histogram. The consistent theme of these experiments has been loss of scintillation signal via the transmission in the optic fibers. Hong et al. in 2011 examined this practice via simulation and experimental validation and found that collecting scintillation light using fiber bundles can reduce light output by as much as 90% in some cases.

In order to avoid the loss of scintillation photons in this manner, Olcott et al., (2009a) developed a PET detector using an electro-optic coupling system, intending to place the entire scintillation detector inside the bore, and transmitting the detector signal to electronics outside of the room. The laser is driven by the single pixel detector (3x3mm^2 SensL SiPM) current directly, and no other active electronics are present in the front-end design. The group found no significant degradation in PET performance between the electro-optic system and standard coaxial cables for transmission. The lack of coaxial cables and small size of the detector block will increase compatibility with the MRI system over other cases which tend to require comparatively more shielding.

In light of these developments, this work focuses on bringing together the multiplexing designs discussed in Chapter 3 with the electro-optic coupling design to produce an MRI compatible PET block detector. This device would significantly reduce the number of signal channels due to the multiplexing scheme which complements the inclusion of the electro-optical coupling stage which is typically more expensive than a simple coaxial cable. Novel to the design is the inclusion of an active laser driver to compensate for the reduced signal amplitude caused by the analog multiplexing scheme.

4.2 Methods

4.2.1 Materials

The materials used in this experiment are mostly described in section 2.1.1 though a few new components are introduced. For the optical communication system, the laser used was the OPTEK OPR2800V, a vertical-cavity surface-emitting laser (VCSEL) in a circuit board surface mounted package. This device was chosen for its lack of ferromagnetic components (common in fiber connector components) and small package design since space is at a premium. The receiver photodiode is the OPTEK OPF432, a p-i-n photodiode in a standard ST-connectorized package. The fiber optic components used to connect these two devices were supplied by CXFiber and OZOptics. CXFiber worked extensively with us to design a ceramic board mounted receptacle for the optical fiber, and a magnetic compatible, large core fiber pigtail for easier coupling to the VCSEL. The fiber used is a 2m long 100/125μm multi-mode fiber (MMF), referring to its 100μm core and 125μm cladding outer diameters. The MMF is FC connectorized due to availability. Due to the mismatched connectors, and relatively short cable, an additional 3m long FC-ST connectorized MMF of the same core size was supplied by OZOptics. These additional components can be seen in figure 4.1. Only the 2x2 LYSO crystal array was used in this work.

The VCSEL is butt-coupled to the MMF using the optical grease. This method has shown to be effective with between 56% and 90% coupling efficiency to a 50μm core MMF dependent upon a variety of factors; 100μm core MMF would then expect even better results (Heinrich et al., 1997, Kim et al., 2007). The decision to use butt-coupling came about due to detector block size considerations and the complexity of incorporating a lens in the packaging design.

4.2.2 Optical Communication System

In this experiment the signal chain is divided into two sections and connected via an electro-optical coupling system. The first stage, the transmitter, of the signal chain includes the multiplexing scheme and scintillation detector, and the laser and associated driver circuit. This circuitry is implemented on a series of small, stacked circuit boards measuring 5.15x1.55x1.5cm^3 (including scintillator crystal and connectors) as seen in figure 4.1b. The multiplexing scheme used in this work was the resistive multiplexer (figure 3.1a). It was chosen based on the simulation results from chapter 3, as both projects were developed simultaneously due to time constraints. The multiplexing scheme showed excellent noise characteristics in simulation and it was hoped that any loss in SNR from the insertion of the optical equipment would have a smaller effect on positioning.

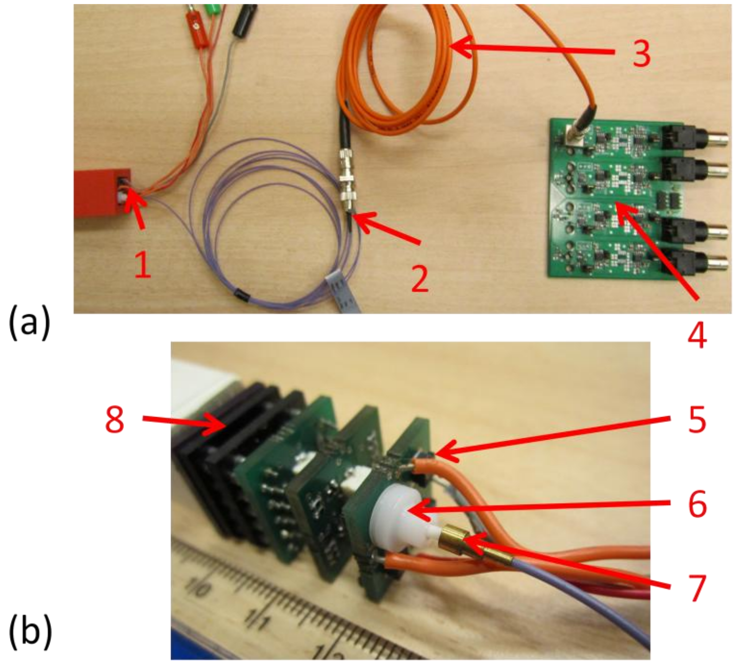

Figure 4.1 Electro-optic coupling system and block detector stack. (a) shows the complete apparatus. (1) The stacked circuit boards of the PET block detector in the container. (2) CXFiber MMF with FC connector. (3) OZOptics FC-ST MMF. (4) Receiver circuit board, with OPF432 connected. (b) close up of PET block detector stack. (5) OPR2800V VCSEL diode. (6) Ceramic fiber connector for the VCSEL. (7) CXFiber MMF pigtail with copper ferrule. (8) Scintillation detector, crystal, and multiplexing board.

The output of the multiplexer is used to drive the laser signal via the laser driver, and the laser stage can be seen in figure 4.2. The circuit is based on a 'simple analog laser driver' (Säckinger, 2005), using the preamplifier in figure 2.5 as the linear amplifier. The purpose of the circuit is to keep the VCSEL at the lasing threshold of its linear range (in DC), such that the voltage produced at the output of the linear amplifier will cause current to flow through the laser which is reflected as an analog optical signal (in AC). In order to achieve this, AC and DC coupling are employed using the capacitors and inductors (radiofrequency choke), as shown in figure 4.2. Since we are transmitting analog signals it is a requirement that the amplifier and VCSEL response be linear, else the signal shape would be distorted on the receiving end. The resistor R_{out} is the R_o

resistor at the corner in figure 3.1a; no AC stage is present in the preamp, as the capacitor C_1 accomplishes this.

The next stage of the signal chain includes the receiver circuit and the front end electronics discussed in section 2.1.2. The receiver circuit is a shunt feedback transimpedance amplifier and is illustrated in figure 4.3 with transimpedance gain approximately equal to $-R_f$ (Säckinger, 2005),. Unlike the SiPM signal, the magnitude of the p-i-n photodiode receiver signal is in the microampere regime and additional gain is required; the low impedance front end is insufficient and simply increasing the impedance would limit the bandwidth and potentially attenuate the signal. The shunt feedback amplifier improves the bandwidth (equation 2.1) by a factor of the op-amp's gain bandwidth and is able to achieve appropriate gain without attenuation (Säckinger, 2005). The signal processing electronics feature a non-inverting amplifier in place of the unity gain buffer of figure 2.8 in order to correct for gain differences between channels. Figure 4.4 shows the transmission of a signal generator pulse (square wave, $500mV_{pp}$, 500ns duration) from the multiplexing stage to output, and a typical SiPM signal. Note that the output signal in figure 4.4a has more noise in the transmitted square wave. This noise is expected to be present on the output of the system in figure 4.4b, though no input reference was measured. The output signal in figure 4.4b has a longer decay time than the signals from figure 2.6. Possible reasons for the discrepancy will be discussed later.

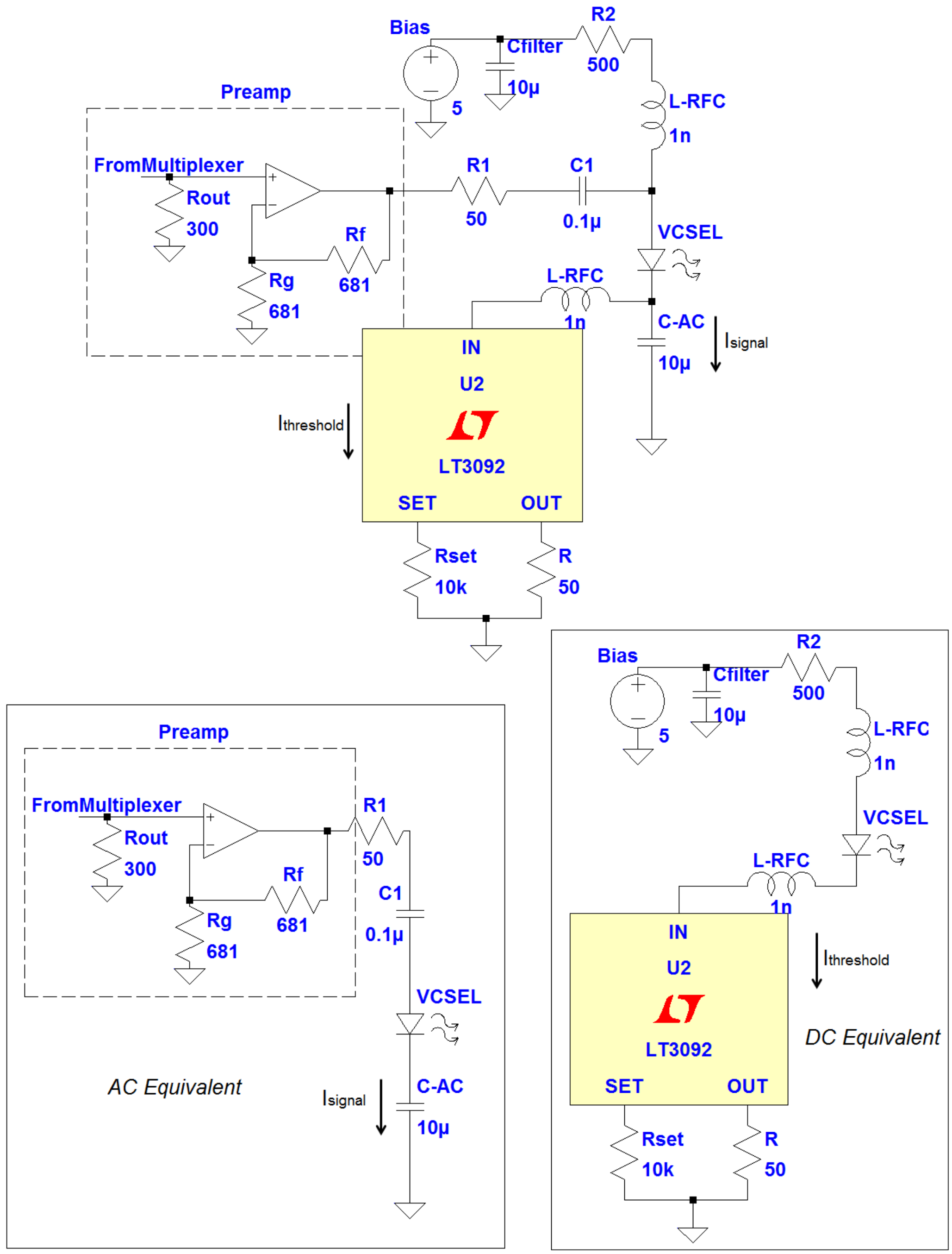

Figure 4.2 Circuit diagram for VCSEL laser transmitter stage. Top: Actual circuit implementation. Bottom: AC and DC equivalent circuits, showing that the preamp modulates the laser current via I_{signal}, and the DC current source, LT3092, keeps the laser at the lasing threshold via $I_{threshold}$.

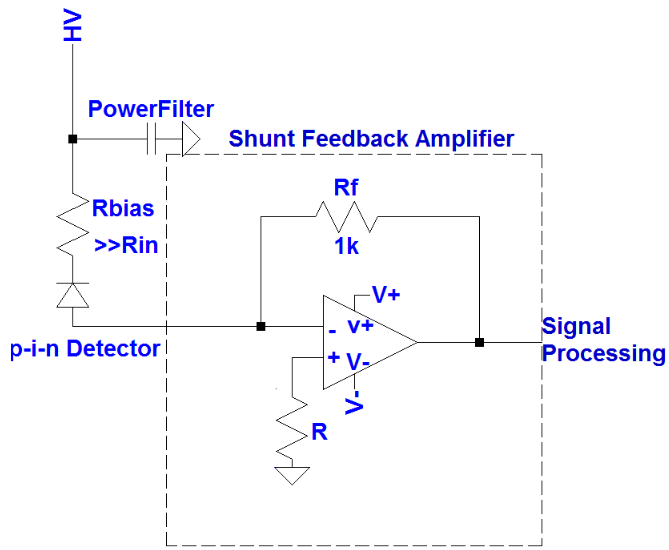

Figure 4.3 Shunt feedback transimpedance amplifier circuit for the p-i-n photodiode receiver. The resistor *R* is available to offset bias currents from the negative input. The output of this amplifier is the input to ADC after a filter and non-inverting amplifier stage.

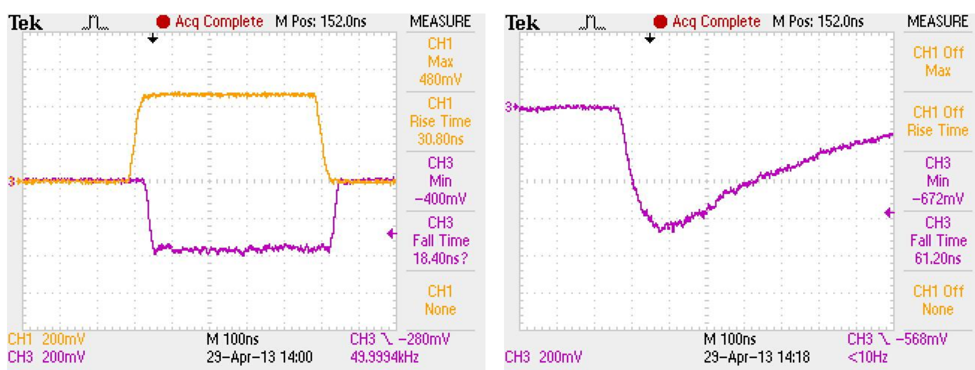

(a) **(b)**

Figure 4.4 Oscilloscope traces of the output of the electro-optic coupling system. (a) response of the system (purple) to a square wave input pulse of 500mV$_{pp}$ of 500ns duration (orange) applied to the bottom left corner position (1,4) in figure 3.1. (b) Typical scintillation detector response to 511keV annihilation photon event.

In order to compare the performance of the electro-optic coupling system to a typical copper trace system, an additional circuit board was produced. This board is similar to the receiver board, missing only the shunt feedback amplifier. In its place is a connector to the output of the linear amplifier of the transmitter; the entire laser stage is removed.

4.2.3 Experimental Setup and Figures of Merit

The experimental setup for this work is adequately described by section 2.2.1. Fibers were coiled and stored within the light tight enclosure, and the detector boards were housed in the apparatus as depicted in figure 4.5. FoMs are consistent with those presented in chapter 3. The focus of this section is on the effect of the electro-optic coupling system and the results directly compare the crystal array performance with and without it, thus no single crystal or multiplexing free cases are reported.

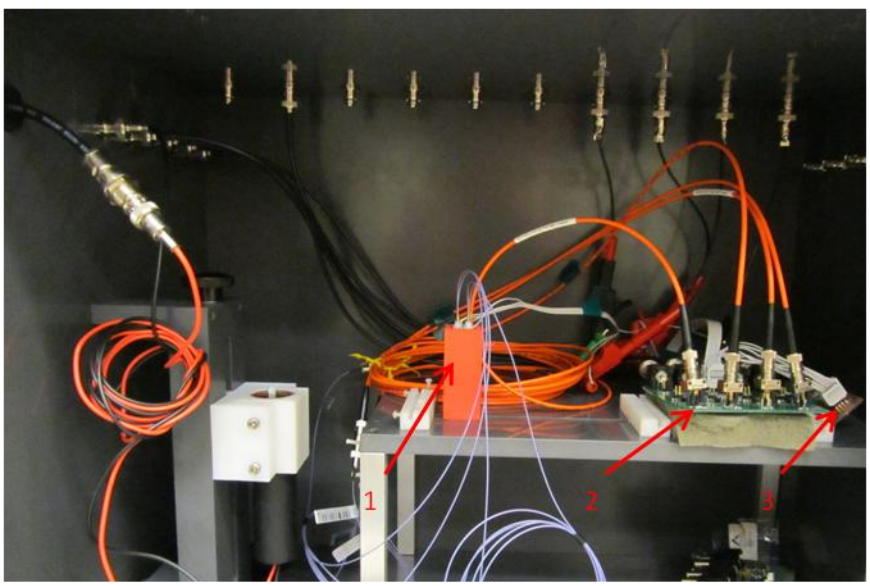

Figure 4.5 Electro-optic coupling system in the light tight enclosure. Stacked PET detector block could be supported on the white platforms for coincidence experiments for easier crystal coupling and source alignment (similar to figure 3.3). (1) Stacked PET detector block. (2) Receiver board. (3) Summing circuit and fast trigger.

4.3 Results

4.3.1 Experimental Results: Energy Performance and Flood Map

The results of the 2x2 crystal array with and without the electro-optic coupling system are shown in figure 4.6 and table 4.1. As before, due to the symmetry of the multiplexing designs and the availability of crystals, only the quadrant occupied by the crystal array is studied. The average PVR is 12.7 when the fiber optics are present and 84.7 using the circuit board adapter with no fiber optics, calculated from crystal 1 indicated in the flood map. Assuming the flood map is symmetric, the dynamic range is 0.81 (with fiber optics) and 1.26 (without). In general, the electro-optic coupling system had poorer flood map performance.

The global energy spectrum and energy resolution results, after correcting for gain variation among crystal pixels, are also shown in figure 4.6. It is observed that the fiber coupled case has a higher energy resolution, 14.6 ± 0.4%, than without the fiber coupling, 13.8 ± 0.4% and the individual crystal performance is found in table 4.1. It is evident that the introduction of the laser and fiber optics affected the energy and spatial performance.

Table 4.1**:** Energy resolutions for individual crystals from 2x2 LYSO crystal array for both cases.

Crystal	Energy Resolution	
	Electro-optic Coupling	Without Coupling
1	12.4±0.7%	11.6±0.6%
2	15.4±0.6%	12.9±0.8%
3	15.3±0.8%	12.9±0.7%
4	14.8±0.4%	12.0±0.3%

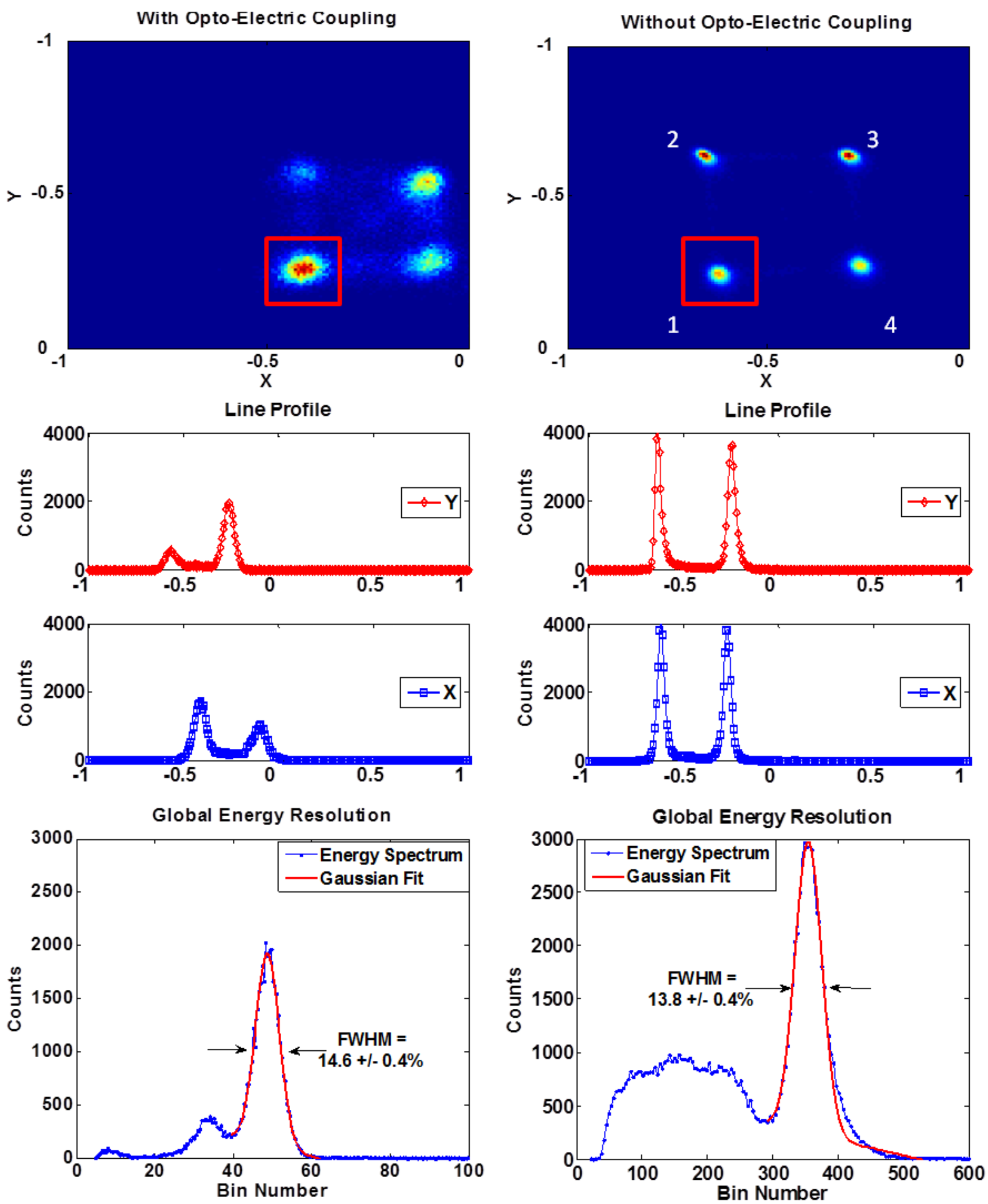

Figure 4.6 (a) and (b): Flood maps produced using the 2x2 LYSO crystal array with and without electro-optic coupling system. The highlighted peak (red square) is used to produce the line profiles of (c) and (d). The average PVR values are 12.7 for the case with the fiber optics, and 84.7 for the case without. (e) and (f): Global energy resolutions for the two cases with a coincidence time window applied to reduce the effect of scatter and higher energy interactions. Crystals can be referred by number as indicated in the flood map on the right.

4.3.2 Experimental Results: Timing Performance

The timing performance of the four crystals in the 2x2 crystal array are shown in figure 4.7 and 4.8 for the two cases, respectively. For the case with fiber optics, the time resolutions (from crystal 1 to 4) are 4.8±0.1 ns, 3.4±0.1 ns, 4.5±0.1 ns and 11.2±0.4 ns, respectively. For the case without fiber optics, the time resolutions (from crystal 1 to 4) are 2.01±0.02 ns, 1.99±0.02 ns, 3.47±0.04 ns and 3.53±0.05 ns, respectively. The average value of the four crystals is 6.0±0.2 ns (with) and 2.75±0.03 ns (without), which indicates significant degradation of timing performance when using the laser communication system. As the resistive multiplexing scheme from chapter 3 was employed in the detector, it is expected that the time resolution is position dependant. In particular, using the fiber optics, the corner crystal has the best timing performance (3.4±0.1 ns) and the center crystal has the worst time resolution (11.2±0.4 ns). However, the performance of the center crystal in this case is significantly worse than expected, even after repeated experiments. It is worth noting that the timing performance in general is poor compared to the results of section 3.3.3.

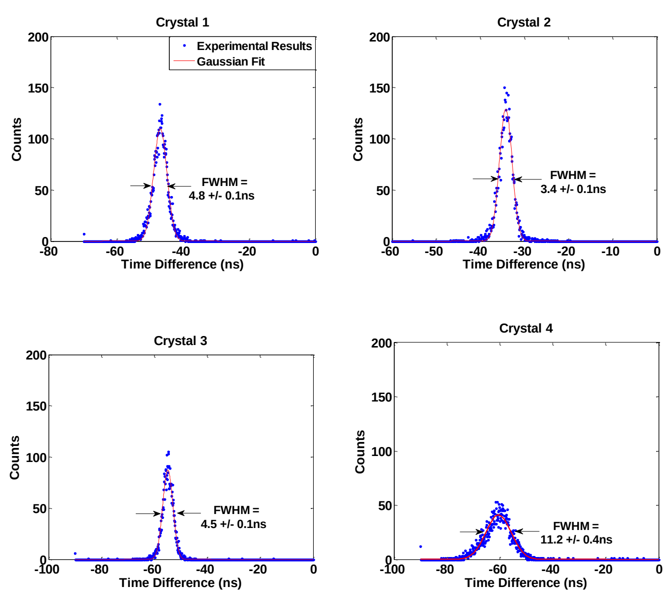

Figure 4.7 Time spectra for the 2x2 array while using the electro-optic system. Parameters of the CFD were optimized on a per crystal basis as explained in figure 3.11. CFD parameters for crystal 1 are: f = 0.21, $D(PMT)$ = 8ns, $D(SiPM)$ = 90ns.

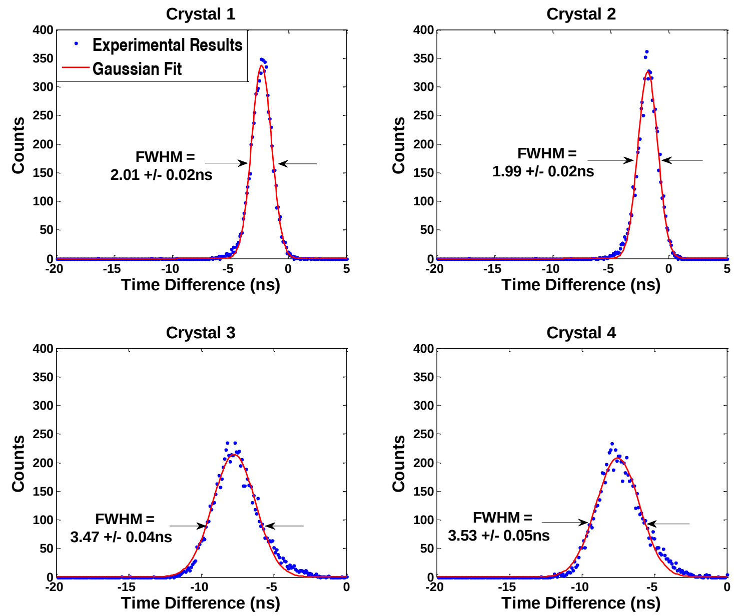

Figure 4.8 Time spectra for the 2x2 array without using the electro-optic system. Parameters of the CFD were optimized on a per crystal basis. CFD parameters for crystal 1 are: *f* = 0.20, *D(PMT)* = 8ns, *D(SiPM)*

4.4 Discussion

This work compares the performance of a PET block detector utilizing the 2x2 LYSO crystal array and resistive multiplexing scheme with and without the electro-optical coupling system. It is obvious from the results that the inclusion of the coupling system had a significant detrimental effect on the detector's performance, contrary to the results of the previous group with a similar experiment (Olcott et al., 2009a). Furthermore, the performance of the detector even without the coupling system was worse than the resistive multiplexer case of chapter 3 in both energy and time resolution. This section discusses some of the possible explanations for these results.

To explain the change in performance between chapter 3 and 4, note that some changes were made to the front end electronics (multiplexing scheme, preamplifier, filtering) that would have a direct impact. It was mentioned that the same preamplifier design was used; however, the transimpedance in this case was 300Ω, simply using the corner resistor from figure 3.1 as the preamplifier impedance. This would actually improve dynamic range based on the discussion from chapter 3, and this is reflected in the flood map in the results; the dynamic range of the flood map is 1.26 vs. 1.02, PVR is 84.7 vs. 49.9 for the results without the coupling scheme and the resistive multiplexer results in chapter 3, respectively. As the total resistance of the network had decreased, timing performance should have also improved, though this was not the case. There were some changes made in the signal chain of the stacked circuit boards when compared to the circuit boards in section 3: connectors between boards in the stack, smaller components including op-amp packages, smaller, more disjointed ground plane due to the configuration, and an additional op-amp on the receiver board. All of these factors may contribute to an increase in noise in the circuit which would decrease the energy and timing resolution as described in chapter 1. Additionally, the bipolar shape of the output was not included as the triangular shaping method made it redundant. Though, this should not increase noise and baseline drift was not a significant factor due to the low activity and count rate used here.

With all other factors being the same between the two cases in this section, it appears that the electro-optic coupling system is to blame for the poorer performance. In general, the use of fiber optics can cause signal distortion due to attenuation, dispersion and nonlinearities (Säckinger, 2005). Attenuation occurs due to inefficient coupling, photon scattering and absorption by impurities, and loss at fiber interfaces. Dispersion is more prominent in MMF, and is a result of photons taking different paths through the fiber, called modes, each with a different propagation delay; resulting in the stretching of the output signal. Dispersion can also occur from modes at different wavelengths travelling at different speeds through the fiber, with similar effects (typically 17 ps/nm km for silicon) called chromatic and polarization mode dispersion. There are many sources of nonlinearities and all are proportional to the optical power output. Since we use very short fibers (<10m) and very low power (low mW), many of these effects are mostly negligible: chromatic dispersion, nonlinearities, scattering, and absorption, are all dependant on the length of fiber or optical power. It is evident from figure 4.4 that there is some delay in the signal chain, but the square wave did not show signs of dispersion or nonlinearities. However, the longer decay time of the scintillation signal in figure 4.4 is indicative of some dispersion, though the signal rise time (technically fall time since it is inverted) is comparable to the previous work.

There are 3 fiber interfaces: VCSEL to fiber, the FC-ST connection, and the fiber to photodiode; each interface will cause signal loss due to reflections. FC and ST typically experience insertion loss of 0.3 to 0.5dB according to fiber supplier Newport (2013). The VCSEL to fiber interface is the most problematic. The VCSEL and fiber are aligned with the help of the custom ceramic part and cured epoxy holds it in place; however, this was performed without the appropriate fiber optic staging equipment. As a result, each laser has a different coupling efficiency; from figure 3.1: Output C has the highest (normalized to 1), followed by D (0.9), A (0.5) and B (0.3). Gain was adjusted using the non-inverting amplifier mentioned in section 4.2 to attempt to normalize these signals. This improved results significantly, but each channel would vary slightly each time an experiment was performed. In particular, output B was the most problematic, often simply not transmitting at all or with poor SNR. It is possible that VCSEL was damaged, but with no additional components, and being encased in epoxy it was not possible to test for this by removing the suspect part. Figure 4.4 shows that there is certainly some attenuation as the output signal is smaller than the input despite the preamplifier stage and transimpedance amplifier at the receiver. This figure also shows that the output is slightly noisier in the ‘high’ signal portion of the square wave.

This increase in noise combined with the poor laser to fiber coupling can explain much of the disparity in the results. Crystal 4 had the poorest results, likely as a result of being relatively more evenly split amongst the 4 channels including the noisy output B. The flood map for this case in figure 4.6 is distorted compared to the case with no fiber, and is a result of the inconsistent channel amplitudes. In this case, output A was overcompensated and thus the Anger logic was biased towards that corner. Additionally, due to the higher amplitude, more counts were recorded for that location based on the trigger threshold. This problem could be corrected in software when using a full crystal array by normalizing all 4 channels; this was difficult using only one quadrant of the array since the 4 channels should not be weighted equally.

In addition to the topics discussed here, the discussion in chapter 3 also applies. As expected, timing performance is best at the corner (crystal 2) and worst in the center (crystal 4). Energy resolution is less consistent than in previous experiments, though still similar within the error values listed. Crystal 1 in particular had significantly better performance, though as this persisted across experimental cases may be related to the pixel in that SiPM array.

Despite the decreased performance, the block detector is comparable to other work despite the inclusion of the multiplexing scheme. Olcott et al. (2009a) reported energy and time resolution of 15.5 ± 0.4% and 1.32 ± 0.02ns, respectively for similar crystals, indicating an improvement in energy resolution. Comparing the resistive multiplexing case to the result with no multiplexing an increase of a factor of at least 2 in time resolution was expected. Compared to the previous groups working with no fiber optics, Yoon et al. (2012) reported 13.9% individual 1.5x1.5x7mm^3 LGSO crystal energy resolution and 1.23ns timing resolution, while Hong et al., (2013) reported 18.1 ± 2.1% average energy resolution and 4.23 ± 0.2ns timing resolution for similar LYSO crystals and SensL detector arrays.

4.5 Conclusions

This work examined the timing, energy and spatial performance of an electro-optic coupling system for a PET/MR block detector. Compared to a test case without the coupling system, all FoM were significantly affected. Energy resolution increased by ~6%, from 13.8 ± 0.4% to 14.6 ± 0.4%; timing resolution increased by ~120%, from 2.75±0.03 ns to 6.0±0.2 ns; and flood map performance decreased from PVR of 84.7 to 12.7 and was slightly distorted in shape.

Despite the affect on performance, the system still performed relatively well in comparison to recent developments in PET/MR insert systems. There are some improvements that could be made to help improve performance of the system. Firstly, the laser to fiber coupling could be improved greatly by having the parts professionally aligned and secured together; the current alignment is thought to be a major problem in the design. With improved coupling, the fiber itself could then be one continuous, single-mode fiber which can help with attenuation of the PET signals in transmission and reduce the cost of the system. Secondly, the multiplexing scheme could be further optimized for the design based on the discussion from chapter 3, and could improve position and timing performance.

This system shows promise, but still has much work to be done before a PET ring insert is feasible. Interference from the MRI system is not expected based on previous published work, but the effect on the MRI system will need to be investigated. Prior to that experiment, the immediate goal should be to address the performance issues presented here and scale up the design to multiple block detectors to form a detection ring.

Chapter 5

Conclusions and Future Directions

There were two projects completed in parallel as part of this thesis work: an investigation of multiplexing schemes and the development of an electro-optical coupling system for PET/MR detectors. In the former, the resistor based multiplexer had superior energy resolution (11±0.1% and 22±0.6%) to the capacitor based multiplexer (12±0.1% and 24±0.4%) for both the 2x2 and 6x6 crystal arrays. However, the capacitive multiplexer had superior timing performance (average of 1.11ns and 1.90ns) compared to the resistive multiplexer (average of 1.95ns and 3.33ns) as predicted by simulation for those cases. In the later, compared to a test case without the electro-optical coupling system, all FoM were significantly affected. Energy resolution increased by ~6%, from 13.8 ± 0.4% to 14.6 ± 0.4%; timing resolution increased by ~120%, from 2.75±0.03 ns to 6.0±0.2 ns; and flood map performance decreased from PVR of 84.7 to 12.7 and was slightly distorted in shape.

As a result of this work, we can first conclude that the capacitor based multiplexing scheme is well suited for applications requiring excellent timing performance. In addition, there are many considerations to be made when selecting the components of the two multiplexing schemes which may allow for a configuration that complements the needs of the detector system through a variety of trade-offs between spatial, timing and energy performance. Secondly, we have demonstrated the proof of principle for the electro-optical coupling system. Though it did have a significant effect on detector performance we believe future prototypes can be easily improved.

With regard to the multiplexing schemes there are two possible considerations for future work. First, including more multiplexing schemes in the comparison will help to improve our understanding of the strengths and weaknesses of analog multiplexing methods. The two multiplexing schemes presented in this work represent popular and recent designs, but other schemes exist which have been discussed briefly in chapter 3.

Secondly, novel multiplexing designs could be introduced using the knowledge gained from these experiments and be included in the analysis.

With regard to the electro-optical coupling scheme there are many recommendations for future implementations. First and most importantly, the coupling of the laser to the optic fiber must be improved. The logical approach would be to have the manufacturer of the custom MRI compatibly components assemble this portion of the system with high accuracy. Next, the fibers themselves could be simplified by matching the connector of the custom part to the photodiode of choice, thereby avoiding additional losses from fiber to fiber interfaces. The multiplexing scheme could be further optimized for the laser drive circuit. The capacitor scheme opens up driver designs utilizing differential inputs, and changes to the resistive multiplexing scheme may improve the timing performance without compromising the amplitude of the output signals (as discussed in section 3.4). Minor improvements in performance may be made by improving the experimental setup, particularly with respect to the alignment of the stacked circuit boards, detector, crystal array, radiation source and reference detector. Finally, the experiments will need to be repeated in the bore of the MRI to measure the mutual interference of the systems.

Additional Publications

Published

Yang, X., Downie, E., Farrell, T., and Peng, H. (2013). Study of light transport inside scintillation crystals for PET detectors. *Physics in Medicine and Biology*, *58*(7), pp 2143.

Accepted

Downie, E., Yang, X., and Peng, H. (2013). Investigation of Two Analog Charge Multiplexing Schemes for SiPM Based PET Block Detectors. *Accepted April 23, 2013 by Physics in Medicine and Biology*.

Bibliography

1. Ahmed, S. N. (2007). *Physics and Engineering of Radiation Detection*. Burlington: Elsevier Science.

2. Allemand, R., Gresset, C., and Vacher, J. (1980). Potential advantages of a cesium fluoride scintillator for a time-of-flight positron camera. *J. Nucl. Med.*, 21(2), 153.

3. Allen R. A., Burcham W. E., Chackett K. F., Munday G. L. and, Reasbeck P. (1955). Electron capture in the decay of sodium 22. *Proceedings of the Physical Society. Section A*, 68(8), 681.

4. Auffray, E., Frisch, B., Geraci, F., Ghezzi, A., Gundacker, S., Hillemanns, H., Jarron, P., Meyer, T., Paganoni, M., Pauwels, K., Pizzichemi, M., and Lecoq, P. (2011, October). A comprehensive & systematic study of coincidence time resolution and light yield using scintillators of different size, wrapping and doping. In *Nuclear Science Symposium and Medical Imaging Conference (NSS/MIC), 2011 IEEE* (pp. 64-71). IEEE.

5. Aull, B. F., Loomis, A. H., Young, D. J., Heinrichs, R. M., Felton, B. J., Daniels, P. J., and Landers, D. J. (2002). Geiger-mode avalanche photodiodes for three-dimensional imaging. *Lincoln Laboratory Journal*, *13*(2), 335-349.

6. Bailey, D. L., Maisey, M. N., Townsend, D. W., and Valk, P. E. (2005). *Positron Emission Tomography: Basic Sciences*. London: Springer-Verlag London Limited.

7. Bezrukov, I., Mantlik, F., Schmidt, H., Schölkopf, B., and Pichler, B. J. (2013, January). MR-based PET attenuation correction for PET/MR imaging. In *Seminars in nuclear medicine* (Vol. 43, No. 1, pp. 45-59). WB Saunders

8. Brix, G., Lechel, U., Glatting, G., Ziegler, S. I., Münzing, W., Müller, S. P., and Beyer, T. (2005). Radiation exposure of patients undergoing whole-body dual-modality 18F-FDG PET/CT examinations. *J. Nucl. Med.*, *46*(4), 608-613.

9. Budinger, T. F. (1983). Time-of-flight positron emission tomography: status relative to conventional PET. *J. Nucl. Med.*, 24(1), 73-78.

10. Budinger, T.F. (1998) PET instrumentation: what are the limits? *Semin Nucl Med. 28:247.*

11. Catana, C., Wu, Y., Judenhofer, M. S., Qi, J., Pichler, B. J., & Cherry, S. R. (2006). Simultaneous acquisition of multislice PET and MR images: initial results with a MR-compatible PET scanner. *J. Nucl. Med.*, *47*(12), 1968-1976.

12. Cherry, S. R., Sorensen J., and Phelps, M. E. (2003). *Physics in Nuclear Medicine (3rd ed.)*. Philadelphia, Pennsylvania: Saunders.

13. Cherry, S. R., Dahlbom, M., and Phelps, M. E. (2006). *PET: Physics, Instrumentation, and Scanners*. New York, NY: Springer Science+Business Media, LLC.

14. Cosentino, L., Finocchiaro, P., Pappalardo, A., and Garibaldi, F. (2012). Assessment of a high-resolution candidate detector for prostate time-of-flight positron emission tomography. *preprint, arXiv:1209.2257*.

15. Daube-Witherspoon, M. E., Surti, S., Perkins, A., Kyba, C. C. M., Wiener, R., Werner, M. E., Kulp, R., and Karp, J. S. (2009). The imaging performance of a LaBr3-based PET scanner. *Phys. Med. Biol.*, 55(1), 45.

16. Degenhardt, C., Prescher, G., Frach, T., Thon, A., de Gruyter, R., Schmitz, A., and Ballizany, R. (2009, October). The digital silicon photomultiplier—A novel sensor for the detection of scintillation light. In *Nuclear Science Symposium Conference Record (NSS/MIC), 2009 IEEE* (pp. 2383-2386).

17. Derenzo, S. E., Moses, W. W., Huesman, R. H., and Budinger, T. F. (1993). “Critical Instrumentation Issues for <2 mm Resolution, High Sensitivity Brain PET.” *Quantification of Brain Function.* Elsevier Science Publishers, Amsterdam, 25–37.

18. Dokhale, P., Stapels, C., Christian, J., Yang, Y., Cherry, S., Moses, W., and Shah, K. (2009, October). Performance measurements of a SSPM-LYSO-SSPM detector module for small animal positron emission tomography. In *Nuclear Science Symposium Conference Record (NSS/MIC), 2009 IEEE* (pp. 2809-2812).

19. España, S., Fraile, L. M., Herraiz, J. L., Udías, J. M., Desco, M., and Vaquero, J. J. (2010). Performance evaluation of SiPM photodetectors for PET imaging in the presence of magnetic fields. *Nuclear Instruments and Methods in Physics Research Section A: Accelerators, Spectrometers, Detectors and Associated Equipment*, *613*(2), 308-316.

20. Eriksson, L., Conti, M., Rothfuss, H., Melcher, C. L., Eriksson, M., and Zhuravleva, M. (2010). LuYAP/LSO phoswich detectors for high resolution positron emission tomography. In *Nuclear Science Symposium Conference Record (NSS/MIC), 2010 IEEE* (pp. 3122-3125).

21. Frach, T., Prescher, G., Degenhardt, C., de Gruyter, R., Schmitz, A., and Ballizany, R. (2009, October). The digital silicon photomultiplier—Principle of operation and intrinsic detector performance. In *Nuclear Science Symposium Conference Record (NSS/MIC), 2009 IEEE* (pp. 1959-1965).

22. Gerber, M. S., Miller, D. W., Schlosser, P. A., Steidley, J. W., and Deutchman, A. H. (1977). Position sensitive gamma ray detectors using resistive charge division readout. *IEEE Transactions on Nuclear Science, 24*(1), 182-187.

23. Gu Y, Matteson JL, Skelton RT, et al. (2011) Study of a high resolution, 3-D positioning cross-strip cadmium zinc telluride detector for PET. *Phys Med Biol*. 56, 1563–1584

24. Gundacker, S., Auffray, E., Frisch, B., Hillemanns, H., Jarron, P., Meyer, T., Pauwels, K., and Lecoq, P. (2012) A Systematic Study to Optimize SiPM Photo-Detectors for Highest Time Resolution in PET. *IEEE Transactions on Nuclear Science,* 59(5), 1798-1804.

25. Haacke, E. M., Brown, R. W., Thompson, M. R., and Venkatesan, R. (1999). *Magnetic resonance imaging: Physical principles and sequence design*. New York: Wiley-Liss.

26. Hamammatsu. (2011). *Monolithic MPPC array in SMD package S11828-3344M, product information.* Hamamatsu Photonics Solid State Division.

27. Hammer, B. E., Christensen N. L., and Heil B. G. (1994). Use of a magnetic field to increase the spatial resolution of positron emission tomography. *Medical Physics*, 21(12), 1917-1920.

28. Heinrich J., Zeeb E., and Ebeling K. J. (2007). Butt-Coupling Efficiency of VCSELs into Multimode Fibers. *IEEE Photonics Technology Letters*, *9*(12).

29. Heinrichs, U., Blume, A., Bussmann, N., Engels, R., Kemmerling, G., Weber, S., and Ziemons, K. (2002). Statistical studies on the light output and energy resolution of small LSO single crystals with different surface treatments combined with various reflector materials. *Nuclear Instruments and Methods in Physics Research Section A: Accelerators, Spectrometers, Detectors and Associated Equipment*, *486*(1), 60-66.

30. Herrero-Bosch, V., Colom, R. J., Gadea, R., Espinosa, J., Monzo, J. M., Esteve, R., Sebastia, A., Lerche, C. W., and Benlloch, J. M. (2008). PESIC: An integrated front-end for PET applications. *IEEE Transactions on Nuclear Science, 55*(1), 27-33.

31. Hong, K. J., Choi, Y., Jung, J. H., Kang, J., Hu, W., Lim, H. K., Huh, Y., Kim, S., Jung, J. W., Kim, K. B., Song, M. S., and Park, H. W. (2013). A prototype MR insertable brain PET using tileable GAPD arrays. *Medical physics*, *40*(4).

32. Inadama, N., Murayama, H., Yamaya, T., Nishikido, F., Shibuya, K., Yoshida, E., Tsuda, T., Ohmura, A., Yazaki, Y., and Osada, H. (2008, October). DOI PET

detectors with scintillation crystals cut as triangular prisms. *Nuclear Science Symposium Conference Record, 2008. NSS'08. IEEE* (pp. 3942-3945).

33. Ito, M., Lee, J. S., Kwon, S. I., Lee, G. S., Hong, B., Lee, K. S., Sim, K., Lee, S. J., Rhee, J. T., and Hong, S. J. (2010). A four-layer DOI detector with a relative offset for use in an animal PET system. *IEEE Transactions on Nuclear Science*, 57(3), 976-981.

34. Ito, M., Lee, J. P., and Lee, J. S. (2012). Timing Performance Study of New Fast PMTs With LYSO for Time-of-Flight PET. *IEEE Transactions on Nuclear Science*, 60(1), 30-37.

35. Ito, M., Lee, M. S., and Lee, J. S. (2013). Continuous depth-of-interaction measurement in a single-layer pixelated crystal array using a single-ended readout. *Phys. Med. Biol.*, 58(5), 1269-1282.

36. Janecek, M., Walder, J., McVittie, P. J., Zheng, B., von der Lippe, H., McClish, M., Dokhale, P., Stapels, C.J., Christian, J.F., Shah, K.S., and Moses, W. W. (2012). A High-Speed Multi-Channel Readout for SSPM Arrays. *IEEE Transactions on Nuclear Science, 59*(1), 13-18.

37. Kadir, A., Almkvist, O., Forsberg, A., Wall, A., Engler, H., Långström, B., and Nordberg, A. (2012). Dynamic changes in PET amyloid and FDG imaging at different stages of Alzheimer's disease. Neurobiology of aging, 33(1), 198-e1.

38. Keng, F. Y. J. (2004). Clinical applications of positron emission tomography in cardiology: a review. Annals-Academy of Medicine Singapore, 33(2), 175-182.

39. Kim J. K., Kim D. U., Lee B. H., and Oh K. (2007). Arrayed Multimode Fiber to VCSEL Coupling for Short Reach Communications Using Hybrid Polymer-Fiber Lens. *IEEE Photonics Technology Letters*, *19*(13).

40. Kishimoto, A., Kataoka, J., Kato, T., Miura, T., Nakamori, T., Kamada, K., Nakamura, S., Sato, K., Ishikawa, Y., Yamamura, K., Kawabata, N., Yamamoto, S. (2013) Development of a Dual-Sided Readout DOI-PET Module Using Large-Area Monolithic MPPC-Arrays. *IEEE Transactions on Nuclear Science*, 60(1), 38-43

41. Knoll, G. F. (2000). *Radiation detection and measurement* (3rd ed.). New York: Wiley.

42. Kolb, A., Wehrl, H. F., Hofmann, M., Judenhofer, M. S., Eriksson, L., Ladebeck, R., Lichy, P. M., Byars, L., Michel, C., Schlemmer, HP., Schmand, M., Claussen, C. D., Sossi, V., and Pichler, B. J. (2012). Technical performance evaluation of a human brain PET/MRI system. *European radiology*, 1-13.

43. Lau, F. W., Vandenbroucke, A., Reynolds, P. D., Olcott, P. D., Horowitz, M. A., & Levin, C. S. (2010). Analog signal multiplexing for PSAPD-based PET detectors: simulation and experimental validation. *Phys. Med. Biol.*, *55*(23), 7149-7174.

44. Levin, C.S. (2002) Design of a high-resolution and high-sensitivity scintillation crystal array for PET with nearly complete light collection. *IEEE Transactions on Nuclear Science,* 49(5) 2236-2243

45. Lide, D. R. (2000). "Magnetic susceptibility of the elements and inorganic compounds". *CRC Handbook of Chemistry and Physics* (81st ed.). CRC Press.

46. Lima, J J Pedroso de, (2011). *Nuclear Medicine Physics. Series in Medical Physics and Biomedical Engineering.* CRC Press, Boca Raton, FL

47. Mackewn J. E., Strul D., Hallett W. A., Halsted P., Page R. A., Keevil S. F., Williams S. C. R., Cherry S. R., and Marsden P. K. (2005). Design and Development of an MR-Compatible PET Scanner for Imaging Small Animals. *IEEE Transactions on Nuclear Science, 52*(5), 1376-1380.

48. Mancini, R. (2003). *Op Amps for Everyone.* Newnes.

49. McCallum, S. J., Clowes, P., and Welch, A. E. (2002). Simulation of the output from a scintillator/photodiode detector using Monte Carlo techniques and spice circuit simulation. In *Nuclear Science Symposium Conference Record (NSS/MIC), 2002 IEEE (Vol. 2*, pp. 881-884).

50. McClish, M., Dokhale, P., Christian, J., Stapels, C., and Shah, K. S. (2007). Characterization and scintillation studies of a solid-state photomultiplier. *Nuclear Instruments and Methods in Physics Research Section A: Accelerators, Spectrometers, Detectors and Associated Equipment*, *572*(3), 1065-1070.

51. McRobbie, D. W., Moore, E. A., Graves, M. J., and Prince, M. R. (2002). *MRI from picture to proton*. Cambridge: Cambridge University Press.

52. Moses, W. W. (2007). Recent advances and future advances in time-of-flight PET. Nuclear Instruments and Methods in Physics Research Section A: Accelerators, Spectrometers, Detectors and Associated Equipment, 580(2), 919-924.

53. Newport. (2013). Fiber Optic Basics – Tutorial. *Fiber Optic Basics.* Accessed April 2013 from: http://www.newport.com/Tutorial-Fiber-Optic-Basics/978863/1033/content.aspx

54. Olcott, P. D., Habte, F., Zhang, J., and Levin, C. S. (2005a). Charge multiplexing readout for position sensitive avalanche photodiodes. In *Nuclear Science Symposium Conference Record (NSS/MIC), 2005 IEEE* (Vol. 5, pp. 2935-2937).

55. Olcott, P. D., Talcott, J. A., Levin, C. S., Habte, F., and Foudray, A. M. (2005b). Compact readout electronics for position sensitive photomultiplier tubes. *IEEE Transactions on Nuclear Science, 52*(1), 21-27.

56. Olcott, P. D., Peng, H., and Levin, C. S. (2009a). Novel electro-optical coupling technique for magnetic resonance-compatible positron emission tomography detectors. *Molecular imaging*, 8(2), 74-86.

57. Olcott, P. D., Peng, H., and Levin, C. S. (2009b) Solid state photomultiplier (SSPM)-based PET detector with capacitively multiplexed readout and electro-optical coupling for PET/MR. *Soc. Nucl. Med. Annu. Meet. Abstracts 50*(Supplement 2) 354.

58. Otte, N. (2006). The silicon photomultiplier—a new device for high energy physics, astroparticle physics, industrial and medical applications. *Proceedings of the International Symposium on Detector Development for Particle, Astroparticle and Synchotron Radiation Experiments (SNIC, 2006)* (pp. 1-9).

59. Peng, H., Olcott, P. D., Spanoudaki, V., and Levin, C. S. (2011). Investigation of a clinical PET detector module design that employs large-area avalanche photodetectors. *Phys. Med. Biol., 56*(12), 3603.

60. Pichler, B. J., Judenhofer, M. S., Catana, C., Walton, J. H., Kneilling, M., Nutt, R. E., Siegel, S. B., Claussen, C. D., and Cherry, S. R. (2006). Performance test of an LSO-APD detector in a 7-T MRI scanner for simultaneous PET/MRI. *J. Nucl. Med.*, 47(4), 639-647.

61. Pichler, B. J., Wehrl, H. F., Kolb, A., and Judenhofer, M. S. (2008, May). Positron emission tomography/magnetic resonance imaging: the next generation of multimodality imaging?. In *Seminars in nuclear medicine* 38(3) pp. 199-208. WB Saunders.

62. Radeka, V. (1974). Signal, noise and resolution in position-sensitive detectors. *IEEE Transactions on Nuclear Science, 21*(1), 51-64.

63. Radoslaw, M., Espana Palomares, S., Thoen, H., and Vandenberghe, S. (2012). Performance of digital silicon photomultipliers for time of flight PET scanners. In *2012 IEEE Nuclear Science symposium and Medical Imaging Conference record (NSS/MIC 2012); Workshop on Room-Temperature Semiconductor X-Ray and Gamma-Ray Detectors*.

64. Rafecas, M., Boning, G., Pichler, B. J., Lorenz, E., Schwaiger, M., and Ziegler, S. I. (2001). A Monte Carlo study of high-resolution PET with granulated dual-layer detectors. *IEEE Transactions on Nuclear Science*, *48*(4), 1490-1495.

65. Renker, D. (2006). Geiger-mode avalanche photodiodes, history, properties and problems. Nuclear Instruments and Methods in Physics Research Section A: Accelerators, Spectrometers, Detectors and Associated Equipment, 567(1), 48-56.

66. Rohren, E. M., Turkington, T. G., and Coleman, R. E. (2004). Clinical Applications of PET in Oncology. *Radiology*, *231*(2), 305-332.

67. Säckinger, E. (2005). *Broadband Circuits for Optical Fiber Communication.* Hoboken, New Jersey: Wiley-Interscience.

68. Saha, G. B. (2005). *Basics of PET Imaging: Physics, Chemistry, and Regulations*. New York, NY: Springer Science+Business Media, LLC.

69. Schaart, D. R., Seifert, S., Vinke, R., van Dam, H. T., Dendooven, P., Löhner, H., and Beekman, F. J. (2010). LaBr3: Ce and SiPMs for time-of-flight PET: achieving 100 ps coincidence resolving time. *Phys. Med. Biol.*, *55*(7), N179-189.

70. von Schulthess, G. K., and Schlemmer, H. P. W. (2009). A look ahead: PET/MR versus PET/CT. *European journal of nuclear medicine and molecular imaging*, *36*, 3-9.

71. Seifert, S., van Dam, H. T., Huizenga, J., Vinke, R., Dendooven, P., Lohner, H., and Schaart, D. R. (2009). Simulation of silicon photomultiplier signals. *IEEE Transactions on Nuclear Science, 56*(6), 3726-3733.

72. Seifert, S., van Dam, H. T., Huizenga, J., Vinke, R., Dendooven, P., Löhner, H., and Schaart, D. R. (2012). Monolithic LaBr3: Ce crystals on silicon photomultiplier arrays for time-of-flight positron emission tomography. *Phys. Med. Biol.*, *57*(8), 2219-2233

73. SensL. (2011). *ArraySL-4 Scalable Silicon Photomultiplier Array Datasheet (Rev 1.3).* SensL.

74. Serway, R. A., and Jewitt J. W. (2008). *Physics for Scientists & Engineers, with Modern Physics* (7th ed.). Belmont: Thompson Higher Education.

75. Shao, Y., Li, H., and Gao, K. (2007) Initial experimental studies of using solid-state photomultiplier for PET applications. *Nucl. Instrum. Methods Phys. Res.* A, 580, 944–950

76. Siegel, S., Silverman, R. W., Shao, Y., and Cherry, S. R. (1996). Simple charge division readouts for imaging scintillator arrays using a multi-channel PMT. *IEEE Transactions on Nuclear Science, 43*(3), 1634-1641.

77. Song, T. Y., Wu, H., Komarov, S., Siegel, S. B., and Tai, Y. C. (2010). A sub-millimeter resolution PET detector module using a multi-pixel photon counter array. *Phys. Med. Biol.*, *55*(9), 2573.

78. Spanoudaki, V. C., Mann, A. B., Otte, A. N., Konorov, I., Torres-Espallardo, I., Paul, S. and Ziegler, S. I. (2007) Use of single photon counting detector arrays in combined PET/MR: Characterization of LYSO-SiPM detector modules and comparison with a LSO-APD detector, *JINST.* **2** P12002

79. Spanoudaki, V. C., Lau, F. W. Y., Vandenbroucke, A., and Levin, C. S. (2010). Physical effects of mechanical design parameters on photon sensitivity and spatial resolution performance of a breast-dedicated PET system. *Medical physics*, *37*(11), 5838-5849.

80. Surti, S., Kuhn, A., Werner, M. E., Perkins, A. E., Kolthammer, J., and Karp, J. S. (2007). Performance of Philips Gemini TF PET/CT scanner with special consideration for its time-of-flight imaging capabilities. *J. Nucl. Med., 48*(3), 471-480.

81. Thompson, C. J., Goertzen, A. L., Berg, E. J., Retière, F., Kozlowski, P., Ryner, L., Stortz G., and Sossi, V. (2011). Evaluation of high density pixilated crystal blocks with SiPM readout as candidates for PET/MR detectors in a small animal PET insert. *Nuclear Science Symposium and Medical Imaging Conference (NSS/MIC), 2011 IEEE* (pp. 2430-2435).

82. Ulaby, F. T. (2006) *Fundamentals of Applied Electromagnetics*. Upper Saddle River: Prentice-Hall, Inc.

83. Valk, P. E., Bailey, D. L., Delbeke, D., Maisey, M. N., and Townsend, D. W (2006). *Positron Emission Tomography: Clinical Practice*. London: Springer-Verlag London Limited.

84. Vandenbroucke, A., Foudray, A. M. K., Olcott, P. D., and Levin, C. S. (2010). Performance characterization of a new high resolution PET scintillation detector. *Phys. Med. Biol.*, *55*(19), 5895-5911.

85. Vaquero, J. J., Sanchez, J. J., Lage, E., Udias, J. M., Guerra, P., and Desco, M. (2011, October). Design of DOI PET detector modules using phoswich and SiPMs: First results. *Nuclear Science Symposium and Medical Imaging Conference (NSS/MIC), 2011 IEEE* (pp. 3311-3313).

86. Wehrl, H. F., Judenhofer, M. S., Wiehr, S., and Pichler, B. J. (2009). Pre-clinical PET/MR: technological advances and new perspectives in biomedical research. *European journal of nuclear medicine and molecular imaging*, *36*, 56-68.

87. Wehrl, H. F., Judenhofer, M. S., Thielscher, A., Martirosian, P., Schick, F., and Pichler, B. J. (2011). Assessment of MR compatibility of a PET insert developed for simultaneous multiparametric PET/MR imaging on an animal system operating at 7 T. *Magnetic Resonance in Medicine*, *65*(1), 269-279.

88. Wernick, M. N., and Aarsvold, J. N. (2004). *Emission tomography: The fundamentals of PET and SPECT*. Boston: Elsevier Academic Press.

89. Westbrook, C. (2002) *MRI at a Glance.* Oxford: Blackwell Science

90. Wiener, R.I., Surti, S., Piemonte, C., Karp, J.S. (2011) Timing and energy characteristics of LaBr3[Ce] and CeBr3 scintillators read by FBK SiPMs. *Nuclear Science Symposium and Medical Imaging Conference (NSS/MIC), 2011 IEEE* , pp.4013,4019, 23-29 Oct.

91. Wu, Y., Ng, T. S., Yang, Y., Shah, K., Farrell, R., & Cherry, S. R. (2009). A study of the timing properties of position-sensitive avalanche photodiodes. *Phys. Med. Biol.*, *54*(17), 5155-5172.

92. Yamamoto, S., Kuroda, K., and Senda, M. (2003). Scintillator selection for MR-compatible gamma detectors. *IEEE Transactions on Nuclear Science*, 50(5), 1683-1685.

93. Yamamoto, S., Imaizumi, M., Watabe, T., Watabe, H., Kanai, Y., Shimosegawa, E., and Hatazawa, J. (2010). Development of a Si-PM-based high-resolution PET system for small animals. *Phys. Med. Biol.*, *55*(19), 5817-5831.

94. Yang, X., Downie, E., Farrell, T., and Peng, H. (2013). Study of light transport inside scintillation crystals for PET detectors. *Phys. Med. Biol.*, *58*(7), 2143-2161.

95. Yang, Y., Dokhale, P. A., Silverman, R. W., Shah, K. S., McClish, M. A., Farrell, R., Entine, G., and Cherry, S. R. (2006) Depth of interaction resolution measurements for a high resolution PET detector using position sensitive avalanche photodiodes. *Phys. Med. Biol. 51*, 2131–2142.

96. Yang, Y., James, S. S., Wu, Y., Du, H., Qi, J., Farrell, R., Dokhale, P. A., Shah, K. S., Vaigneur, K., and Cherry, S. R. (2011). Tapered LSO arrays for small animal PET. *Phys. Med. Biol.*, *56*(1), 139.

97. Yeom, J. Y., Spanoudaki, V., and Levin, C. S. (2011). Silicon photomultiplier-based detector array for TOF PET. In *Nuclear Science Symposium and Medical Imaging Conference (NSS/MIC). 2011 IEEE* (pp. 2415-2417).

98. Yoon, H. S., Ko, G. B., Kwon, S. I., Lee, C. M., Ito, M., Song, I. C., Lee, S. D., Hong, S. J., and Lee, J. S. (2012). Initial results of simultaneous PET/MRI experiments with an MRI-compatible silicon photomultiplier PET scanner. *J. Nucl. Med.*, *53*(4), 608-614.

99. Ziegler, S. I., and Delso, G. (2013). Technical and methodological aspects of PET/MR. *Clinical and Translational Imaging*, 1-6.

100. Zulliger, H. R., and Aitken, D. W. (1970). Fano factor fact and fallacy. *IEEE Transactions on Nuclear Science, 17*(3), 187-195.